Integrated Micro Gas Chromatographs with High-Flow Knudsen Pumps

by

Yutao Qin

A dissertation submitted in partial fulfillment
of the requirements for the degree of
Doctor of Philosophy
(Electrical Engineering)
in the University of Michigan
2015

Doctoral Committee:

Professor Yogesh B. Gianchandani, Chair
Professor Xudong Fan
Professor Katsuo Kurabayashi
Professor Khalil Najafi
Professor Kensall D. Wise
Associate Professor Zhaohui Zhong

To my wife and my parents

who have always loved me and supported me

Acknowledgements

I would like to acknowledge my research advisor, Prof. Gianchandani, for providing me an opportunity to become a PhD student, and delve into an exciting research project that still continues to fascinate me. His encouragement, advice, ideas, writing skills, working styles, *etc*. all helped me tremendously throughout my PhD study.

Next, I would thank my committee members, Prof. Fan, Prof. Kurabayashi, Prof. Najafi, Prof. Wise, and Prof. Zhong. They all provided valuable feedback to my work. The research in their groups, as well as those in Prof. Zellers' group, continue to inspire me substantially. It has been a great experience to be among such a big community of researchers working on related technologies.

I also thank all the people who have provided me generous assistance. Seungdo An has been a great mentor and collaborator, who worked with me on the Si-micromachined high-flow Knudsen pumps. Robert Gordenker has provided me a well-organized lab space with instruments set up for gas chromatography experiments, as well as many critical training, maintenance, and discussions. Naveen Gupta trained me on the Knudsen pumps. Christine Eun served as my initial LNF mentor. Jing Liu trained me on coating the gas chromatography columns. Xin Luo helped me set up experiments with microdischarge-based detectors. Prof. Kenichi Morimoto collaborated on modeling of the capacitive detectors. I also thank all my group members, fellow students and colleagues in other labs, and all the staffs, who helped me in one way or another.

Finally, I want to express my most sincere gratitude to my family. My wife, Yu (Fish) Huang, who has determined to abandon her study in China and accompany me in US, provided me with the greatest support that I could ever imagined, a home I can always return. All the joy and sorrow

that we shared are the most cherished part of my life. My parents have supported me wholeheartedly in every way they can. Without them, I would not have decided to pursue a PhD in the first place. Their excitement about every little progress I made always encourages me to carry on.

Table of Contents

List of Figures

List of Tables

List of Appendices

Abstract

Environmental gas sensing typically requires both sensitivity and specificity; target vapor species must not only be detected and quantified, but also differentiated from interferents. This mission can be accomplished by micro gas chromatographs (μGCs), which allow preconcentration of samples and subsequent separation of complex vapor mixtures into individual constituents by their specific retention times. This thesis focuses on the system-level design, fabrication, and integration of μGCs, with the ultimate goal of fully microfabricated systems that can be easily manufactured and distributed to end-users. This thesis also explores the optimization of a micro gas pump – a critical μGC component, and generally recognized as a challenge for microsystems.

Three generations of integrated μGC systems have been designed, fabricated, and evaluated. The *iGC1* system demonstrates the feasibility of a low-cost three-mask fabrication approach for a μGC including a Knudsen pump, a preconcentrator, a separation column and a microdischarge-based detector, which are integrated in a 4-cc stack. The *iGC2* system demonstrates a valveless μGC architecture, in which a bi-directional Knudsen pump provides reversible gas flow for (multi-stage) preconcentrators, which is essential for quantitative analysis. The *iGC3* system replaces the microdischarge-based detectors in *iGC1* and *iGC2* with complementary capacitive detectors, facilitating a purely electronic interface for the fluidics. Additionally, it is compatible with the use of room air as the carrier gas. The quantitative analysis of 19 chemicals with concentration levels

of well below 100 ppb is demonstrated, showing the promise of automated, continuous monitoring of indoor air pollutants.

The pumps used in the *iGCx* systems are Knudsen pumps that use thermal transpiration provided by nanoporous media and have no moving parts. This thesis also describes an exploratory effort in which lithographically fabricated channels in silicon substrates provide the thermal transpiration. The Si-micromachined Knudsen pumps demonstrate >200 sccm flow rate. To increase the output pressure head, these pumps are arrayed in series, using both a stacked configuration and a planar one. The results show that the pressure and flow characteristics can be tailored over a wide performance range, extending the possible applications beyond μGC systems.

Chapter 1:

Introduction

1.1. Various Technologies for Gas Phase Analyses

Gas phase analyses of volatile organic compounds (VOCs) typically involve a variety of gas species that are often present in unknown concentrations. Although a number of microscale gas sensors have been reported in the past [Bon08], the specificity provided by stand-alone sensors is inadequate for VOCs. The commonly used instruments that can provide the necessary differentiation and identification typically include three categories: the infrared (IR) spectroscope, mass spectrometer (MS) and gas chromatograph (GC). Each of these instruments has its own advantages; therefore they are often combined to provide accurate analyses on very complex gaseous samples.

The use of IR spectroscope for gaseous chemical analysis is based on the measurement of IR absorption by gas molecules. IR radiation permits the interrogation of the vibrational and rotational states of chemical bonds. Chemical bonds are thus identified and even quantified by examination and interpretation of the absorption bands in the IR spectrum. In early efforts IR spectroscopy was performed by transmitting radiation through gas samples; the results were analyzed by dispersive elements. Modern IR spectroscopy predominantly uses the Fourier-transform IR (FTIR) spectroscopy method, where two interfering IR beams pass through gas samples, and the resulting interferogram is processed by a computer using Fourier transformation, which reveals the absorption spectrum (Fig. 1.1a) [Stu04].

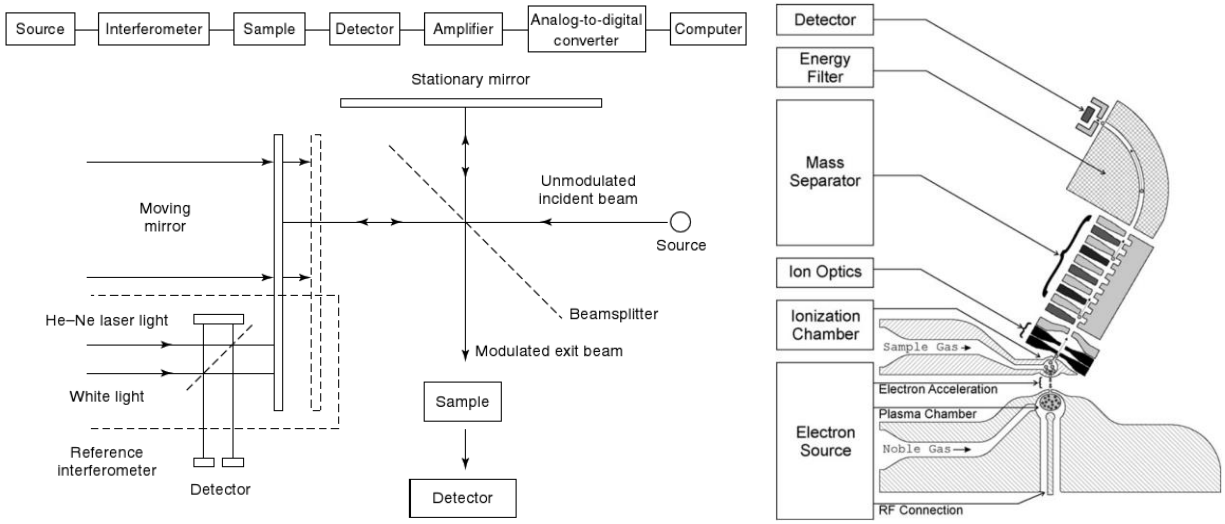

Fig. 1.1: (a) Schematic of typical Fourier-transform IR spectroscopy [Stu04]. (b) Schematic of a miniature mass spectrometer [Hau07].

The MS identifies gas molecules by the charge-to-mass ratio of ions. An MS is comprised of three major components: an ionization source that breaks down the analyte molecules into ions, a mass analyzer that separates the ions based on mass, and a detector that detects the ions. As the mass analyzer operates under vacuum, a vacuum pump is also required [We08].

The GC performs gas analyses by spatiotemporally separating gas mixtures. In a GC, the analyte mixture passes through a long channel (*i.e.*, the separation column) coated or loaded with a functional material (*i.e.*, stationary phase). The elution time can be used as an identifier of the gas species. A GC is typically comprised of a gas injector, a separation column, and the gas detector. For sampling low concentrations, a preconcentrator is often used as the gas injector. Additionally, the GC requires continuous carrier gas flow, which is generated by a pressurized gas cylinder or a gas pump.

The GC, MS, and IR spectroscope are often used in conjunction to perform analyses on very complex gaseous substances [Gos08]. For example, the GC is used to separate the complex vapor

into individual gas species, whereas an MS or FTIR positioned downstream of the GC is used as a detector to identify them. Such combinations provide very accurate analytical data.

The GC, MS, and IR spectroscope systems place different constraints on device miniaturization, which typically involves lithographic microfabrication. The miniature IR spectroscope requires microfabricated optical components. While various microfabricated components have been reported, fully microfabricated IR spectroscope systems remain rare. Miniaturized MS systems have been reported, *e.g.,* as shown in Fig. 1.1b [Hau07]. For miniaturized MS, a major challenge lies in the generation of vacuum (10^{-3}-10^{-6} Torr). For miniature GCs, most components are essentially microfluidic structures which are amenable to microfabrication. The gas pumps used in miniature GC are required to provide 1-10 kPa pressure head and ~1 sccm flow rate. Compared to the requirements of an MS, these are readily achievable by microfabricated gas pumps.

1.2. Conventional Gas Chromatography

Introduced in the early 1950s, the GC has grown into a complicated yet powerful system with numerous variations and combinations of its constituent components. The principles of the commercialized benchtop GC are discussed in this section while miniaturized GCs are reviewed in the next section. In both cases, a simplest GC system contains a gas injector, a separation column, a gas detector, and a gas flow generator in the form of either a pump or a pressurized gas tank (Fig. 1.2).

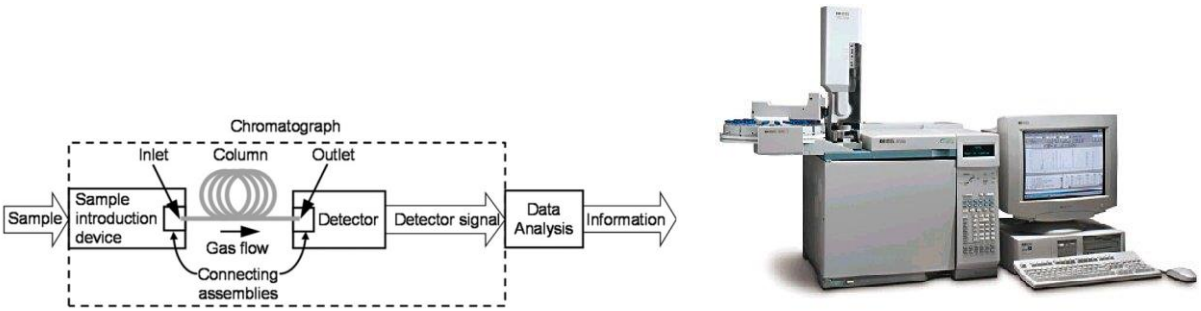

(a) (b)

Fig. 1.2: (a) Schematic of conventional GC [Blu12]. (b) A commercial benchtop GC model (Agilent 6890) [Sci15].

The separation column is structurally a long gas flow channel within which the vapor analytes can interact with a material – the stationary phase – that impedes the flow of various species by characteristic durations. Fused silica capillary tubes and stainless steel tubes are the most common types of column structures. Depending on how the stationary phase is incorporated, the separation column can be divided into two categories: packed column and capillary column (which is also called open tubular column). The former is packed with functionalized particles in the form of either inert solid particles coated with a layer of liquid stationary phase or uncoated solid adsorbent particles of the stationary phase material. In contrast, in a capillary column the inner walls is coated with a layer of stationary phase which can be either a liquid silicone or a solid porous material (PLOT column). Based on the physical form of the stationary phase, the chromatography is also classified into gas-liquid chromatography (GLC) and gas-solid chromatography (GSC), as different physics are used for gas separation. In GLC the separation is based on the partition of analyte molecules between the mobile phase (carrier gas) and the stationary phase, while in GSC the separation is based on the adsorption of analyte molecules onto the solid adsorbent surface [Bar04].

A variety of GC detectors have been developed, including the flame ionization detector (FID), the electron capture detector (ECD), and the thermal conductivity detector (TCD), and others. The

FID operates by ionizing the carbon-containing gas molecules in a flame of H_2 and air; the ions are collected by an electrode, providing a detectable electric current. The ECD operates by using a β radiation source to produce electrons that can be captured by gas analyte molecules; the reduction in the electric current caused by the β radiation indicates the presence of gas analytes. The TCD utilizes a filament to produce a thermal distribution profile in the carrier gas; the presence of gas analytes changes the overall thermal conductivity of the gas, resulting in a temperature change that can be detected by the filament resistance [Col04].

Most conventional GCs require a syringe to draw gas or liquid samples which are then transported into the GC injection module either manually or automatically. Commercialized GC injection modules typically employ a split technique in which the injected analytes are fully vaporized in a high temperature chamber. A valve controls the portion of gas injected into the separation column. Alternatively, a splitless technique may be used, in which all the injected analytes are transported into the separation column. On column injection techniques are sometimes used, in which the syringe needle is directly inserted into the column. The carrier gas flow in conventional GCs is provided by a pressurized gas cylinder with mass flow regulators [Sno04].

In addition to the basic GC components, a variety of peripheral components have been developed to enhance the GC power. Thermal desorption tubes are glass or steel tubes packed with adsorbent beds that can be used to sample gas analytes and perform thermal injection into the separation column. An oven and valves are often provided with the GC to allow temperature control of the separation column and gas flow paths. A special syringe needle packed with adsorbent is used to acquire concentrated analytes from dilute gas or liquid; this increasing popular method is called solid phase extraction (SPE).

Beyond the traditional one dimensional GC where only one column is used or several are connected in tandem, the comprehensive GC×GC technology is used to analyze very complex substances. In a GC×GC system, two columns are coated with different stationary phases that have distinctive separation mechanisms to achieve "orthogonal" separation, *i.e.*, several analytes co-eluting from one type of stationary phase can be separated by the other. In most cases the first column is a long column coated with a non-polar stationary phase while the second short and polar. A modulator injects analytes eluting the first column into the second column. A distinctive feature of GC×GC is the data processing, where the 1D raw chromatograms can be transformed into 2D or 3D for visualization and identification of families of chemicals with similar functional groups [Ada06].

1.3. Miniaturized GC Components and Systems

The need for portable and effective field analysis continues to drive the miniaturization of GC hardware. Research in μGC enabled by microfabrication technology, was launched over 30 years ago, with the early work dating back from 1979 when Terry *et al.* reported a micromachined GC system [Ter79]. Various micromachined column structures have been reported since then, such as the nickel column microfabricated by the Lithographie-Galvanoformung-Abformung (LIGA) process [Bhu07], the silicon-glass column microfabricated by the deep reactive ion etching (DRIE) and anodic bonding process [Aga05], the parylene column microfabricated by parylene deposition on sacrificial silicon/glass [Noh02], and the oxynitride column microfabricated by plasma-enhanced chemical vapor deposition (PECVD) of an oxynitride layer [Pot07]. The stationary phase coating methods for the microfabricated columns include the conventional static coating [Rei06] method as well as a recently reported self-assembly process [Zar10].

The preconcentrator-focuser (PCF), the miniaturized counterpart of the macroscale thermal desorption tube, is commonly used in μGC systems for gas sampling and injection. A three stage PCF has been reported [Tia05]; this was built with vertically standing microheaters and sorbent particles packed in between. An improved design of the PCF simplified the sorbent packing process [Ser13]. A passive PCF was also reported, which was designed to facilitate gas adsorption without utilizing active gas flow [Seo12]. As an alternative to the option of injecting a vapor pulse into the separation column by thermal desorption from an adsorbent, it is also possible to use an injection valve. For example, a pneumatically actuated six-port microfabricated valve was used as an injection device in a GC [Nac12].

A variety of micro gas detectors have been reported. The chemiresistor array uses gold nanoparticles protected with thiolate monolayers in a polymer matrix to form vapor-sensitive resistors [Ste11]. The chemicapacitor uses microfabricated capacitors formed by chemoselective polymer insulators between microfabricated electrodes [Mls06]. In the micro thermal conductivity detector, the suspended filament in its macroscale counterpart is replaced with a metal film heater on a glass substrate [Nar12]. The Fabry-Pérot detector uses a polymer coating either at the tip of an optical fiber or waveguide [Liu10] or on a silicon substrate [Red11] as a Fabry-Pérot interferometer; the eluting gas analytes cause swelling in the polymer layer, modulating the interference pattern that can be detected by a spectrometer. The discharge-based detector uses microfabricated electrodes to generate microplasma and detects chemicals by their emission spectra [Mit08, Luo11].

Other μGC components have also been reported. Two examples of micro gas pumps include the peristaltic pump that utilizes microfabricated membranes and valves to achieve stage-by-stage pumping [Kim07] and the Knudsen pump based on thermal transpiration in nanoporous material

[Gup11]. A thermal modulator has been reported, which utilizes a thermoelectric cooler to provide thermal modulation for a μGC×GC system [Ser12]. A micro valve for μGC applications has also been reported [Pot12].

The academic research in μGC systems that incorporate microfabricated GC components has also made remarkable progress (Fig. 1.3). Terry *et al.*'s pioneering work in 1979 included a microfabricated valve injector, separation column, and μTCD [Ter79]. The μChemLab reported by Lewis *et al.* was a hand-held μGC system that consisted of a preconcentrator, a column, and surface acoustic wave sensors [Lew06]. The University of Michigan had reported several prototypes of μGC over the past decade, including the Intrepid system for explosive marker detection [Zel11], the Spiron system for breath biomarker analysis [Kim11], and the palm-size Mercury system for use on autonomous robotic vehicles [Gor12]; these μGC systems incorporated micro-scale preconcentrators, columns, and chemiresistors. The components were assembled on printed circuit boards (PCB) with capillary tube connections and driven by commercial mechanical pumps. Two micro pump driven μGC systems were also reported, including one driven by a peristaltic pump [Kim07] and another driven by the Knudsen pump [Liu11].

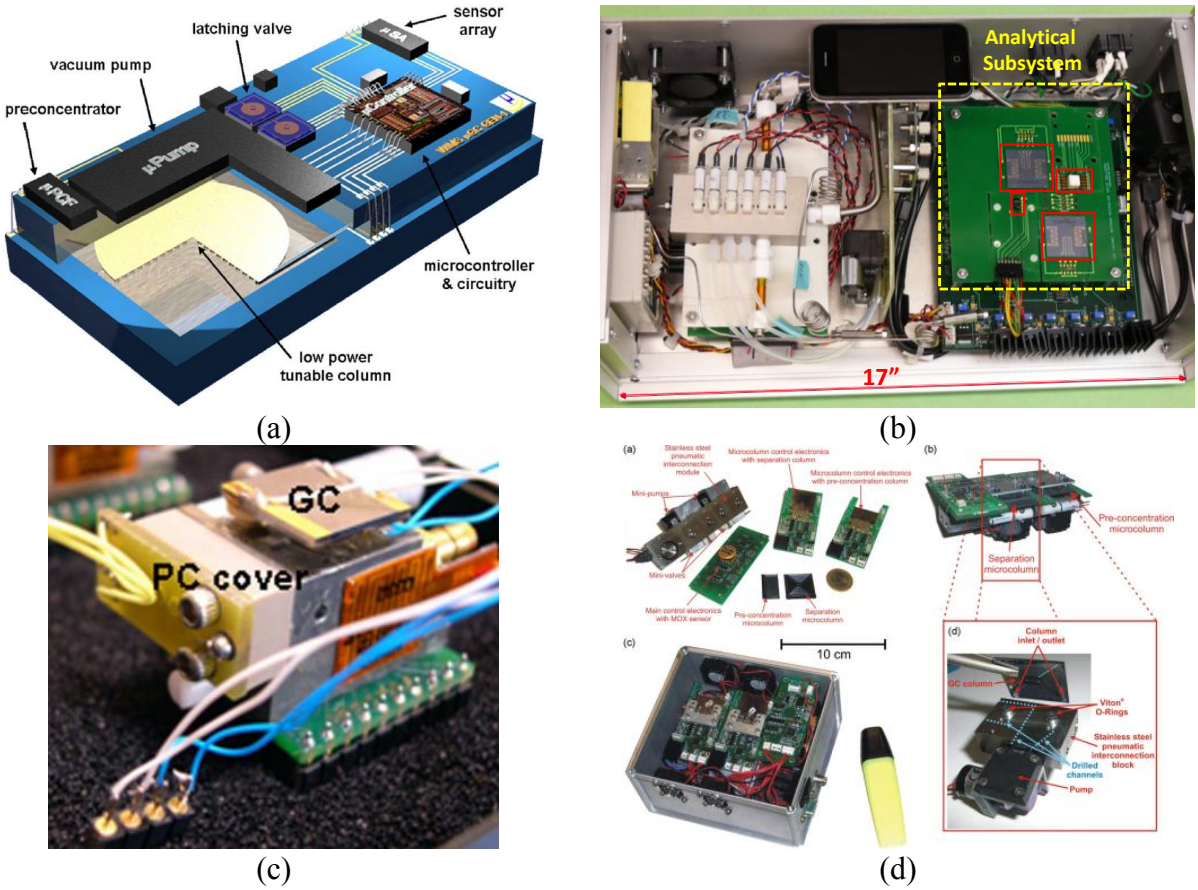

Fig. 1.3: Various μGC prototypes. (a) A vision of a fully integrated μGC [Pot07]. (b) The Spiron [Kim11]. (c) The μChemlab [Lew06]. (d) The miniGC [Zam09].

Over the years, a number of μGC systems that have appeared in the market made partial use of μGC components. The Inficon 3000 (Inficon Holding AG, Switzerland) and the C2V-200 (Thermal Scientific, Inc., TX) contain microfabricated sample injectors and TCDs. The Vernier mini-GC (Seacoast Science, Inc., CA) incorportates micromachined chemicapacitive sensors. The Varian CP 4900/Agilent 490 μGC (Agilent Technologies, Inc., CA) has a micromachined valve injector, a micromachined TCD and a micro-scale differential ion mobility detector. The SLS GCM5000 μGC (Elster Group GmbH, Germany) has a micromachined separation column and TCD. The zNose portable GC series (Electronic Sensor Technology, Inc., CA) includes microfabricated surface acoustic wave sensors.

1.4. Miniature Gas Pumps

Gas pumps in μGC systems are typically required to generate a pressure head of 1-10 kPa and a flow rate of ~1 sccm. The systems that use mass spectroscopy operate at a vacuum level of 10^{-4} -1 kPa (10^{-3}-10 Torr), while also providing ~1 sccm flow rate.

Many microfabricated gas pumps reported to date are based on diaphragm actuation (Fig. 1.4a-c). The first gas micropump that was reported operated on piezoelectric actuation of a brass diaphragm with diffuser nozzles rectifying the flow [Ste93]. It was capable of providing 35 sccm air flow and a blocking pressure of 2.3 kPa. Another piezoelectrically actuated gas pump used a polycarbonate diaphragm, and used check valves to rectify flow; this generated an air flow of 3.5 sccm and a blocking pressure of 50 kPa [Kam98]. A meso-scale dual diaphragm pump, based on electrostatic actuation of two perforated metallized Kapton diaphragms, was reported to generate an air flow of 30 sccm and a blocking pressure of 0.2 kPa [Cab01]. An 18-stage peristaltic pump, based on electrostatic actuation of parylene diaphragms that was used in pumping chambers as well as active microvalves, generated 4 sccm flow and a blocking pressure of 18 kPa [Kim07]. A number of miniature gas pumps based on diaphragm actuation have been commercially available, such as the KNF NMP series (KNF Neuberger, Inc., NJ), the Xavitech V200-GAS (Xavitech AB., Sweden), and the Bartels mP6 (Bartels Mikrotechnik GmbH, Germany).

Electrostatic actuation of diaphragm is power efficient, but the stress and fatigue in the diaphragm actuation may lead to diaphragm fracture [Yee13] and thus reliability and lifetime issues. In contrast, another type of gas micropump, the Knudsen pump, operates by the phenomenon of thermal transpiration; with no moving parts, long lifetimes have been demonstrated, e.g., ≈11750 hrs of continuous operation [Gup11].

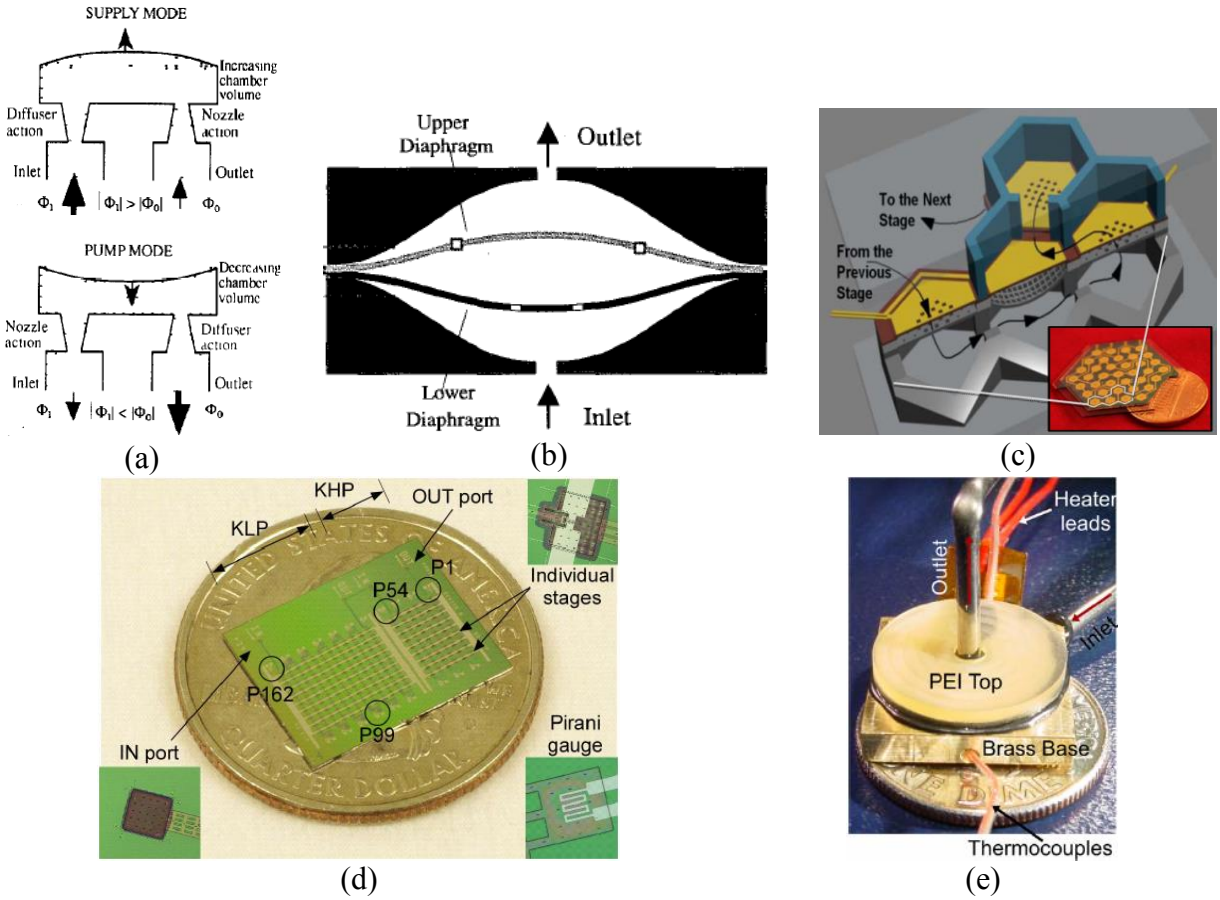

Fig. 1.4: Various micro gas pump prototypes. (a) Concept of a piezoelectric micropump with diffuser/nozzle [Ste93]. (b) Concept of an electrostatic dual-diaphragm pump [Cab01]. (c) A peristaltic roughing pump [Bes12]. (d) A 162-stage Knudsen pump [An14]. (e) A nanoporous membrane-based Knudsen pump [Gup11].

When two chambers are connected by a channel that has a hydraulic diameter that is comparable to or smaller than the mean free path of the gas molecules at the relevant pressure (i.e., $Kn \geqslant 0.1$), the gas flow is in the transition or free molecular regimes. Under these conditions, gas molecules flow from the cold end to the hot end of a narrow channel [Knu50, Rey79].

In order to facilitate the thermal transpiration for Knudsen pumps, both microfabricated channels and porous media have been employed (Fig. 1.4d-e). Thermal transpiration channels lithographically microfabricated on silicon substrates were reported in [An14, Gup12, McN05]. These efforts were directed at pumps intended to evacuate blind cavities. The 162-stage Knudsen

pump achieved a vacuum pressure of 0.9 Torr at atmospheric ambient pressure, but its flow rate was limited (~10^{-6} sccm) due to the small number of channels [An14]. The porous media employed in Knudsen pumps incorporated numerous nano/micro channels that permitted thermal transpiration to occur in parallel, thereby generating high gas flow. Various porous media, such as silicon aerogel [You03], glass microspheres [You03], naturally occurring zeolite [Gup11], and mixed cellulose ester (MCE) membranes [Gup11, Pha10], have been used. The MCE-based Knudsen pump generated air flow rates of ~1 sccm, sufficient for certain μGC systems [Liu11]. Using porous media is a low-cost and facile approach, but the channels cannot be tailored for varying pressure levels, and material defects can also limit the flow rate. In addition, assembly of porous media into lithographically fabricated frames can pose challenges to process integration [Gup11, Gup11].

1.5. Motivation for This Work

Monitoring of indoor air pollutants has become an important subject in environmental sensing. A major category of indoor air pollutant includes the VOCs. Common indoor VOCs include aromatic hydrocarbons, such as benzene, toluene, and xylenes (BTX), as well as alkanes, halogenated compounds, alcohols, aldehydes, ketones, terpenes, *etc*. These VOCs typically appear in higher concentrations indoors than outdoors [Bro94, Kos95]. The exposure limits of these VOCs are typically in the range of 1-100 ppm [Occ15]. Certain species can cause severe health hazards – for example, benzene is a known carcinogen [Huf07]. For pervasive deployment in households, offices, and public facilities, device miniaturization is the pathway to cost effectiveness. A device deployed for long-term indoor VOC monitoring should ideally be capable of performing automated sampling and analyses without requiring consumables or parts

replacement. Power consumption might not be a critical concern, as power sockets are often available in indoor environments. These features can ultimately be provided by μGCs.

Many μGC systems reported hitherto have focused on partial system miniaturization, and relied on external macro components. Additionally, these systems were comprised of components microfabricated by disparate processes [Gar15, Kim07, Kim11, Lew06, Zam09]. These aspects constrained the integration of entire μGC systems, and the potential reduction in system cost were not realized. This work investigates μGC systems with the following features: (1) all the components can be microfabricated using the same low-cost process; (2) room air can be used as the carrier gas, eliminating the use of external carrier gas supplies; (3) the system can ultimately perform continuous, automated monitoring of the environmental, typically air pollutants.

The state-of-the-art high-flow Knudsen pumps reported previously used nanoporous media to provide thermal transpiration. While the nanoporous MCE-based Knudsen pumps have demonstrated sufficient performance for some μGC [Liu11], their performance was still much lower than desired and an array of pumps was necessary. Therefore, this work also explores an approach to lithographically microfabricate dense arrays of narrow channels for thermal transpiration, eliminating any potential defect-induced leakage. In the long term, these Knudsen pumps can be used to support μGC systems with higher flow rate requirements that are more typical of conventional architecture.

Overall, the major contribution of this thesis is the system-level design, fabrication, and integration of full μGC systems. This task involves the integration of gas phase sensors and actuators, all microfabricated using a unified, low-cost process that enhances the manufacturability of the entire system. As the components are not each individually optimized by specific but distinct fabrication processes, the performance trade-off among the components is compensated

by system-level design. Beyond this goal, this thesis also contributes to the improvement of a critical μGC component, *i.e.*, the gas pump, which can ultimately not only be integrated into μGC systems but also used in other potential applications.

1.6. Organization of This Thesis

Chapter 2 describes an integrated μGC system, the *iGC1*, which contains four components: a nanoporous membrane-based Knudsen pump, a preconcentrator, a separation column, and a microdischarge-based gas detector that uses optical emission spectroscopy. All four components are fabricated from glass wafers using a three-mask process with minimal postprocessing. In a stackable architecture, the components are finally assembled into a 4-cm^3 system. The stacked *iGC1* system separates and detects of an alkane mixture in the range of C_5-C_8 in less than 60 s using N_2 as the carrier gas.

Chapter 3 describes a second μGC system, the *iGC2*. Compared to *iGC1*, the *iGC2* uses bi-directional Knudsen pump and a two-stage preconcentrator, components which are necessary for quantitative analysis in the absence of microvalves. Compared to the conventional approach of using valve routing to provide bi-directional flow, this μGC architecture reduces the overall complexity. The microsystem operation is experimentally validated by quantitative analyses of benzene, toluene, and xylene vapors ranging in concentration from 43-1167 mg/m^3 using N_2 as the carrier gas.

Chapter 4 describes a third μGC system, the *iGC3*, which replaces the microdischarge-based detectors in the previous two systems with capacitive detectors. This approach achieves a system in which all the components can be interfaced purely by electronic circuitry. Additionally, the system can use room air as the carrier gas, without relying upon external carrier gas supplies. The

system is used to demonstrate the analysis of 19 chemicals, most of which are common indoor VOCs at relevant concentrations. The experimental results show promise of a system for performing automated continuous monitoring of indoor air pollutants.

Chapter 5 describes single-stage Si-micromachined Knudsen pumps for high flow generation. It is comprised of arrays of densely integrated, vertically oriented parallel narrow channels, with a monolithically integrated heater and heat sink. The narrow channel sidewalls are made of a thin dielectric layer to provide thermal isolation between the heater and heat sink. The device is fabricated on a single wafer using a four-mask lithographic process. It demonstrates an air flow rate of >200 sccm when operated at atmospheric pressure, the highest reported to date for this type of pump.

Chapter 6 describes two architectures for configuring multi-stage Si-micromachined high-flow Knudsen pumps. In the primary architecture, the single-stage Si-micromachined high-flow Knudsen pumps are stacked with Si-micromachined spacers to form multi-stage pumps. Another architecture that arranges the single-stage pumps in a planar array is used to benchmark the stacked architecture. Both architectures show that the pressure head of the single-stage pumps can be multiplied by the number of stages, while the flow rate can be maintained.

Chapter 7 concludes this thesis and provides a brief discussion about the future work.

Chapter 2:

iGC1: an Integrated Fluidic System for Gas Chromatography Including Knudsen Pump, Preconcentrator, Column, and Detector, Microfabricated by a Three-Mask Process

This chapter describes an integrated μGC system, the *iGC1*, which contains four components: a Knudsen pump, a preconcentrator, a separation column and a gas detector. All the four components are fabricated from glass wafers using a three-mask process with minimal post-processing. In a stackable architecture, the components are finally assembled into a 4-cm^3 system. The stacked *iGC1* system demonstrates the successful separation and detection of an alkane mixture in the range of C_5-C_8 in less than 60 sec.

2.1. Introduction

Most μGC research efforts have not incorporated the use of micropumps. Only two cases have been reported: one with a microfabricated, electrostatically-actuated peristaltic pump [Kim07], and another with an array of motionless Knudsen pumps [Red11]. The former required high frequency, large amplitude, drive voltages, but was power-efficient. The latter was not power-efficient, but required only a low-voltage DC source; it provided high reliability, with continuous operation for over 6000 hours [Gup11].

Many micropump-operated μGC systems reported to date have used components fabricated by disparate microfabrication processes. Some systems connect the components by tubing (*e.g.*,

[Gor12, Kim07, Kim11, Red11, Zel11]), whereas some use manifolds for fluidic interconnect (*e.g.*, [Adk10, Adk09, Man08, van08]). The benefit of this approach is that each component can be optimally designed and fabricated. Unfortunately, the increased complexity and cost of the fabrication of the whole system pose a challenge for integration. As in other fluidic systems, a stackable architecture (*e.g.*, [Lew07]) or a monolithic integration scheme (*e.g.*, [Man11]) can alleviate this problem. Additionally, using a simple and easily available microfabrication process for all of the components would greatly benefit the manufacturability and integration of the system.

This chapter reports the use of a simple three-mask fabrication process for simultaneously manufacturing a preconcentrator, a separation column, a discharge-based detector, and a Knudsen pump. Design innovations at the device level are used to accommodate this facile process, followed by system assembly. A stackable architecture is used for the system integration scheme, eliminating the use of tubing for gas flow interconnects and providing a path for further miniaturization.

As opposed to the pump array [Liu11] that included six KPs fabricated by drill machining, the *iGC1* system uses a single KP that is for the first time designed for integration within a μGC and micromachined lithographically. It also provides at least an order of magnitude improvement in footprint and power.

The design and modeling of the *iGC1* system are described in Section 2.2, the fabrication process is described in Section 2.3, experimental results are presented in Section 2.4, followed by the discussion and conclusions in Section 2.5.

2.2. Design and Modeling

Knudsen pump

Knudsen pumps are driven by thermal transpiration in narrow channels that constrain flow to the free-molecular or transition flow regimes. Gas molecules move against a temperature gradient, *i.e.*, from the cold end to the hot end of the channels; the pump itself has no moving parts. In this effort, the Knudsen pump (Fig. 2.1) consists of three glass dice (Die 1-3, thickness =500 μm) sandwiching a stack of nanoporous mixed cellulose ester (MCE) membranes (thickness ≈105 μm, pore diameter ≈25 nm, porosity ≈70%, Millipore, MA). The membranes are cut to 1.2 × 1.2 cm^2 squares, which form the active pumping areas. The pore diameter is on the same order of magnitude as the mean free path of air near atmospheric pressure. Multiple grooves on Die 1 and multiple through-holes on Die 2 facilitate the gas flow through the MCE membrane, while the grooves on Die 3 guide the gas flow into the upper components. The temperature gradient is applied by a thin-film heater on Die 2 and an external heat sink attached to the bottom of Die 1. In this work the heat sink is a simple aluminum plate with a perforation at the gas inlet. Its footprint is slightly larger than the Knudsen pump. Based on equations (5.3) and (5.4), the Knudsen pump described for this effort is estimated to provide a maximum air flow rate of 6.7 sccm and a blocking pressure of 6.7k Pa with ΔT_{KP} =60°C.

The preconcentrator adsorbs the analyte molecules onto a porous surface at room temperature. To initiate analysis, sample is desorbed with a thermal pulse and injected into the fluidic path. This work utilizes a single bed preconcentrator, designed as an 11 mm^3 chamber formed by Die 5 and Die 6 (Fig. 2.1). Granules of Carbograph™ 2 (Grace Davison Discovery Sciences, IL), a graphitized carbon with a surface area of 10 m^2/g, are packed in the chamber as the sorbent material. In addition to the gas inlet and outlet features, the preconcentrator contains a sorbent loading port from which the sorbent granules can be loaded. The arrays of pillars are designed to confine the sorbent granules in the chamber. In this work, the preconcentrator is designed to have the largest

achievable sorbent chamber without compromising the thermal isolation and form factor of the system (Fig. 2.1).

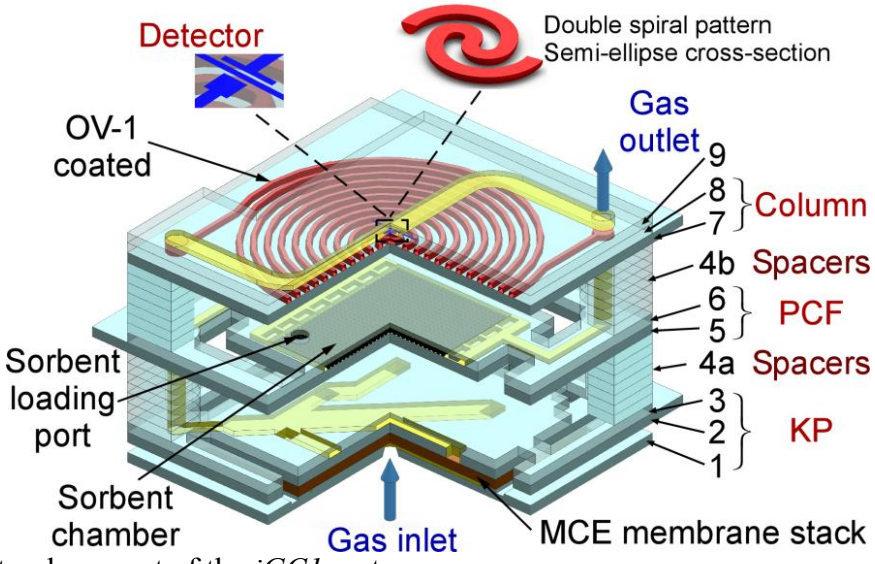

Fig. 2.1: Structural concept of the *iGC1* system.

Preconcentrator

The theoretical modeling of the sorbent-packed preconcentrators is often described using the Wheeler-Jonas model [Jon73]. The breakthrough time t_b (min.) is a metric for characterizing the adsorption capability. Specifically, it is the time required for vapor that enters the preconcentrator to saturate and reach a certain concentration at outlet (expressed as a fraction of that at inlet):

$$t_b = \frac{W_e}{Q \cdot c_{in}} \left[W - \frac{Q \cdot \rho_b}{k_v} \ln\left(\frac{c_{in}}{c_{out}} \right) \right] \tag{2.1}$$

where W_e is the adsorption capacity that can be theoretically derived [Jon73], W is the total sorbent mass (g), Q is the volumetric flow rate (cm^3/min.), c_{in} is the inlet chemical concentration (g/cm^3), ρ_b is the bulk density of the packed sorbent (g/cm^3), k_v is the overall mass transfer coefficient (min.$^{-1}$) that can be estimated from semi-empirical equations [Lod03], and c_{out} is the outlet chemical concentration chosen to denote breakthrough (g/cm^3).

The adsorption capacity W_e can be theoretically predicted using the modified Dubinin equation [Jon73]:

$$W_e = W_0 \rho_L \exp\left[-\frac{k_0 R_g^2 T_{bed}^2}{\beta_a^2} \ln^2 (\frac{P_S}{P_V}) \right] \tag{2.2}$$

where W_0 is the micropore volume (cm^3/g), ρ_L is the adsorbate liquid density (g/cm^3), k_0 is the structural constant of the sorbent (cal^{-2}/mol^{-2}), R_g is the universal gas constant, T_{bed} is the temperature of the packed bed (K), β_a is the affinity coefficient of the adsorbate, P_S is the saturated adsorbate vapor pressure at temperature T_{bed}, P_V is the adsorbate vapor pressure at temperature T_{bed}.

The overall mass transfer coefficient k_v can be calculated using the semi-empirical equation [Lod03]:

$$k_v = 800 \cdot \beta^{0.33} \cdot v_L \cdot {d_P}^{-1.5} \cdot \sqrt{\frac{W_e}{M_W}} \tag{2.3}$$

where v_L is the linear velocity of the vapor passing through the sorbent bed (cm/s), d_P is the average diameter of the carbon particle (cm), M_W is the molar mass of the adsorbate vapor (g/mol).

The preconcentration factor is another parameter that characterizes the overall efficiency of the preconcentrator. Different definitions of the preconcentration factor coexist in literature. It is defined as the ratio of the sampling volume to the desorption volume of the preconcentrator [Tia03].

Separation column

The column separates analyte species as they pass along, based on the partition that each analyte establishes between the mobile phase (carrier gas) and the stationary phase. In this effort, the column is designed as a channel (length ≈25 cm) laid out in a double-spiral pattern and formed by the bonding of Die 7 and Die 8 (Fig. 2.1). The manufacturing process creates an approximately semi-elliptical cross-section (width ≈300 μm, depth ≈200 μm), which has a hydraulic diameter

≈230 μm (defined as 4×area/perimeter). A ≈0.2 μm thick non-polar polydimethylsiloxane (OV-1, Ohio Valley Specialty, OH) layer is coated on the inner walls as the stationary phase.

The separation efficiency of a chromatography column can be evaluated from experimentally obtained chromatograms. Higher separation efficiency is denoted by higher number of plates, N, as well as smaller dimension of a theoretical plate, termed the "height equivalent to a theoretical plate (HETP)". The HETP of the column can be calculated accordingly, which facilitates the evaluation and comparison of columns with various lengths.

$$N = 5.54\left(\frac{t_R}{W_{1/2}}\right)^2 \tag{2.4}$$

$$\text{HETP} = \frac{l_{column}}{N} \tag{2.5}$$

where t_R is the retention time, $W_{1/2}$ is the width of the retention peak measured at half height, and l_{column} is the length of the separation column.

The retention factor, k, can also be measured from the chromatogram as follows:

$$k = \frac{t_R - t_0}{t_0} \tag{2.6}$$

where t_0 is the hold-up time the column, which can be measured by the elution time of an unretained chemical.

The retention factor k is also called the capacity ratio, which has a physical meaning – the ratio of the mass of substance in the stationary phase to that in the mobile phase, at partition equilibrium.

The HETP can also be theoretically estimated using the rate theory [Bar04], where the peak broadening is explained through a number of diffusion and mass transfer factors that result from the structural dimensions and physical properties of the column. The HETP of an open-tubular column can be theoretically calculated by the Golay – Van Deemter equation:

$$H = A + B/u + C_g u + C_l u + H_{ec} \tag{2.7}$$

where u is the average gas velocity, A is the band broadening term due to the eddy diffusion resulted from irregularities in the column structure, B is the longitudinal diffusion coefficient, C_g and C_l denote the resistance to mass transfer in the mobile phase and the stationary phase, respectively, H_{ec} accouts for an extra-column band broaden term resulting from the testing instruments.

By convention the A term in equation (2.7) describes the packing condition of a packed column and diminishes in characterizing an open-tubular column with thin film wall coating. However, surface roughness and defects exist in microfabricated open-tubular columns, causing minor eddy diffusions. Therefore the author deem it helpful to keep the A term in characterizing some microfabricated columns. For a short separation column with a circular cross-section and operating under a moderate pressure difference, the coefficients B, C_g, C_l and H_{ec} are provided by:

$$B = 2D_g \tag{2.8}$$

$$C_g = \frac{1 + 6k + 11k^2}{96(1+k)^2} \frac{d^2}{D_g} \tag{2.9}$$

$$C_l = \frac{2}{3} \frac{k}{(1+k)^2} \frac{h^2}{D_l} \tag{2.10}$$

$$H_{ec} = \frac{\Delta t^2}{l_{column}(1+k)^2} u^2 \tag{2.11}$$

where D_g and D_l are the coefficients of diffusion of the substance in the mobile phase and the stationary phase, respectively, d is the internal diameter of the separation column, h is the film thickness of the stationary phase, Δt is the total instrumental dead time. Usually for a

microfabricated column with a thin film stationary phase, the resistance to mass transfer in the mobile phase is dominant over that in the stationary phase ($C_g \gg C_l$).

Detector

The discharge-based gas detector uses two metal electrodes to create localized microdischarges, which generate optical spectra indicating the presence of carbon atoms. Although RF-powered microdischarges and DC microdischarges are options as summarized in [Eun12], pulsed DC microdischarges are used because they consume low power, require a simple interface circuit, and offer an extended lifetime [Eun12, Mit08]. As shown in Fig. 2.1, the electrodes for creating microdischarges, spaced 50 μm apart, are located on Die 8, while the groove structure of Die 9 guides the gas to pass over the detector. The optical signal is detected by a hand-held spectrometer (Model # USB 2000, Ocean Optics, FL), which is controlled by a laptop computer.

Stacked iGC1 Assembly

The four components are arranged in a stack, forming a serially connected gas flow path (Fig. 2.1). Driven by the Knudsen pump located upstream, the preconcentrator accumulates analytes and desorbs them along the same gas flow direction. The desorbed gas analytes pass through the column with characteristic retention times that are temporally resolved by the detector. Thermal crosstalk between the pump, preconcentrator, and separation column is inhibited by glass spacers (Dice 4a and Dice 4b) and the cut-outs (voids) in each layer. Depending on the system requirements, more spacers can be added to the system to achieve superior thermal isolation.

Thermal Modeling of the Stacked iGC1 Assembly

The thermal behavior of the stacked *iGC1* assembly was modeled using finite element analysis (FEA) in COMSOL Multiphysics 4.2. The simulations were directed at modeling the temperature distributions of the system while the Knudsen pump or the preconcentrator is heated. In both cases,

the simulated structure included 7 spacers both between the preconcentrator and the column as well as between the preconcentrator and the Knudsen pump, mimicking the actual system used for experimental tests. The thermal conductance of the MCE membrane stack in the Knudsen pump was derived from an experimentally fitted equivalent value. The bottom of the Knudsen pump was assumed to be maintained at room temperature by an ideal heat sink. The system was surrounded by an air box with natural convective heat transfer to the ambient.

In the case where the preconcentrator is heated, it is subject to a thermal pulse (12 W, 2 sec) and reaches 170°C (Fig. 2.2a and b). Because of the thermal isolation offered by the spacers and the pulsed nature of the heating, the column and the Knudsen pump are only minimally affected. In the case where the Knudsen pump is actuated, there is a 50°C temperature difference across the MCE membrane stack with 1 W input power (Fig. 2.2c and d). The simulation shows that the maximum parasitic temperature rises, after reaching steady state in ≈400 sec, are ≈18°C in the preconcentrator and ≈14°C in the separation column. This thermal crosstalk, which exists during both vapor sampling and analytical separation, is small enough that the preconcentrator and the column remain functional. The exact thermal crosstalk depends on how the system is operated. For vapor sampling and separation times shorter than 400 sec, the thermal crosstalk is smaller.

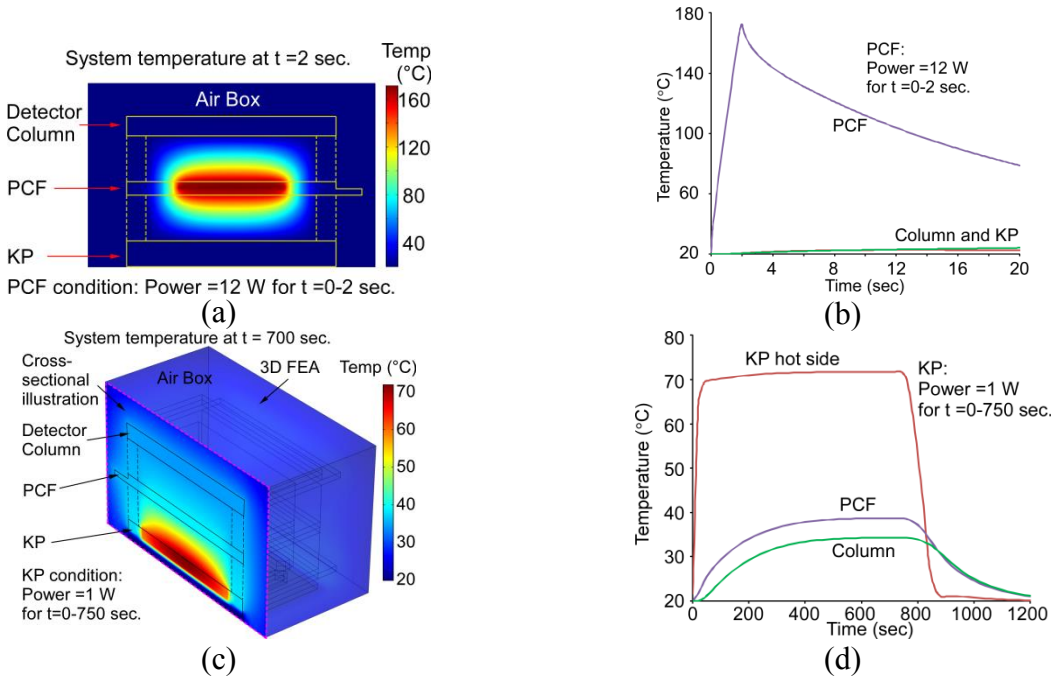

Fig. 2.2: The FEA simulation result of the thermal response of the *iGC1* system. (a) The temperature profile of the system after heating the preconcentrator with 12 W for 2 sec. (b) The transient thermal response of the system during a thermal cycle of the preconcentrator. (c) The temperature profile of the system after heating the Knudsen pump with 1 W for 700 sec. (d) The transient thermal response of the system during a thermal cycle of the Knudsen pump.

2.3. Fabrication

The fabrication process can be divided into two major steps. The first is the lithographic microfabrication: a common 3-mask sequence is used for all the four *iGC1* components. The second is the assembly of the system.

Lithographic Process

The lithographic microfabrication utilizes one mask for metallization and two masks for micromachining. Borosilicate glass is selected as the substrate material in this effort. However, any other kind of glass, including the low-cost sodalime glass can be used. To start with, a metal layer (Ti/Pt 25/100 nm) is deposited by thermal evaporation and patterned by liftoff on a 500 μm thick glass wafer (Fig. 2.3a), forming heaters, temperature sensors and microdischarge electrodes. The metallized wafer is subject to a two-step machining process that grooves the non-metallized

side of the wafer and creates through-wafer vias and cutouts (Fig. 2.3b). Each of the micromachining steps requires a mask. In this effort, a micro abrasive jet machining (sandblasting) was used (Bullen Ultrasonics, OH). The grooved structures form in-plane gas flow paths; the through-wafer vias form the inter-layer gas flow paths; and the through-wafer cutouts provide in-plane thermal isolation and stackable spacers. The sandblasted features typically have a 22° taper angle and a corner radius of 125 μm. The depth and feature sizes of the groove structures are in the range of 150-300 μm. In addition to sandblasting, many other approaches are available for micromachining glass wafers, such as plasma etching, wet etching and ultrasonic machining.

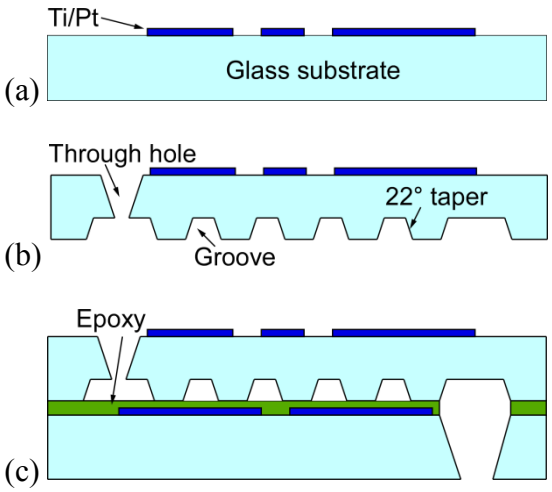

Fig. 2.3: Fabrication of the *iGC1* system. (a) Deposition and patterning of a Ti/Pt metal layer on a glass wafer. (b) Two-step sandblasting to create the groove structures and through-wafer vias and cutouts. (c) Epoxy bonding of two glass dice.

Assembly Process

If each component is fabricated on a separate wafer, system assembly can be performed at the wafer level. In this work, however, all the components are on the same wafer, so the dice are singulated prior to assembly. Each of the components is then epoxy bonded to its upper layer (Fig. 2.3c) before being added to the system stack (Fig. 2.4).

The Knudsen pump is assembled into a glass-MCE-glass stack. Die 2 and Die 3 are first bonded by a low-viscosity epoxy Epotek 377 (Epoxy Technology, MA), which is applied from the perimeter of the dice that are arranged in a stack, and drawn into the seams between the mating surfaces by capillary force. Curing at 150°C forms a leak free bond between the two glass dice. Next, Die 2, Die 3, four MCE membranes, and Die 1 are stacked (in order from top to bottom as stated). Finally, a viscous epoxy Stycast2850FT (Henkel, Düsseldorf, Germany) is applied around the edge of the MCE membrane stack to achieve a hermetic seal, which is crucial to the operation of the Knudsen pump.

The preconcentrator is assembled by epoxy bonding and sorbent packing. Die 5 and Die 6 are bonded by Epotek 377. Next, sorbent granules are packed into the preconcentrator using a similar method to that described in [Seo12]. Moderate vacuum from the inlet/outlet is used to draw the Carbograph 2 granules from the loading port into the preconcentrator. The pillar structures in the preconcentrator act as sieves to contain larger particles while letting smaller particles to pass through and exit the preconcentrator. After sorbent loading, the loading port is sealed with either thermal tape or epoxy.

The separation column is assembled by a coated layer of SU-8 5 (MicroChem, MA). Omnicoat (MicroChem, MA) is spin-coated and baked as the adhesion promoter, followed by a layer (less than 10 μm) of SU-8 spin-coated on the mating surfaces – specifically, the metallized side of Die 7 and the grooved side of Die 8. The grooved die (Die 8) is softbaked at 150°C in order to prevent the potential problem of fluid SU-8 filling and blocking the channel. Then the dice are aligned and stacked, followed by a second softbake at 95°C, which drives the fluid SU-8 to gradually fill the gaps and voids between the mating surfaces, providing a leak free bond. The device is exposed to ultraviolet (UV) radiation and hardbaked at 150°C to cure the SU-8 and minimize outgassing.

The spin-coating process described above fully covers the inner walls of the separation column with SU-8, providing two potential benefits for obtaining a more uniform coating of stationary phase. First, the inner surface of the column is a homogeneous material that provides uniform adhesion strength to the stationary phase. Second, any surface roughness on the grooves that may result from the sandblasting is smoothened by the SU-8 layer.

The SU-8 bonded column is then coated with a ≈0.2 μm thick layer of OV-1 stationary phase using a conventional static coating method [Rei06]. In this process, a solution of OV-1 is prepared by dissolving OV-1 and its cross-linking agent dicumyl peroxide in pentane and filled into the column. With one end of the column sealed, pentane is evaporated from the other end of the column by vacuum, leaving OV-1 coated on the inner walls of the column. After that, the column is heated at 150°C overnight to fully remove the solvent as well as to perform cross-linking. This coating process can be assisted by capillary tubes temporarily attached to both ends of the column using the epoxy Stycast2850FT; the capillary connections can be easily detached by localized heat after the coating process.

The detector is assembled by bonding Die 9 to Die 8 with Epotek 377 using the process as described for assembling the Knudsen pump.

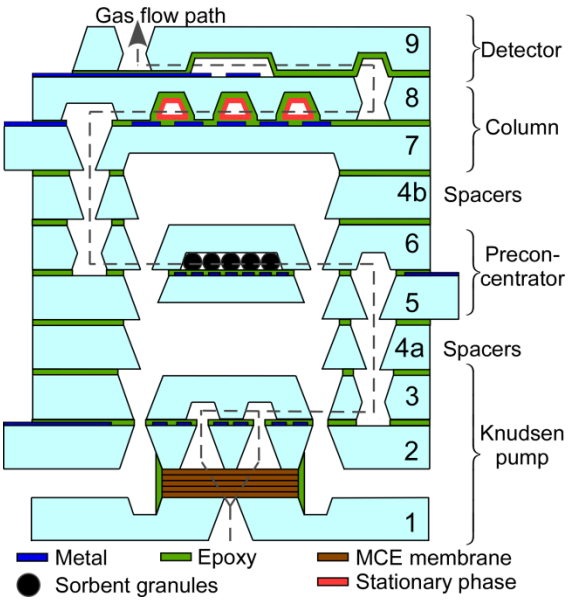

Fig. 2.4: The illustrated cross-section of the *iGC1* system after the final stacking.

The overall system is finally integrated by the assembly of all four components together with a number of spacers (Fig. 2.4), which are micromachined by sandblasting on the same glass wafer as the other dice. The spacers can be permanently bonded to the *iGC1* components using Epotek 377. However, a removable bonding layer between the components is also favored to allow reconfigurability. With low melting points and easy solubility in common solvents, various kinds of mounting wax have been widely used as temporary adhesives in the industry. The mounting wax QuickStick^{TM} 135 (Electron Microscopy Sciences, PA) is used in this effort to provide the removable bonding layers. When assembling the system, the components are placed on a hot plate at 150°C. The mounting wax is melted by the elevated temperature and applied to the mating surfaces. The components are then pressed together, allowing the mounting wax to form a leak free bond. The thermal operation of the *iGC1* system does not damage this bond as long as no strong shear force is applied. When it is necessary to reconfigure the *iGC1* system, the stack can be heated on a hot plate and the bond can be easily detached.

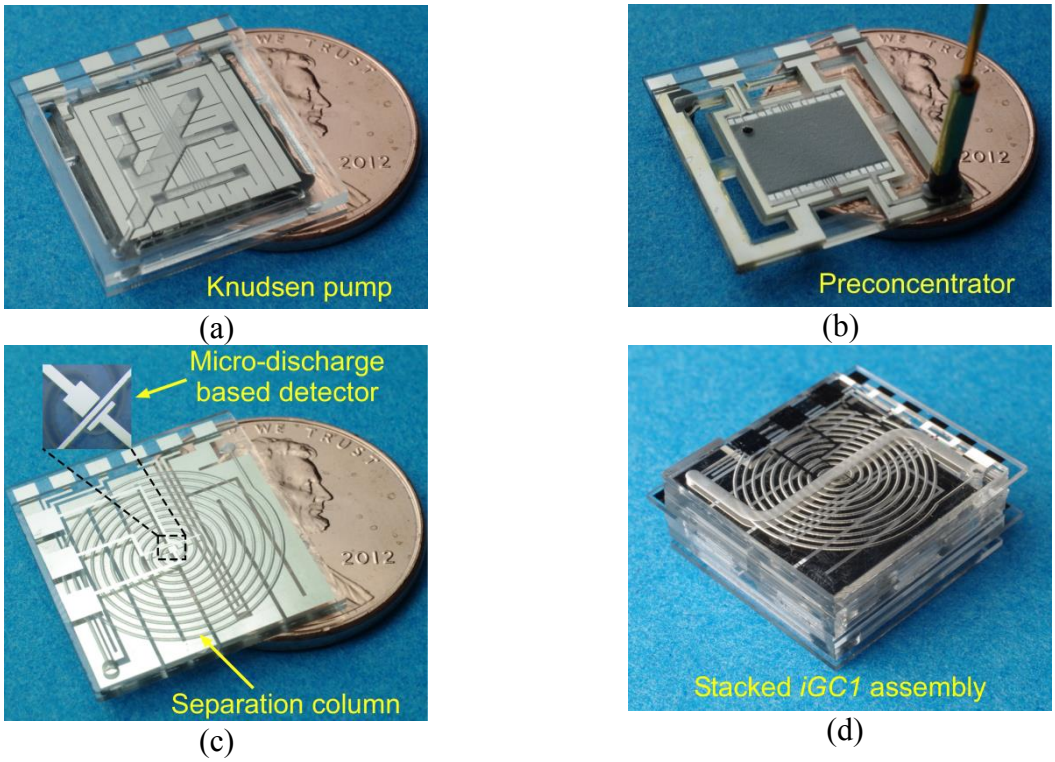

Fig. 2.5: Photographic images of (a) the Knudsen pump, (b) the preconcentrator, (c) the separation column and the discharge-based detector, and (d) the *iGC1* stack assembly.

The bottom surface of the *iGC1* stack can be attached to an aluminum plate, which serves as a heat sink for the Knudsen pump. Capillary tubes can be attached to the inlet and outlet of the *iGC1* system for testing.

Fabrication results of the various elements are shown in Fig. 2.5 The *iGC1* system has a footprint of 3.2 cm^2 and a height dependent on the number of spacers in the stack; a typical system tested in this effort has 14 spacers in total, corresponding to a total height of ≈1.15 cm and a form factor of 3.7 cm^3.

2.4. Experimental Results

Prior to the assembly of the full *iGC1* system, each component was separately evaluated. The experimental evaluations focused on alkanes in the range of C_5-C_8 for simplicity and

benchmarking purposes. These alkanes are also indicative of the system response to typical indoor pollutants. The results are presented below.

Pump and gas flow

In the evaluation of the Knudsen pump, its inlet was exposed to the ambient at atmospheric pressure, while varying loads (manifested as capillary tubes with varying length) were connected to its outlet. The values of the loads were selected to span over a wide range covering the actual load provided by the system. A commercial pressure sensor (Model # MPX5010DP, Freescale Semiconductor, AZ) and a flow meter (Part # FMA-1603A, Omega Engineering, CT) were connected between the outlet and the capillaries to monitor the pressure and flow conditions, respectively. With 1 W input power, the pump generated a ΔT_{KP} of ≈60°C, and was able to provide a steady state flow rate of 0.41 sccm against a pressure of 330 Pa; it provided a maximum pressure of 1 kPa. The flow rate declines linearly with load pressure (Fig. 2.6). The deviation of experimental data from the theoretical estimates is likely due to imperfections in the MCE membranes or in the loss of a portion of the temperature gradient in the air gap between the heater and the membrane [Gup11].

The load presented by the *iGC1* system was measured using a similar setup. The only differences were: an external pump replaced the Knudsen pump and the component stack (including preconcentrator, column, and detector) replaced the capillary tubes. With the data points linearly fitted into a load line, the flow conductance of the stacked preconcentrator, column and detector can be read from the slope – 0.64 sccm/kPa (Fig. 2.6). The system operating point is indicated by the intersection between the Knudsen pump curve and the system load line.

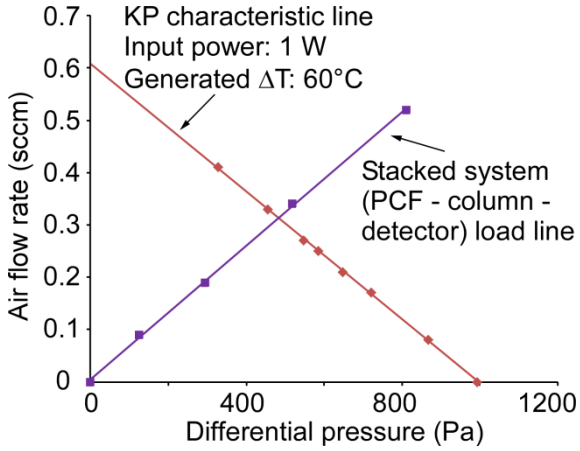

Fig. 2.6: The steady state performance of the Knudsen pump and the gas flow load of the system tested in room air.

Preconcentrator

The preconcentrator was characterized for both adsorption and desorption. The adsorption capability of the preconcentrator was experimentally evaluated by measuring the time taken by the vapor concentration at its outlet to reach a certain fraction of that at its inlet; this is known as "breakthrough". In this effort, the inlet of the preconcentrator was connected to a 2 L dilution bottle (Sigma Aldrich, WI) containing 80 ppm heptane in N_2; the vapor was drawn by a vacuum pump to pass through the preconcentrator at 1 sccm flow rate; the vapor concentration at the outlet was routed through a six-port valve to a flame ionization detector (FID) within a commercial Agilent 6890 GC. At two-minute intervals, the valve routed a fixed volume (100 µL) of the vapor downstream of the preconcentrator into the FID.

In Fig. 2.7a, the heptane concentration at the preconcentrator outlet is normalized to that at its inlet. The preconcentrator saturated after 45 minutes of sampling and the heptane concentration at its outlet approached the concentration at its inlet. Conventionally, the breakthrough criterion is defined to be the outlet concentration that is 10% of that at the inlet [Tia05]. For this work, this value corresponds to a breakthrough time of 16 minutes and a breakthrough volume of 16 mL for heptane.

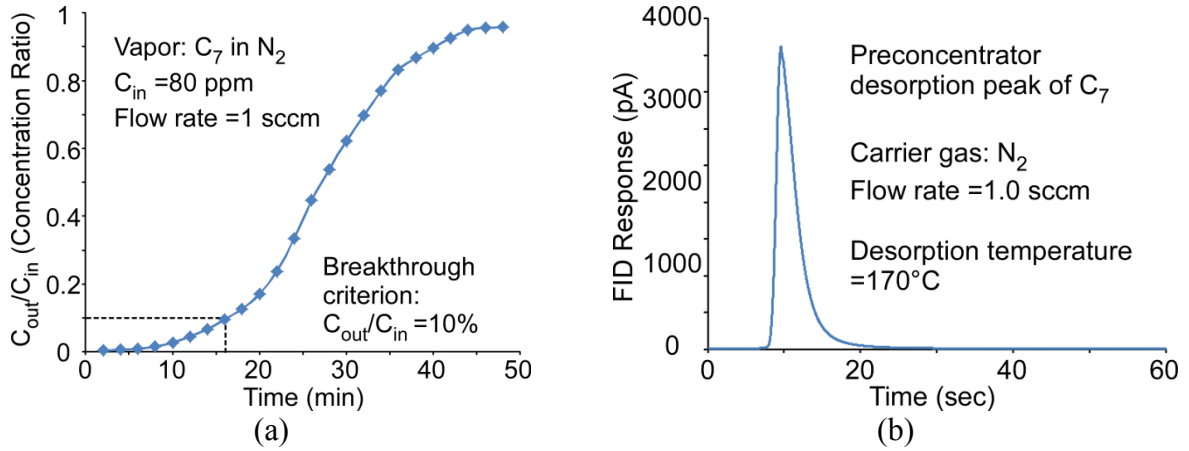

Fig. 2.7: The evaluation of the performance of the preconcentrator. (a) A sample breakthrough experiment by challenging the preconcentrator with heptane and measuring the vapor concentration at its outlet. (b) A heptane desorption peak provided by the preconcentrator with N_2 carrier gas.

The thermal desorption of the preconcentrator was evaluated by the desorption peak in the chromatogram. The preconcentrator was first used to sample the heptane vapor and then connected to the Agilent 6890 GC where it was positioned upstream of the FID and downstream of the injection port. The desorption was performed by applying a pulse using the integrated thin-film heater, which heated the preconcentrator to 170°C in 2 sec. The carrier gas was N_2 at a flow rate of 1 sccm; flow direction in the preconcentrator was the same during both sampling and desorption. As shown in Fig. 2.7b, a 1.4 sec. desorption peak (measured at half height of the peak) is observed from the FID chromatogram with only minimal tailing. A second thermal pulse did not provide any additional desorption peak, verifying full desorption during the first thermal pulse. This characterization of the preconcentrator is a representation of its general capability rather than its actual performance within the *iGC1* system. This is because the *iGC1* system is operated at a lower flow rate of ≈0.2 sccm. Not only is this more easily accommodated by the pump, but the performance of the separation column is better at this flow rate.

Column

The separation column was evaluated by an Agilent 6890 GC system by positioning it downstream of an injection port and upstream of an FID. Sample chromatograms obtained with the tested column are shown in Fig. 2.8. At room temperature, three alkane species (C_5, C_7, and C_8) were separated by the column in about 52 sec. (Fig. 2.8a). With a 30 sec.-long linear ramping of temperature from 25°C to 75°C provided by the on-chip heater, the column separated the same alkane mixture with the same gas flow rate in 30 sec. (Fig. 2.8b). Both chromatograms were obtained using N_2 as the carrier gas at 0.17 sccm flow rate.

Golay plots are curves indicating how the column efficiency is affected by the carrier gas flow rate, which are helpful in determining the optimal operating point of the column. In this effort, a Golay plot was obtained by testing the separation column at room temperature for a number of N_2 carrier gas flow rates. The C_8 peak was used for calculating the number of plates N and the height-equivalent-to-a-plate HETP based on Equations (2.4) and (2.5). As shown in Fig. 2.8c, the column has an optimal operating point at the gas velocity range of 5-10 cm/sec. (corresponding to the flow rate of 0.15-0.3 sccm), which gives HETP ≈0.04 cm and a plate number (1/HETP) of ≈2600 plates/m. This performance is comparable to other microfabricated columns that have been previously reported – 2000 plates/m [Lam05], 3000 plates/m [Zar10], and 4200 plates/m [Rei06].

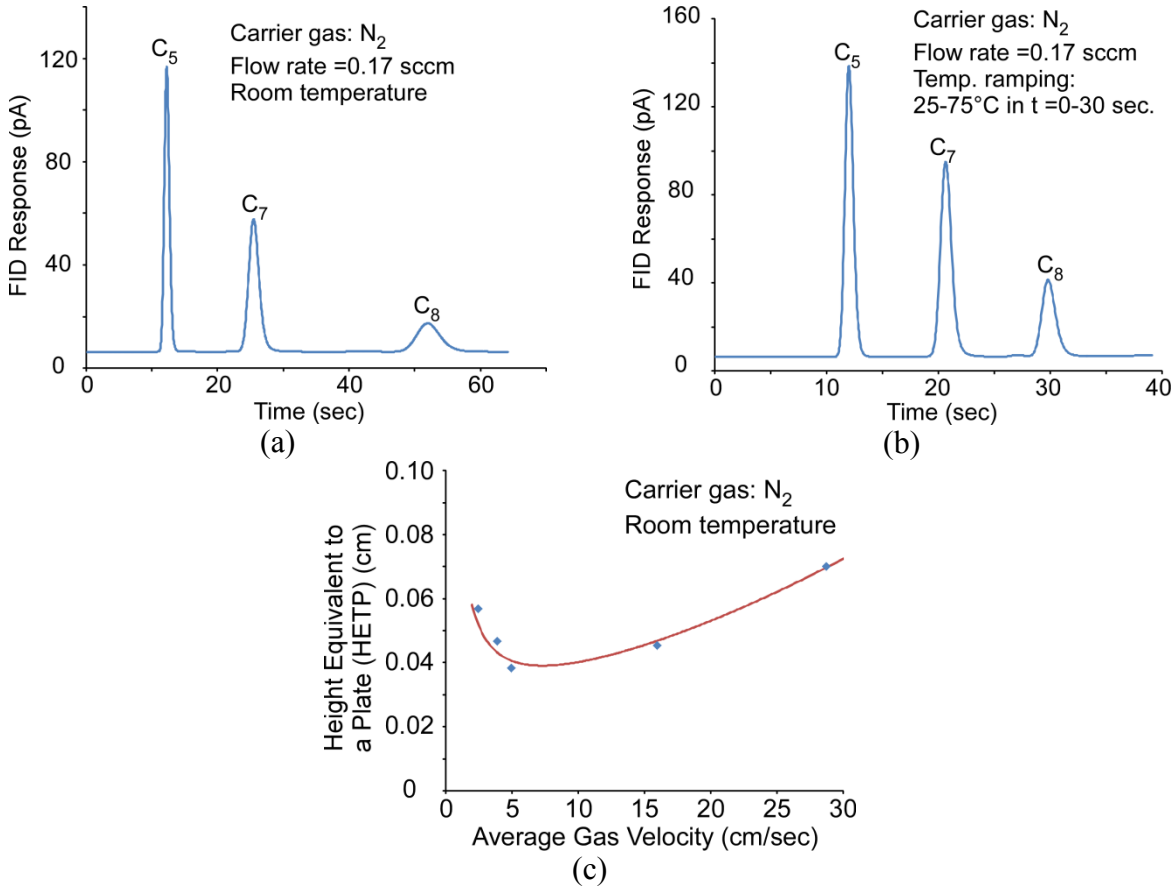

Fig. 2.8: The testing and evaluation results of the separation column. (a) The column separating a C_5, C_7, and C_8 alkane mixture at room temperature. (b) The column separating a C_5, C_7, and C_8 alkane mixture by linearly ramping the temperature from 25°C to 75°C in 30 sec. (c) The Golay plot of the separation column operating at room temperature; the evaluation is based on the C_8 peak.

Detector

The detector uses pulsed discharges that are controlled by the circuit shown in Fig. 2.9a. In this circuit, the discharge energy is provided by capacitor *C*, which is charged by a single 1000-V pulse through *R1*. Once the anode reaches the breakdown voltage, which is typically ≈650 V, the discharge is initiated. Resistors *R2* (the ballast resistor) and *R3* are used to control the discharge current. The resistive dividers formed by *R2/R3* and *R4/R5* are connected to oscilloscope channels, so that the anode and cathode voltages as well as the discharge current can be observed.

The typical transient voltages observed at the anode and cathode are shown in Fig. 2.9b. The anode took 1.6 ms to reach the breakdown voltage. The discharge current ran through the ballast resistor and raised the cathode voltage. Once initiated, the discharge presented in the circuit as 73 kΩ resistance. The high voltage pulse lasted 3.5 ms, during which the actual discharge took 1.9 ms. During the pulse, the typical energy consumed by the discharge was 2.9 mJ, while the total energy consumed by the whole circuit was 13.3 mJ.

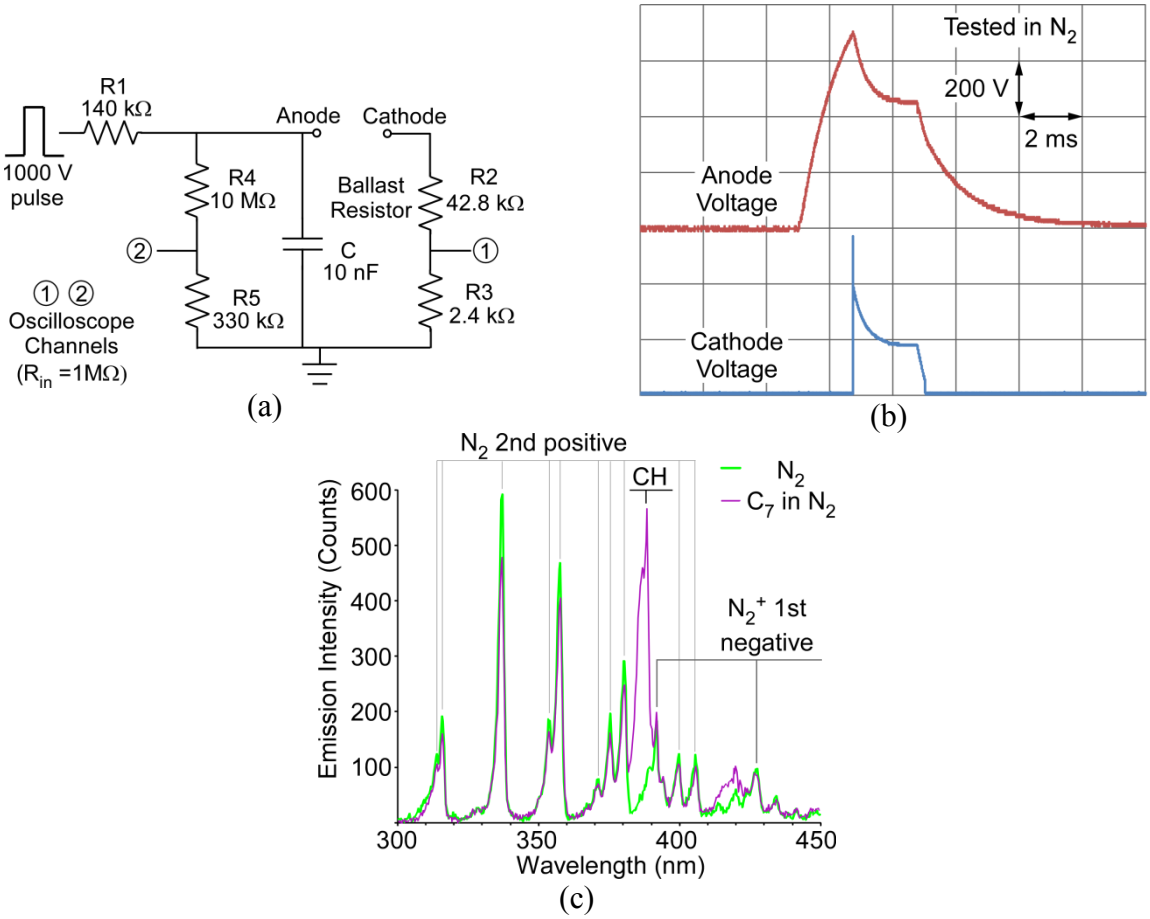

Fig. 2.9: The testing and evaluation results of the separation column. (a) The column separating a C_5, C_7, and C_8 alkane mixture at room temperature. (b) The column separating a C_5, C_7, and C_8 alkane mixture by linearly ramping the temperature from 25°C to 75°C in 30 sec. (c) The Golay plot of the separation column operating at room temperature; the evaluation is based on the C_8 peak.

Optical emission from the microdischarge is guided by an optical fiber to a handheld spectrometer (Model # USB 2000, Ocean Optics, FL). The spectrometer uses a grating to diffract

the incoming light. The resulting spatial distribution is captured by a charge-coupled device (CCD) array. The emission spectra, in the 300-450 nm window, of pure nitrogen and a heptane/nitrogen mixture are compared in Fig. 2.9c. The emission associated with the N_2 second positive system contains lines at 314 nm, 316 nm, 337 nm, 353 nm, 357 nm, 371 nm, 375 nm, 380 nm, 399 nm and 405, while that associated with N_2^+ first negative system contains lines at 391 nm and 426 nm [O'Ne68]. With an elevated concentration of heptane, the emission spectrum shows a significant CH line at 387 nm [Pea50]. The intensity ratio of the CH line at 387 nm to the N_2 line at 337 nm was used as a measure of alkane strength to correct for possible variations in intensity from pulse to pulse. The data points with sufficient emission intensity (*i.e.,* greater than 50 counts at 337 nm line) were used to construct chromatograms.

The stacked iGC1 system

Typical chromatograms provided by the stacked *iGC1* system for alkane mixtures are shown in Fig. 2.10. As shown from the data collected by the discharge-based detector (Fig. 2.10a), the three peaks correspond to the separation and detection of pentane, heptane and octane. The benchmark FID response (Fig. 2.10) verifies the results provides by the discharge-based detector. The FID signal lags behind that of the discharge-based detector as the FID is connected downstream of the *iGC1* stack. The relative peak heights among the three analytes are slightly different between the two chromatograms, possibly due to the emission characteristics of various species within the microdischarges. The power/energy consumption of the components and the *iGC1* system are summarized in Table 2.1. The *iGC1* run as shown in Fig. 10 had an average power consumption of 1.5 W.

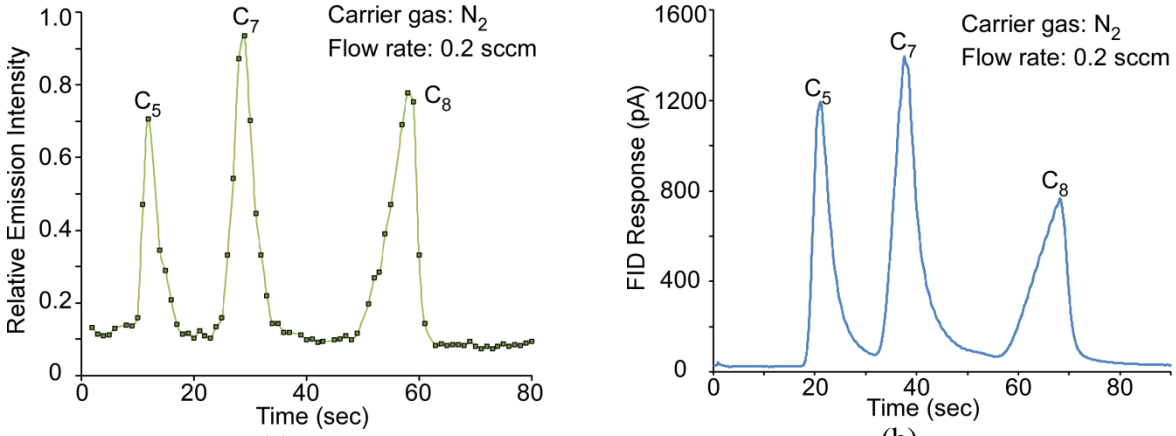

Fig. 2.10: The separation of pentane, heptane and octane by the fully stacked *iGC1* system. (a) The chromatogram provided by the discharge-based detector. (b) The corresponding chromatogram provided by the FID used as a reference.

Table 2.1: Power/Energy consumption during the *iGC1* separation.

Component	Operation	Energy/Power	Comment
Knudsen pump	Steady state pumping	1.1 W	Steady state power
Preconcentrator	2 sec. thermal pulse	34 J	Desorption energy
Column	Temperature programming	1.06 W	Average power during ramping
Discharge-based detector	3.5 ms high voltage pulse	13.3 mJ/pulse	Energy per pulse
Stacked *iGC1* system	Separation without column programming	1.5 W	Average power during a run

The results in Fig. 2.10(a) were obtained by first sampling a prepared vapor mixture. Driven by the integrated Knudsen pump, a mixture of pentane, heptane and octane in N_2 was sampled into the preconcentrator for ≈5 min. When initiating the separation, the preconcentrator was heated to 170 °C in 2 sec. to inject the vapor analytes into the column. The Knudsen pump was supplied with 1.1 W power, providing a N_2 flow rate of 0.2 sccm; the N_2 carrier gas was supplied by a Tedlar bag connected upstream of the system. Temperature programming of the separation column was not used in this experiment. The detector was operated at 1 Hz (1 pulse /sec.) frequency. A customized LabVIEW® program was used to control the overall operation of the *iGC1* system.

2.5. Discussion and Conclusion

This work demonstrates the feasibility of using a standardized fabrication approach to manufacture a fluidic microsystem for gas chromatography, including a pump, a preconcentrator, a separation column and a detector. The fabrication process is low cost and standardized, showing promise of wider adoption of μGC technology. The assembly procedure described in this effort mainly focuses on die-to-die assembly after dicing. However, as noted earlier, wafer-to-wafer assembly prior to dicing can also be envisioned, enabling batch mode fabrication.

The 4-cm^3 *iGC1* system demonstrates that it is possible to mitigate thermal crosstalk between components to achieve a small form factor. The properties of the system are summarized in Table 2.2. Discharge-based detectors are stable over time because the emission spectra are characteristics of the chemical species present. The detection rate is mainly limited by the duration of plasma afterglow, which is typically less than 20 ms [Mit08], corresponding to a detection rate of over 50 Hz. Nevertheless, the discharge-based detector requires special considerations because of background noise in an air ambient, and the need for high voltages. The miniaturization of spectrometers has previously been demonstrated [Que05], and versions as small as 19 cm^3 are commercially available (Model # Qstick, RGB Lasersysteme GmbH, Germany [RGB15]), indicating the feasibility of a fully integrated system.

The use of epoxies in the system assembly provides a low-temperature (*i.e.,* less than 200°C) and low-cost solution. The epoxies are chosen for low out-gassing properties and are sufficiently cured, minimizing the out-gassing problem. In preliminary studies, significant out-gassing was not observed, but the effects of higher temperatures remain unclear. As an alternative, spin-on-

glass may be used for component assembly. It is expected not to contribute interferences to the chromatography, but its curing temperature is typically above 400°C.

Table 2.2: Summary of the system characteristics.

***iGC1* volume**	≈3.7 cm^3
***iGC1* weight**	≈5 grammes
Power	typically ≈1.5 W
Operation time	typically ≈6 min.
External hardware	Heat sink
	Spectrometer
	Control electronics

The effort of integrating a micro gas pump into the *iGC1* system provides a path for realizing a complete micro analytical system. The stackable architecture provides interchangeability, *i.e.*, different component designs can be readily fitted into the system, tailoring it for various applications. The analytical capability of the system can be extended to more complex gas environments by reconfiguring the system, such as direct stacking of more separation columns or even implementing a 2DGC system. Beyond the preliminary experimental results shown in this effort, more options of the *iGC1* operation are possible, such as the combination of temperature programming and flow programming (readily provided by the Knudsen pump [Liu11]). Although the Knudsen pump utilized in this design does not provide optimal flow for the preconcentrator, future designs are expected to resolve this matter.

Chapter 3:

iGC2: an Architecture for Micro Gas Chromatographs Utilizing Integrated Bi-Directional Pumps and Multi-Stage Preconcentrators

This chapter reports an integrated micro gas chromatography (μGC) architecture which utilizes a bi-directional micropump. Four integral components – the bi-directional Knudsen pump (KP2), a two-stage preconcentrator-focuser (PCF2), a separation column, and a gas detector – are integrated in a 4.3 cm^3 stack, forming a serial flow path. All four components are fabricated using the same 3-mask process. Compared to the conventional approach used with multi-stage preconcentrators, in which valves are used to reverse flow between the sampling phase and the separation phase, this μGC architecture reduces the overall complexity. In this architecture, the vapors being sampled are drawn through the detector and column before reaching the PCF2. The microsystem operation is experimentally validated by quantitative analyses of benzene, toluene, and xylene vapors ranging in concentration from 43-1167 mg/m^3.

3.1. Introduction

Following the pioneering work of Terry *et al*. [Ter79], a variety of micro gas chromatography (μGC) systems have been reported over the past three decades. Many μGC systems include microfabricated renditions of three components that are integral to the system: the preconcentrator, which samples vapor analytes and provides vapor injection; the column, which separates the vapor analytes; and the gas detector, which quantifies the eluents from the column [Gor12, Lew06,

Man11, Zam09]. These systems use external, commercial pumps to provide gas flow. More recent systems utilizing micropumps have also been demonstrated [Kim07, Liu11, Qin13]. Some systems use commercial valves to control fluidic routing; microfabricated valves for μGC systems are being studied [Lew06].

In the simplest architectures, the preconcentrator, column, detector, and pump are connected in series, and operated with unidirectional flow from the preconcentrator to the column and then the detector [Gor12, Qin13]. In others, a valve bypasses the column during vapor sampling to increase the flow rate, but the flow direction in both sampling and analytical separation remains the same [Adk09, Lew06]. The bypass-flow architecture can be further enhanced by an additional detector in the bypass line that provides a coarse measurement of the vapor concentration and informs the system of the optimal sampling time [Adk09]. In more complex architectures, a number of valves are used to reverse the flow direction in the preconcentrator during sampling and separation (*i.e.*, bi-directional flow is necessary) [Col13, Kim11, Lu05]. As a consequence, during the sampling phase vapors enter the preconcentrator at the end which will be downstream during the analytical separation phase.

While bi-directional flow is potentially beneficial for a single-stage preconcentrator, it is essential for a multi-stage (or multi-bed) one. A multi-stage preconcentrator uses various types of sorbents for analyses of vapor analytes of broad ranges of volatilities. The stages, each packed with one type of sorbent, are connected in series. During the vapor sampling phase, analytes with low volatility are trapped in stages that are upstream in the sampling flow path; these stages are packed with sorbents of low surface area. Analytes with high volatility, after passing through the upstream stages, are trapped in downstream stages, which are packed with sorbents of high surface

area (Fig. 3.1). During the analytical separation phase, the flow direction is reversed, allowing all the trapped analytes to be injected into the separation column [Tia05].

Miniaturization of valves has been a subject of extensive research [Oh06]. Many of the microvalves reported to date utilize the actuation of a flexible diaphragm to control flow. This actuation has been performed electrostatically [Rob98], piezoelectrically [Par09], or thermopneumatically [Hen98]. A microvalve targeting μGC integration has been reported [Pot12]. However, the use of a deformable diaphragm introduce additional cost, complexity, and reliability challenges to a multi-component μGC system that is already complex. This chapter evaluates a valveless μGC architecture, the *iGC2*, which is comprised of a bi-directional Knudsen pump (KP2), a two-stage preconcentrator (PCF2), a separation column, and a detector. Its operation is illustrated in Fig. 3.1. During the sampling phase, vapor analytes enter the system, pass through the detector and column, and finally settle into the PCF2. During the analytical separation phase, the flow direction is reversed by the KP2; the sampled vapor analytes are then thermally desorbed from the PCF2, separated in the column, and quantified by the detector.

Valveless bi-directional operation is more amenable to μGC systems than to conventional benchtop GC systems. In contrast to conventional columns that are usually 10-30 m long, microcolumns typically have relatively small lengths of 0.08-3 m [Aga05, Lew06, Nar12]. Qualitatively, the short microcolumns have small "breakthrough" volumes, *i.e.*, vapors can easily pass through the column and reach the preconcentrator during sampling. At the end of the sampling period, residual vapors may remain in the column. When flow is reversed to initiate the separation phase, these vapors in the column are purged, but may contribute to a baseline response upon which the retention peaks are superposed. By accommodating these trends into the quantitative assessment of retention peaks, quantitative analyses are not compromised.

The design of the *iGC2* system is described in Section 3.2; fabrication is described in Section 3.3; experimental results are presented in Section 3.4, followed by the discussion and conclusion in Section 3.5.

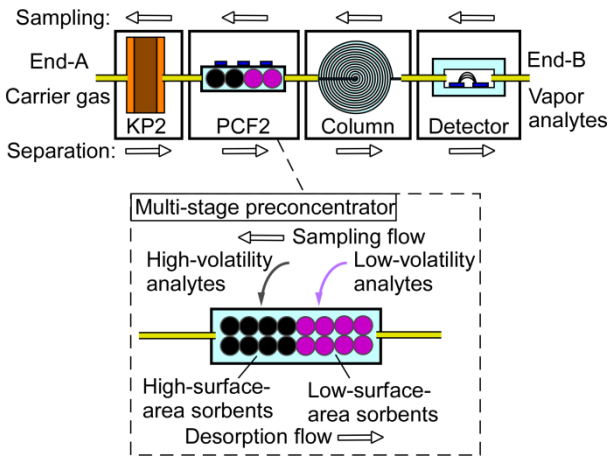

Fig. 3.1: Bi-directional operation of the *iGC2* system. During vapor sampling, the KP2 draws vapor analytes through the detector and column, and into the PCF2. The two stages of PCF2 target analytes with different volatility ranges. The flow is reversed during analytical separation.

3.2. Design

Bi-directional Knudsen pump (KP2)

Knudsen pumps are motionless gas pumps that operate on the principle of thermal transpiration [Knu09, Rey79]. One type of Knudsen pump implementation utilizes nanoporous mixed cellulose ester (MCE) membrane(s) (of thickness ≈105 μm, pore diameter ≈25 nm, porosity ≈70%, Millipore, MA) [Gup11]. In the presence of a temperature gradient, flow is generated from the cold side to the hot side of the MCE membrane(s). A previously reported bi-directional Knudsen pump used thermoelectric elements to apply reversible temperature gradients across the MCE membrane(s) [Pha10]. In the *iGC2* architecture, however, the KP2 simply utilizes thin-film Joule heaters on both sides of a membrane stack. During operation, one of the sides is heated while the other is cooled passively (by a heat sink or natural convection).

The KP2 has a stack of four MCE membranes sandwiched by two glass dice on each side, *i.e.*, *Side-A* and *Side-B*, (Fig. 3.2). Each glass die is ≈500 μm thick. On *Side-A*, the glass die that is in contact with the MCE membrane stack (*i.e.*, Die 2a) has a thin-film metal heater and thermistor to control the temperature, as well as multiple through-holes to facilitate gas flow into and out of the MCE membranes. The other glass die (*i.e.*, Die 1a) has in-plane grooves that guide gas streams to a single port, which can be connected to other components or external test setup. The constituent glass dice on *Side-B* (*i.e.*, Die 1b and Die 2b) are identical to Die 1a and Die 2a, respectively.

In the *iGC2* stack assembly (Fig. 3.2), *Side-B* is attached to the rest of the stack, whereas *Side-A* is attached to an external heat sink. During analytical separation, *Side-B* is heated while *Side-A* is cooled by the heat sink. During vapor sampling, *Side-A* (and the heat sink) is heated while *Side-B* is cooled by natural convection together with the rest of the stack.

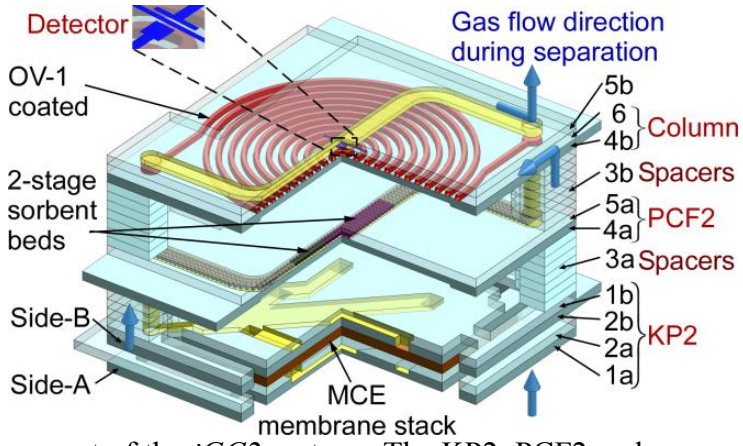

Fig. 3.2: Structural concept of the *iGC2* system. The KP2, PCF2, column, and detector are stack integrated. Spacers are used to provide inter-layer flow connection.

Two-stage preconcentrator (PCF2)

Previously reported microfabricated multi-stage preconcentrators used multiple chambers, each containing one type of sorbent [Lu05, Tia05]. In the *iGC2*, however, the PCF2 contains only one chamber designed in the shape of a channel; the two stages are formed by packing different

sorbents in sequence. This design mimics its macro-scale counterpart: the multi-bed thermal desorption tube. It can be configured to include more than two stages without redesign.

The PCF2 consists of a channel (width ≈1 mm, depth ≈200 μm) formed by Die 4a and Die 5a (Fig. 3.2). The channel is packed with four segments of particles in series: glass beads (with diameter 150-180 μm, Sigma Aldrich, WI); Carbograph 2 (with surface area ≈10 m^2/g, diameter 120-150 μm, Grace Davison Discovery Sciences, IL); Carbopack B (with surface area ≈100 m^2/g, diameter 112-140 μm, Sigma Aldrich, WI); glass beads (with diameter 150-180 μm, Sigma Aldrich, WI). The segment of Carbograph 2 is intended to trap vapors of lower volatility (*e.g.*, toluene and xylene), and the segment of Carbopack B is intended to trap vapors of higher volatility (*e.g.*, benzene). The two segments of glass beads, one at each end of the PCF2 channel, are used to confine the two segments of sorbents in the central region of the device, where the temperature is the highest during thermal desorption.

The PCF2 has advantages over our prior preconcentrator design [Qin13] because its narrower channel dimension provides less sensitivity to the non-uniformity of sorbent packing, as well as higher flow velocity at a given volumetric flow rate. A future design can be improved, presumably, by incorporating the pillar structures and sorbent loading port [Qin13, Seo12].

Column, detector, and the stacked iGC2 system

The *iGC2* separation column is a channel (of length ≈25 cm and hydraulic diameter ≈230 μm) coated with a layer of ≈0.2 μm thick non-polar polydimethylsiloxane (PDMS or OV-1, Ohio Valley Specialty, OH) that serves as the stationary phase [Qin13]. The column is formed by Die 4b and Die 6 (Fig. 3.2). When passing along the separation column, vapor mixtures partition between the stationary phase material and the carrier gas. The non-polar PDMS stationary phase used in this work interacts with the vapor molecules mainly by van der Waals force [Bar04]. Vapor

molecules with higher molecular weight typically have a stronger interaction with the stationary phase and display a longer retention time. Additionally, thicker coatings of the stationary phase provide a stronger interaction with the vapor molecules and extend retention times.

The gas detector consists of two thin-film metal electrodes on a glass substrate (*i.e.*, Die 6). In this work, the metal layer consists of Ti/Pt of thickness 25/100 nm. The two electrodes (i.e., anode and cathode) are spaced 50-200 μm apart. Electrodes of other materials, thickness, and separation can also be used. The groove in Die 5b forms the detector channel that guides gas flow over the electrodes (Fig. 3.2). By applying a voltage pulse between the two electrodes, a microdischarge is generated. The resulting optical intensity at the line that is specific to the C-H emission can be used to quantify carbon-containing species in the gas flow [Mit08, Qin13]. In contrast to flame ionization detectors (FID) that are often used within commercial GC systems, microdischarge based detectors do not require a stored supply of H_2 to create the ionization, and are more amenable to monolithic integration.

The KP2, PCF2, column, and detector are integrated in the form of a stack (Fig. 3.2 and Fig. 3.3), that also uses fourteen 500 μm-thick glass spacers (Dice 3a and Dice 3b). The spacers provide thermal isolation between adjacent components. Perforations in the spacers allow inter-layer flow. The dashed line in Fig. 3.3 indicates the gas flow path of the system.

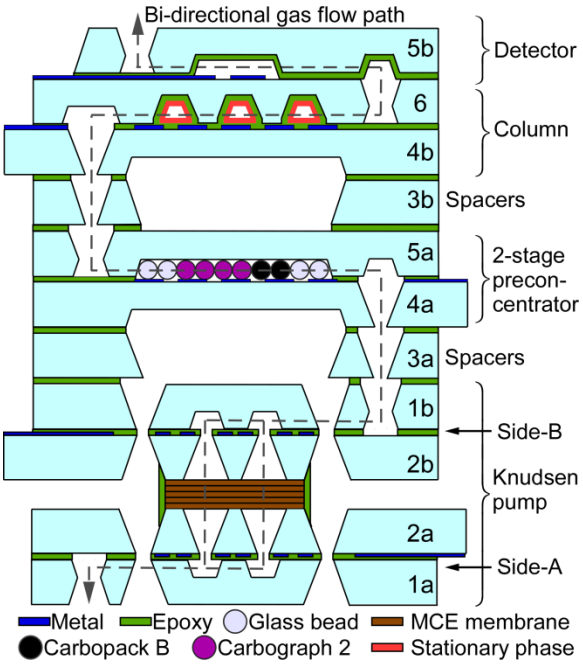

Fig. 3.3: Illustration of the cross-section of the *iGC2* system. The four components – pump, preconcentrator, separation column, and detector – form a serial gas flow path, as indicated by the grey dashed line.

3.3. Fabrication

The constitutive elements of all four *iGC2* components, as well as the spacers, are fabricated on glass wafers using the same three-mask lithographic processes. Hence, these elements may be either fabricated on separate wafers or all on a single wafer. The use of glass as the substrate material has several benefits. It is lower in cost than silicon and ceramic options, and can be easily micromachined. In addition, the transparent nature of glass permits visual inspection of the interior of the devices, which benefits early stage research and development.

First, a Ti/Pt thin film (of thickness 25/100 nm) is deposited and patterned to form heaters, thermistors, and discharge electrodes (using Mask #1). The glass wafer is micromachined on both sides by sandblasting (Bullen, Inc., OH) to create fluidic channels and thermal-isolating cutouts (using Mask #2-3).

After wafer dicing, the glass dice are assembled together. The constituent dice of the separation column are spin-coated with an SU-8 (MicroChem, MA) layer, which, smoothens the sandblasted surface and also serves as an adhesive between dice. The column is also coated with the OV-1 stationary phase using a static coating method, in which an OV-1/pentane solution is first filled into the column and subsequently the pentane is evaporated under vacuum [Rei06]. The resulting thickness of the stationary phase is expected to be in the range of 0.2 μm. The other dice are held in place by a low-viscosity epoxy (Model # Epotek 377, Epoxy Technology, Inc., MA). The MCE membrane stack of the KP2 is sealed around the perimeter by a viscous epoxy (Model # Stycast2850FT, Henkel, Germany).

The PCF2 is packed with sorbent particles. In this preliminary PCF2 design, which does not have embedded features to confine the sorbent particles, a small segment of capillary tube (with inner diameter ≈100 μm, length ≈2 mm) is attached to one end of the channel. With a gentle vacuum applied at this end, the sorbent particles and glass beads are drawn into the PCF2 channel [Seo12], in sequence, from the other end, which is later attached to another similar segment of capillary tube.

The four components and the spacers are finally integrated into a stack. Adhesion between the components and spacers is provided by either an epoxy or a wax bond layer. Photographs of the fabricated components and system are shown in Fig. 3.4. The *iGC2* system has a footprint of 1.8 × 2.0 cm^2 and a volume of 4.3 cm^3.

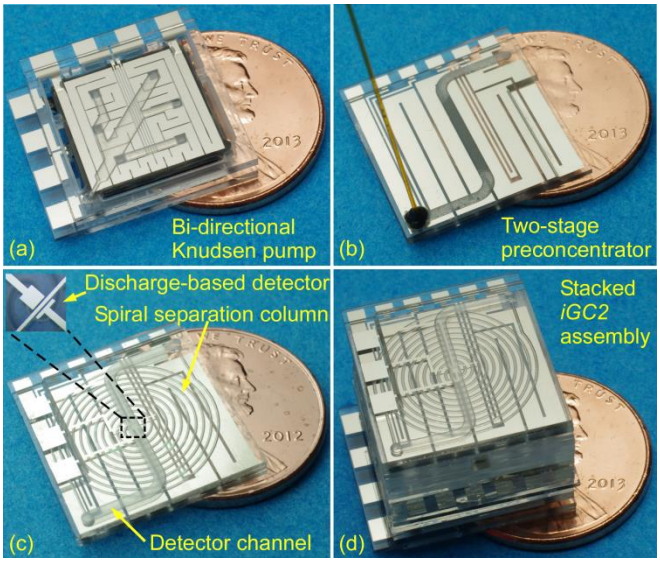

Fig. 3.4: Photographs of the *iGC2* system. (a) The KP2, (b) the PCF2, (c) the separation column and the discharge-based detector, and (d) the *iGC2* system, which has a footprint of 2×1.8 cm^2 and a volume of 4.3 cm^3.

3.4. Experimental Results

In order to characterize their performance, the KP2 and PCF2 were separately evaluated without assembly into the full *iGC2* system. The experimental evaluations focused on the aromatic hydrocarbons benzene, toluene, and *m*-xylene (BTX), which are typical indoor pollutants.

KP2

The KP2 was evaluated by measuring its pressure-flow characteristics. As indicated in Section 3.2, *Side-A* of the KP2 was attached to an aluminum block that served as a heat sink. In the evaluation of the standalone pumps, *Side-B* was not attached to the other *iGC*2 components. As shown in Fig. 3.5, a commercial pressure sensor (Model # MPX5010DP, Freescale Semiconductor, AZ) and a flow meter (Part # FMA-1603A, Omega Engineering, CT) were used to monitor the pressure head and flow, respectively. Although the former had a rated maximum error of ±500 Pa (including offset variation), the actual error was expected to be much smaller, because it was used at room temperature within a small pressure range and corrected for offset. The latter had a rated

error of ±0.02 sccm. Varying flow loads (manifested as capillary tubes with varying lengths and inner diameters) were used to obtain various pressure-flow points. The values of the loads were selected to span a wide range covering the actual load provided by the rest of the *iGC2* system.

With 1.3 W power applied on *Side-B*, the pumps typically provided a steady state air flow rate of 0.52 sccm for a pressure head of 413 Pa; the blocking pressure head, at which the flow was reduced to zero, was 1254 Pa. This direction of flow is intended for the analytical separation. In the opposite direction, with 3.3 W power applied on *Side-A* (with the heat sink still in place, and *Side-B* cooled only by natural convection), the pump provided a steady state air flow rate of 0.11 sccm against a pressure head of 87 Pa; the blocking pressure was 302 Pa (Fig. 3.5). In general, the relationship between the input power of the KP2 and the flow rate are approximately linear for intermediate pressure heads.

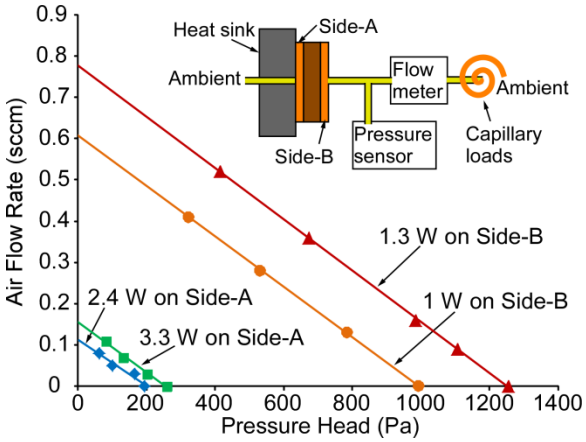

Fig. 3.5: The test setup and steady state performance of the KP2. The data points were obtained by altering the capillary loads and were linearly fitted to indicate the characteristic lines of the KP2.

PCF2

The PCF2 was characterized for both adsorption and desorption of BTX. The adsorption capability of preconcentrators is often characterized by the time taken for the vapor analytes flowing through the component to saturate the concentration measured at the exit; this is known as "breakthrough" [Tia05]. For the PCF2, the inlet (for vapor sampling) was connected to a 2 L

dilution bottle (Sigma Aldrich, WI) containing the vapor of benzene, toluene, or *m*-xylene in N_2. The component BTX vapors were individually drawn by a vacuum pump through the PCF2 at flow rates of 0.1, 0.3, and 0.4 sccm. A fixed volume (100 µL) of vapor exiting the PCF2 was periodically routed, by a six-port valve to an FID within a commercial GC (Model # Agilent 6890).

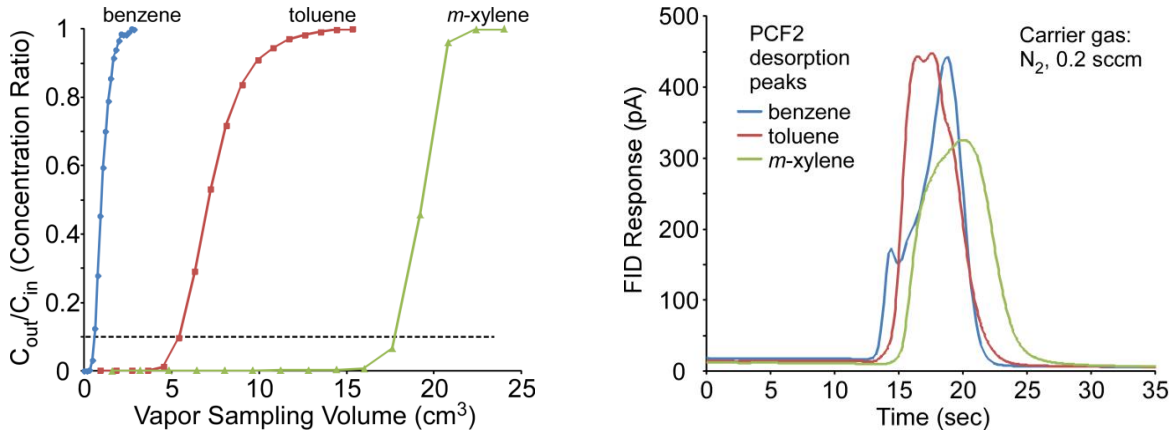

Fig. 3.6: Evaluation of the performance of the PCF2. (a) The outlet BTX concentration response (normalized to the inlet concentration) during vapor sampling. (b) BTX desorption peaks with 0.2 sccm N_2 flow after sampling 1 cm^3 of vapor.

In Fig. 3.6a, the BTX concentrations at the preconcentrator outlet c_{out} are normalized to that at its inlet c_{in}; the vapor sampling volume is calculated as the product of sampling flow rate and sampling time. Conventionally, the breakthrough criterion is selected at the point when c_{out}/c_{in} reaches 10% [Tia05]. Using this criterion, the PCF2 in this effort had breakthrough volumes of 0.5 cm^3, 5.4 cm^3, and 17.6 cm^3 for benzene, toluene, and *m*-xylene, respectively.

The thermal desorption characteristics of the PCF2 were evaluated by the desorption peaks observed in chromatograms. The PCF2 was first used to sample an individual analyte vapor (*i.e.*, benzene, or toluene, or *m*-xylene) at 0.1 sccm for 10 min. Then it was connected upstream of the FID and downstream of an injection port in a commercial GC (Agilent 6890), which provided a 0.2 sccm N_2 flow in the opposing direction, matching the flow to be provided by the KP2 during the analytical separation phase in the *iGC2*. Desorption was performed by applying a 10.5 W

pulse to the integrated thin-film heater, which heated the PCF2 to 180°C in 10 sec, immediately followed by a 2.7 W pulse for 5 sec, which maintained this temperature. This relatively modest heating rate was selected for superior control and uniformity, while reducing the likelihood of stress fractures in the device, even though sharper desorption peaks are achievable with higher power.

Typical values of the resulting peak widths measured at half height (PWHH) were 3.2 sec, 4.6 sec, and 6.3 sec for benzene, toluene, and *m*-xylene, respectively (Fig. 3.6b). Only minimal tailing was observed. Full desorption was achieved during the first thermal pulse, as verified by a second thermal pulse that did not provide any additional desorption peak.

The preconcentration factors were calculated by the volume ratios of the vapor sample to the thermal desorption, *i.e.,* the product of the sampling flow rate and the sampling time divided by the product of the desorption flow rate and the desorption PWHH [Nam88]. As calculated from Fig. 3.6b, the preconcentration factors for toluene and *m*-xylene were 65 and 48, respectively. The value for benzene cannot be obtained from Fig. 3.6b, because the 1 cm^3 sampling volume substantially exceeds its breakthrough volume (as illustrated in Fig. 3.6a). By sampling benzene and toluene with their breakthrough volumes, preconcentration factors of 25 and 236 were obtained. A preconcentration factor of 143 was obtained for *m*-xylene with a sampling volume of 3 cm^3. A thorough parametric sweep can identify the maximum preconcentration factors, but it is beyond the scope of this effort.

Column and detector

The separation columns were evaluated in an Agilent 6890 GC with a vapor injection port located upstream and an FID located downstream [Qin13]. To provide a better demonstration of the separation capability of the column, the columns were used to separate BTX and 5 interfering

alkanes (C_5-C_9) at room temperature, with N_2 carrier gas flowing at 0.2 sccm to mimic the KP2. The 8 analytes were separated in less than 2 min. (Fig. 3.7).

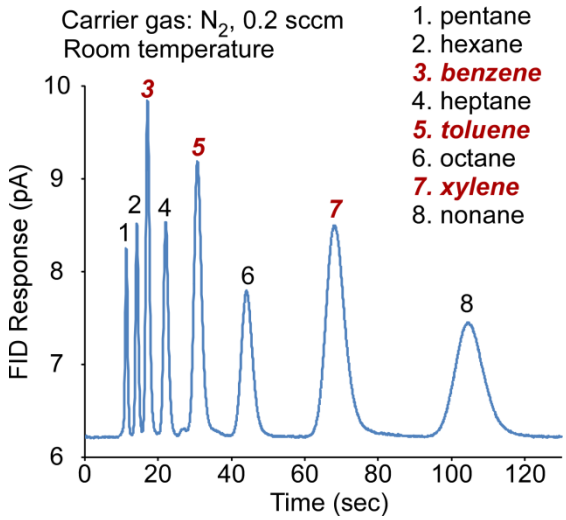

Fig. 3.7: Typical separation of BTX and 5 alkanes provided by the column at room temperature. The injector and FID in an Agilent 6890 GC were used for testing the column.

The discharge-based detector was operated with 3-5 ms voltage pulses of 800-1600 V. A handheld spectrometer (Model # USB 2000, Ocean Optics, FL) was used to monitor the optical emission [Qin13]. As expected, the microdischarge showed strong optical emissions for N_2 within a wavelength range of 300-400 nm. The emission intensity at 388 nm, which is a characteristic line of C-H species, was used to quantify the BTX vapors eluting the column. To minimize the effect of pulse-to-pulse variation in emission intensity, the emission peaks at 388 nm were ratioed to the peaks for the N_2 line at 337 nm [Mit08]. The detector was operated at 1 Hz (1 pulsed detection/sec). With each microdischarge requiring ~10 mJ energy, the average power consumption was in the range of 10 mW, which was negligible compared to the power consumption of other *iGC2* components (*i.e.*, the KP2 and PCF2). It is notable that such detectors can be operated at even lower energy levels [Mit08].

The stacked iGC2 system

Fully assembled *iGC2* systems were tested in two manners. In the first set of experiments, the discharge-based detector in the stacked system was not activated. Instead, the FID in an Agilent 6890 GC was used to evaluate the impact of the fluidic architecture upon the output. In the second set of experiments, the detector was utilized together with all other components, demonstrating the operation of the full system.

Vapor samples for these tests were prepared by evaporating liquid phase benzene, toluene, and *m*-xylene (each 0.1-2.7 μL) in a 2 L dilution bottle, resulting in vapor concentrations ranging from 43-1167 mg/m^3. The bottle and the *iGC2* system were previously purged using ultra-high-purity N_2 to minimize any impurities that might affect the evaluation of the system. With the bottle connected to *End-B* (Fig. 3.1) of the *iGC2* system, the KP2 was used to provide a sampling flow of 0.05 sccm for 5-15 min. (using 3.3 W input power), drawing 0.25-0.75 cm^3 of the vapor through the detector and the column into the PCF2. Then the system was allowed to cool down naturally for ≈10 min.

In the first set of experiments, *End-B* (Fig. 3.1) of the *iGC2* system was then connected to the FID, whereas *End-A* remained open to ambient room air, which served as the carrier gas. The KP2 was then powered up to 1.3 W to provide 0.2 sccm air flow for 20 sec. before the PCF2 was powered up. This delay ensured a sufficient flow to be established prior to the analytical separation. The eluent from the column was identified and quantified by the FID. With each BTX vapor sample the tests were repeated four times in succession, using identical operating conditions in order to evaluate repeatability. Typical results are shown in Fig. 3.8; the repeatability is evident. As expected, the retention peaks of BTX appear as superposed onto a baseline response. The system operation parameters are summarized in Table 3.1.

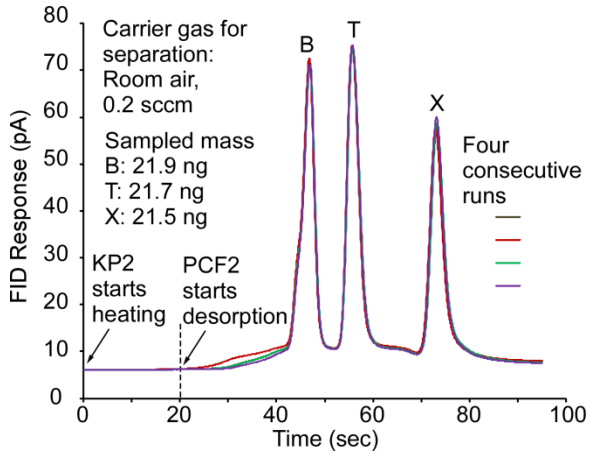

Fig. 3.8: Four consecutive runs of BTX separations provided by a fully assembled *iGC2* system operated with a commercial FID. In each run, the system was used to analyze the same BTX vapor with the same sampling volume.

Table 3.1: Summary of the *iGC2* operation.

Component	Operation parameters		Figure
KP2	Sampling: 3.3 W, 0.05 sccm Separation: 1.3 W, 0.2 sccm		Fig. 3.8-Fig. 3.11
PCF2	Desorption: temperature ramped to 180°C in 10 sec using 10.5 W, and maintained for 5 sec using 2.7 W.		Fig. 3.6b Fig. 3.8-Fig. 3.11
Column	Separation without active temperature programming		Fig. 3.8-Fig. 3.11
Discharge-based detector	Detection rate: 1 Hz; ~10 mW power		Fig. 3.11
***iGC2* system**	Sampling time	BTX concentration	
	10 min	43 mg/m^3	Fig. 3.8
	10 min	43-328 mg/m^3	Fig. 3.9
	5-15 min	43 mg/m^3	Fig. 3.10
	15 min	573-1167 mg/m^3	Fig. 3.11

Continuing the first set of experiments performed with the FID detector, in order to demonstrate quantitative analysis, samples of BTX vapors were prepared with concentrations varying from 43-328 mg/m^3. Using the same *iGC2* parameters (Table 3.1), the vapors were sampled at 0.05 sccm for 10 min., resulting a vapor sampling volume of 0.5 cm^3 and sampled masses of 22-164 ng. The FID chromatograms of the separations are shown in Fig. 3.9a. To verify quantitative analysis, the areas of the retention peaks in the chromatograms (Fig. 3.9a) were calculated by subtracting from the peak response the underlying baseline area (Fig. 3.9b). The data points were fitted by straight lines connecting to the origin of the coordinate system, resulting in $R^2 \geq 0.9987$, which indicates good linearity of the system response for quantitative analysis.

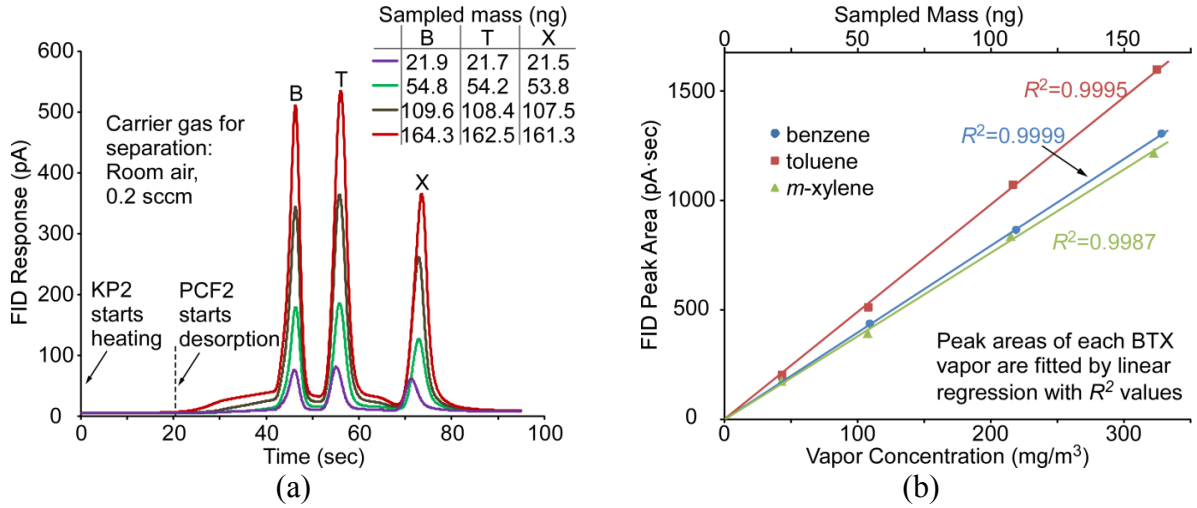

Fig. 3.9: Quantitative separations provided by the *iGC2* system. (a) FID chromatograms of BTX vapors with the same sampling volume and various concentrations (and consequently various sampled mass). (b) Calculation of peak areas after subtraction of baseline areas, representing the analyzed masses.

In addition, sampling volumes were varied in the 0.25-0.75 cm^3 range (Table 3.1). This was performed by varying the duration of the sampling period from 5-15 min. The resulting FID chromatograms and calculated peak areas are plotted in Fig. 3.10a and b, respectively. In Fig. 3.10b, the intercepts on the horizontal axis indicates the threshold volumes, *i.e.*, the product of sampling times and flow rate taken by the vapor to pass through the column and detector before reaching the PCF2. As configured, the *iGC2* had threshold volumes of 0.02, 0.1, and 0.23 cm^3 for BTX, respectively. The sampling of benzene started to saturate when the sampling volume exceeded 0.4 cm^3, corresponding to the breakthrough of benzene in the PCF2.

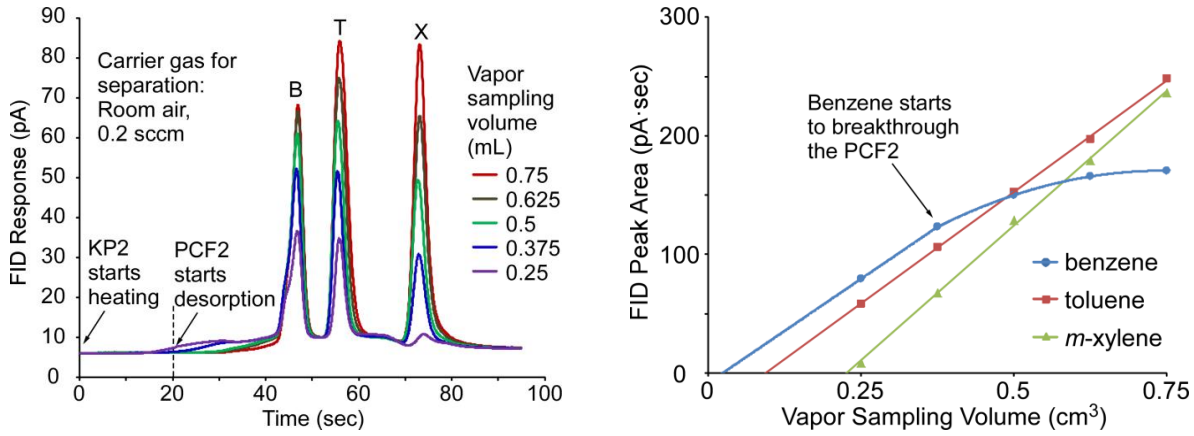

Fig. 3.10: Characterization of the *iGC2* sampling operation. (a) FID chromatograms of the same BTX vapor with various sampling volumes. (b) Calculation of the peak areas. The intercepts on the horizontal axis indicate the threshold volumes (*i.e.*, the volumes taken by the vapors to pass through the column during sampling).

In the second set of experiments conducted with fully assembled *iGC2* systems, the sampling procedure remained the same as the first set, as did the operating parameters (Table 3.1). Samples of BTX with concentrations of 573-1167 mg/m^3 were analyzed. To reduce the noise from spectal emissions of air, N_2 was used as the carrier gas by connecting an N_2-filled Tedlar® bag to *End-A* (Fig. 3.1) of the *iGC2* system. The resulting emission-intensity chromatograms (Fig. 3.11a) demonstrate separations of BTX with retention times similar to those shown in Fig. 3.8, Fig. 3.9a, and Fig. 3.10a. However, the peak heights of *m*-xylene are much smaller than those of toluene in Fig. 3.11a. This is different from the FID chromatogram obtained with the same vapor sampling volume in Fig. 3.10a, where toluene and *m*-xylene show similar peak heights. Additionally, the baseline fluctuations are not observed in Fig. 3.11a. The calculated peak areas demonstrate positive correlations with sampled vapor concentrations, showing promise of quantitative analyses (Fig. 3.11b). However, in contrast to Fig. 3.9b, the peak areas in Fig. 3.11b are not proportional to the vapor concentrations. This underscores the need for establishing the relationship between spectral intensity and vapor concentration for various analytes.

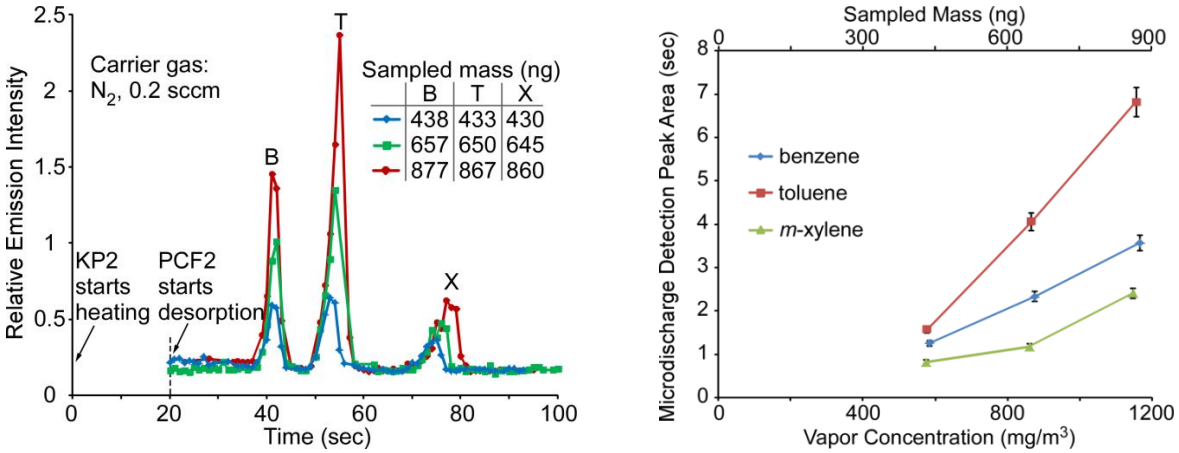

(a) (b)

Fig. 3.11: Characterization of the *iGC2* sampling operation. (a) FID chromatograms of the same BTX vapor with various sampling volumes. (b) Calculation of the peak areas. The intercepts on the horizontal axis indicate the threshold volumes (*i.e.*, the volumes taken by the vapors to pass through the column during sampling).

3.5. Discussion and Conclusion

Overall, the experimental results validate the functionality of a valveless μGC architecture that utilizes a bi-directional micropump with a two-stage preconcentrator. Further, the results are repeatable, and quantitative analysis appears possible despite the modest flow rates provided by the motionless pump. The facile nature of the fabrication process holds promise for eventually developing a low-cost system. A number of observations can be made about the constitutive components and future work.

In contrast to a previously reported approach of using thermoelectric elements to implement a bi-directional Knudsen pump [Pha10], the direct integration of heaters on both sides of the thermal transpiration membranes in the KP2 compromises flow rate in the sampling period (Fig. 3.5) for structural simplicity. Nevertheless, the small sampling flow rate can be compensated by extending the sampling period. In principle, bi-directional flow can also be achieved by two opposing uni-directional pumps. In that case, however, each pump would be required to overcome the flow resistance of the other, which is less efficient than the use of a single bi-directional pump.

In the analytical separation periods, PCF2 provided 3-6 sec.-wide desorption peaks under the modest flow rate (≈0.2 sccm) available from KP2. Although the width of these desorption peaks may have contributed to the broadening of the retention peaks, quantitative analyses are evidently possible, as long as the retention peaks reach baseline-separation, *i.e.*, a condition where the signal returns to the baseline between consecutive peaks (as demonstrated in Fig. 3.9). The dual-peak shapes of the benzene and toluene desorption in Fig. 3.6(b) are likely the result of the two stages within the PCF2 desorbing under a modest heating rate: the stage packed with Carbograph 2 desorbs slightly before the stage packed with Carbopack B.

It is notable that the relative heights of retention peaks measured by microdischarge-based detection (Fig. 3.11a) are different from those measured by the commercial FID (Fig. 3.10a). This is likely related to the difference between the two ionization methods that are involved. However, even with microdischarge-based detection, the calculated areas of the retention peaks are correlated to vapor concentration, demonstrating promise for quantitative analyses. This is encouraging, given the simple and unsealed nature of the microdischarge-based detector. The use of an N_2 carrier gas, and ambient contaminants can, however, increase the spectral noise [Hos11, Wil03].

The overall system power consumption can be estimated from Table 3.1. For a vapor sampling time of 10 min. and separation duration of 1.5 min., the average system power consumption is 3.2 W, which is dominated by the KP2 operation during the vapor sampling phase. This power consumption is higher than those of some of the previously reported systems (*e.g.*, 0.7 W in [Gor12], which uses a commercial pump), because of the inefficiency of the KP2 heat sink when driving flow during vapor sampling. Nevertheless, despite the relatively high power consumption, the Knudsen pump is still an attractive candidate for μGC integration, because of its compactness,

simplicity in fabrication, and ultra-high reliability [Gup11]. Thermal optimization of the system design and overall assembly are expected to reduce the power consumption.

A number of improvements can be envisioned for future designs of the *iGC2*. For example, a longer column can provide better separation of retention peaks, and heating of the column both during sampling and separation is likely to improve various aspects of the performance. In addition, the use of sorbents with higher surface area within the PCF2 would permit analyses of vapors with lower concentrations. All these approaches are intended to analyze more complex vapor mixtures. Nonetheless, a more powerful micro gas pump may be required to maintain the gas flow rate in a longer column. This can be accomplished by a multi-stage Knudsen pump. The stackable architecture in this work provides a simple and compact integration of the system, as well as the scalability to longer columns (by stacking multiple short columns). However, it is difficult for the stackable architecture to accommodate a multi-stage Knudsen pump, which requires more thermal isolation between multiple heaters and heat sinks. New architectures for multi-stage Knudsen pumps are currently under investigation.

The packaging of the system is still under investigation. One possibility is a case with embedded heat sink, circuit board, and fittings for a mini-spectrometer. The lead transfer from the components to the circuit board could be accomplished by pin assemblies.

Chapter 4:

iGC3: a Fully Electronic Microfabricated Gas Chromatograph with Complementary Capacitive Detectors for Indoor Pollutants

This chapter reports a complete micro gas chromatography (μGC) system, named *iGC3.c2*, in which all the components are lithographically microfabricated and electronically interfaced. All components include a bi-directional Knudsen pump, a preconcentrator, separation columns, and capacitive gas detectors, forming a complete μGC system with a foorprint of ≈8×10 cm^2. All the fluidic components of the system are fabricated by a common three-mask lithographic process. The Knudsen pump is a thermomolecular pump that provides air flow to the μGC without any moving parts. The film heaters embedded in the separation columns permit temperature programming. Two capacitive detectors provide complementary response patterns, enhancing vapor recognition and resolving co-eluting peaks. The system uses room air as carrier gas. The system is used to experimentally demonstrate analysis of 19 chemicals with concentration levels of parts-per-million and parts-per-billion in room air. The tested chemicals include alkanes, aromatic hydrocarbons, aldehyde, halogenated hydrocarbons, and terpenes. This set of chemicals represents a variety of common indoor air pollutants, among which benzene, toluene, and xylenes (BTX) are of particular concern.

4.1. Introduction

Volatile organic compounds (VOCs) are common contributors to indoor air pollution. The species of interest include aromatic hydrocarbons, such as benzene, toluene, and xylenes (BTX), as well as alkanes, halogenated compounds, alcohols, aldehydes, ketones, terpenes, *etc*. These VOCs are typically found in higher concentrations in indoor environments than outdoors [Bro94, Kos95]. The exposure limits of these VOCs are typically in the range of 1-100 ppm [Occ15]. Certain species constitute severe health hazards – for example, benzene is a known carcinogen [Huf07].

Although VOCs can be collectively detected by a variety of standalone gas detectors, these typically lack the selectivity to discriminate between constituents of complex mixtures [Bon08]. Whereas simple mixtures can be analyzed by mass spectrometry and infrared spectroscopy systems [Stu00, Wes08], gas chromatography systems are typically needed for complex mixtures [Bar04]. For pervasive deployment in households, offices, and public facilities, microfabrication offers a pathway to reducing system cost. A system deployed for long-term indoor VOC monitoring should ideally be capable of performing automated sampling and analyses without requiring consumables or frequent replacement of components. Power consumption is not a critical concern, as power sockets are widely available in indoor environments.

Since the late 1970s, a variety of micro gas chromatography (μGC) systems have been reported, in which a subset of the necessary components have been microfabricated lithographically [Ter79]. Most commonly, the separation column is micromachined. Micromachined preconcentrators have been reported for sampling and injection of low-concentration VOCs into the columns [Voi08]. However, almost all μGCs reported to date used external, commercial gas pumps and valves [Gar15, Kim11, Lew06, Zam09]. Some μGCs used microfabricated gas pumps, but only

demonstrated partial system operation; for these, macro-scale injectors were used for vapor injection [Kim07].

Additionally, each of the components in these μGCs was fabricated by separate processes. This greatly constrained the implementation of fully microfabricated μGC systems. Our group has previously demonstrated an approach for fabricating all the fluidic components in a μGC using the same three-mask microfabrication process [Qin14, Qin14]. This approach included the integration of bi-directional gas pumps (*i.e.*, Knudsen pumps) that allowed quantitative analysis without valves. However, these systems used gas detectors based on microdischarge emission spectroscopy. Not only does this require an external optical spectrometer, it also favors the use of an inert carrier gas instead of room air.

Various electronic detectors have been reported for use with μGC systems, including the thermal conductivity detector (TCD) [Kaa10], the discharge photo ionization detector (DPID) [Akb15], the heterodyne graphene detector [Kul14], the surface acoustic wave (SAW) detector [Lew06], the metal oxide semiconductor (MOX) detector [Zam09], the chemiresistor [Kim11], and capacitive detectors [Mls06, Mor14, Pat03]. The TCD, DPID, and heterodyne graphene detector relied upon a supply of Helium as either carrier gas or auxiliary gas, whereas the other detectors were compatible with the use of air as carrier gas. In the context of the stated goals of this effort, the capacitive detectors offer the advantages of (1) commercially available chip-scale electronic interfaces; (2) room temperature operation; (3) compatibility with a variety of simple fabrication processes.

A number of capacitive detectors have been reported in the past. A parallel plate structure reported in [Mls06, Pat03] used a polymer film sandwiched between a perforated top plate and a flat bottom plate. The perforations allowed access of vapor to the polymer. The majority of

capacitive detectors use a simpler structure with on-substrate interdigitated electrodes covered by a polymer film [Hag01, Igr06, Mor14, Zar89]. Upon vapor adsorption, the polymer undergoes both swelling and a change in electrical permittivity. Both effects impact the capacitance. In contrast to the parallel plate structure, there is a greater surface area in the interdigitated structure over which the sampled vapor can interact with the polymer, which generally leads to a faster response. In addition, the thickness of the polymer can be varied in the final step, after lithographic fabrication is completed.

This chapter reports a full μGC system, the *iGC3.c2*, that integrates a Knudsen pump, a preconcentrator, separation columns, and a pair of capacitive detectors. The Knudsen pump operates by thermal transpiration [Knu09], which requires no moving parts and thereby providing high reliability. The preconcentrator uses a cantilever structure that alleviates thermal stress. A series of two separation columns use non-polar stationary phase to separate BTX and other VOCs. The capacitive detectors provide complementary responses based on the dielectric response and swelling. The detector responses are directly measured by commercial integrated circuit chips. All the components are fabricated using a common three-mask process that is further simplified from our prior work [Qin14]. This approach achieves a complete, easily manufacturable μGC that does not rely on external mechanical or optical instruments, or carrier gas suppliy, hence is suitable for long-term, continuous, automated monitoring of indoor pollutants.

The design of the system and various components is described in Section 4.2, the fabrication is described in Section 4.3, the experimental results are presented in Section 4.4, and followed by the discussion and conclusion in Section 4.5.

4.2. Design

The *iGC3.c2* system is divided into two modules: the chromatography module and the Knudsen pump module (Fig. 4.1). The former includes the two-stage preconcentrator, separation columns, and both capacitive detectors, whereas the latter includes only the two-stage, bi-directional Knudsen pump used in this effort. The Knudsen pump requires external heat sinks that are unnecessary for the other components.

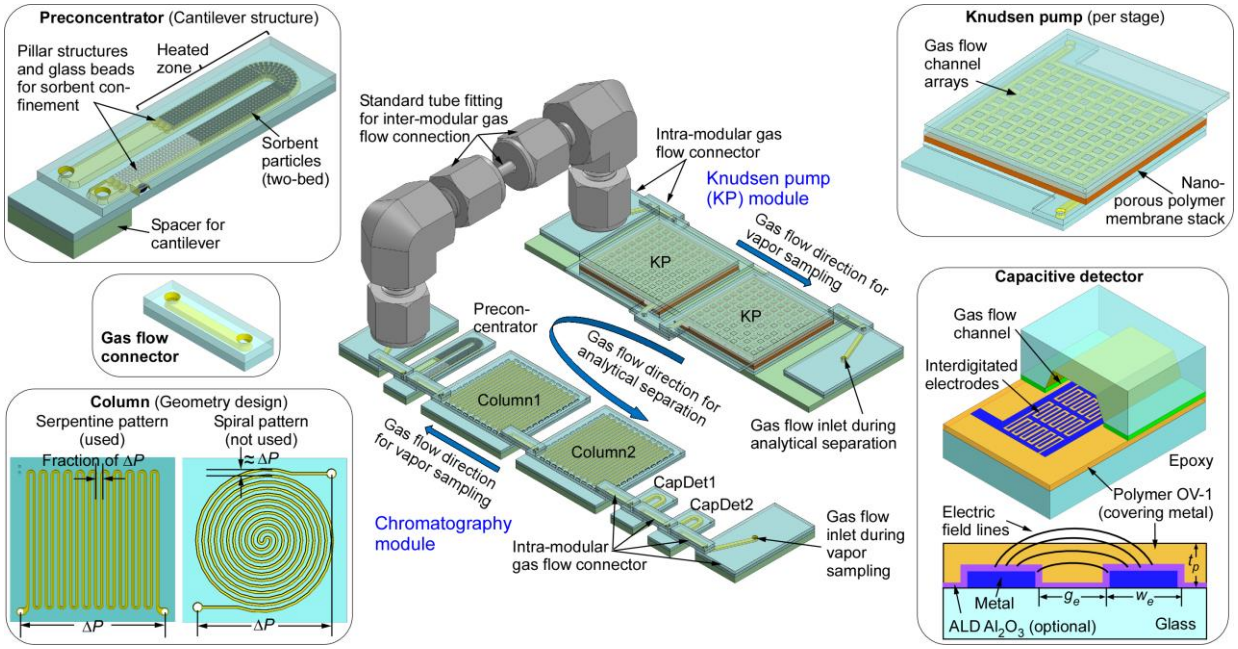

Fig. 4.1: *iGC3.c2* system architecture and component design.

During vapor sampling, the Knudsen pump provides a negative pressure to the chromatography module, drawing the vapor analytes sequentially through the capacitive detectors, the separation columns, and into the preconcentrator. During analytical separation, the Knudsen pump provides a positive pressure, and hence a reversed flow through the chromatography module. The preconcentrator provides thermal injection of the analytes, which are separated by the columns and detected by the capacitive detectors. The columns can be selectively heated to accelerate the separation. Heating of the Knudsen pump, preconcentrator, and separation columns is provided

by the embedded thin-film metal heaters, whereas the temperatures of these components are monitored using the embedded thin-film metal thermistors.

In the preconcentrator, the sorbent particles, which absorb the VOCs, are held in a channel with an elongated "U" shape, of width ≈1350 μm and height ≈300 μm (Fig. 4.1). The sorbent particles are confined to the lower half of the "U" shape by pillar-like structures and glass beads that are packed against the pillars. A thin-film metal heater is located in this region to provide localized heating for vapor desorption. The gas flow inlet and outlet are located at the upper end of the "U" shape, which is cantilevered above a glass spacer, thermally isolating it from the substrate. This design relieves thermal stress and reduces heat loss. Two segments of sorbents, Carbopack-B and Carbopack-X (Sigma Aldrich, WI) are packed in series into the "U"-channel to target a wide range of vapor species. Other types of sorbents can also be used, depending on the specific applications.

The separation columns are serpentine channels with hydraulic diameter ≈230 μm and length ≈30 cm per chip. The interior of these channels is coated with ≈0.2 μm thick OV-1 stationary phase (*i.e.*, 100% polydimethylsiloxane or PDMS, Ohio Valley Specialty, OH). In this work, two identical column chips are used, providing a total length of ≈60 cm. The microfabricated columns can be implemented in mainly two shapes: the serpentine pattern and the spiral pattern. Whereas it has been reported that the serpentine pattern provides slightly higher performance than the spiral pattern [Rad10], for this work its primary attraction lies in more uniform pressure distribution and better immunity to leakage than the spiral pattern (Fig. 4.1). With a given pressure (ΔP) applied between the two ends of a serpentine column, the pressure is evenly distributed from one end of the chip to the other end. Therefore, the maximum pressure between any two adjacent channels is only a fraction of ΔP. In the spiral column, however, the pressure between two adjacent channels

varies from zero in the chip center to ≈Δ*P* near the chip perimeter. Therefore, any potential leak site near the chip perimeter could directly shunt the column (*i.e.*, cause gas flow to pass through the leak site but not the rest of the column), greatly compromising the performance.

The capacitive detectors are formed using closely spaced interdigitated electrodes (Fig. 4.1). The electrodes are covered by a layer of OV-1, which is also used as the stationary phase in the separation columns. This polymer, upon exposure to VOCs, undergoes changes in thickness and permittivity. In principle, detector performance can be improved by downscaling of various feature dimensions. As the detector output signal is capacitance change (Δ*C*), a smaller interelectrode gap provides higher Δ*C*. A smaller electrode width permits denser integration of electrodes, which also provides higher Δ*C* per unit area. In addition, a thinner polymer layer provides faster response, as the detector response time is mainly constrained by the speed of vapor absorption and desorption in the polymer layer. In this work, the interdigitated electrodes have widths and gaps of ≈1 μm, which is limited by the lithographic equipment available for this project. Two detectors with different polymer thicknesses are connected in series along the fluidic path, downstream of the separation column. The first detector, CapDet1, uses an OV-1 layer of thickness ≈0.25 μm. Because this is substantially smaller than the interelectrode gap, the electric field lines extend over the polymer. Its capacitance change, Δ*C1*, is always positive, dominated by the swelling response of the OV-1. The second detector, CapDet2, uses an OV-1 layer of thickness ≈1.6 μm. Its capacitance change, Δ*C2*, can be either positive or negative, depending on the dielectric constant of the vapor species relative to that of the OV-1. Whereas the swelling response of the OV-1 does not contribute to Δ*C2*, the change in permittivity caused by the penetration of the gas molecules matters more because the electric field lines are mostly contained

within the polymer [Igr06]. In each detector, the electrodes occupy a footprint of ≈1 mm^2, which is enclosed in a gas flow channel with width ≈800 μm and height ≈300 μm.

Knudsen pumps generate gas flow by thermal transpiration in narrow channels with hydraulic diameter comparable to or less than the molecular mean free path [Knu09]. The gas molecules tend to move against the temperature gradient along the channel. In this work, each stage of the Knudsen pump uses a stack of nanoporous mixed-cellulose-ester (MCE) membranes to provide thermal transpiration [Gup11]. Each membrane has average pore diameter ≈25 nm and porosity ≈70% (Millipore, MA); the stack has a total thickness of ≈500 μm, and footprint ≈16×16 mm^2. The membrane stack is sandwiched between glass dice from above and below, both with embedded thin-film metal heaters, thermistors, and flow channels (Fig. 4.1). External heat sinks are attached to the glass dice. By selectively heating one side of the membrane stack, flow can be generated in either direction. This permits the flow direction to be reversed when switching from sampling to separations. Two pumping stages are used to increase the output pressure head for the separation columns.

All components are arranged in a planar fashion, in both the chromatography module and the Knudsen pump module. Within each module, the components are connected by co-fabricated gas flow connectors. The small length of these connectors (7 mm) permits compact arrangement of the components, minimizing the overall footprint. The modules can be readily reconfigured with more separation columns and more Knudsen pump stages. The two modules are connected by compression tube fittings (Fig. 4.1), which facilitate modular reconfiguration.

4.3. Fabrication

We have previously reported a three-mask process for various μGC components [Qin14]. In that process, a glass wafer was first metallized, and subsequently micromachined. In the current effort, the metallization and micromachining are performed on different glass substrates that are later bonded together. Consequently, the micromachining and metallization are not performed sequentially (Fig. 4.2). Whereas the new approach cannot be used for the stacked architectures [Qin14, Qin14] that require through holes to provide vertical gas flow paths, it becomes feasible for the planar arrangement of components described in this work. The basic elements of each of the system components are fabricated from glass wafers by a common three mask process. One mask is used to pattern a thin film of Ti/Pt (25/100 nm) for the heaters thermistors, and capacitor electrodes. The other two masks serve to define trenches and perforations for the fluidic path by sandblasting both sides of the wafer.

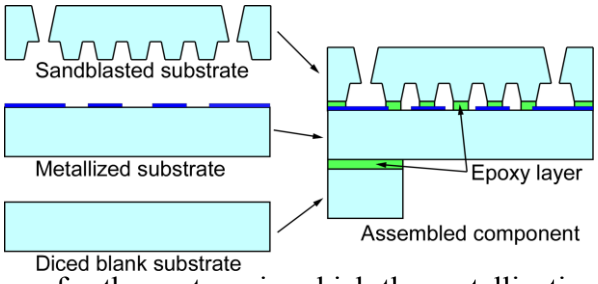

Fig. 4.2: Fabrication process for the system, in which the metallization and micromachining are performed on separate glass substrates in parallel.

The Knudsen pump is assembled by sandwiching the MCE membrane stack with the microfabricated glass dice and sealed with an epoxy (Stycast2850FT, Henkel, Germany). The MCE membrane and the epoxy could induced mild outgas issues that interfere with the chromatography; these issues can be addressed by proper system operation as discussed in the experimental section. The preconcentrator is assembled by bonding the glass dice with another epoxy (Epotek-377, Epoxy Technology Inc., MA). The two types of sorbent particles, *i.e.*,

Carbopack-X and Carbopack-B, as well as the glass beads, are sequentially packed, by a gentle vacuum, into the "U"-channel from a loading port that is subsequently sealed by the Stycast2850FT epoxy. The separation column is assembled by bonding the glass dice with a spin-coated layer of adhesion material (SU-8, MicroChem, MA), followed by the application of OV-1 stationary phase coating to the interior of the column using the established static coating method [Rei06].

For the capacitive detectors, the metallized substrate is coated with 10 nm-thick Al_2O_3 using atomic layer deposition. This is an optional, precautionary step to prevent potential shorting caused by dust, *i.e.*, it can be excluded if the assembly is performed in a clean environment. Next, an OV-1 solution is spin-coated on the metallized substrate. The OV-1 solution is prepared by dissolving OV-1 in nonane. A small quantity of dicumyl peroxide (<10% of OV-1 in weight) is also added to the solution to provide cross-linking [Rei06]. Other common non-polar solvents such as pentane and hexane have also been evaluated for preparing the solution. However, these solvents easily cause random cavities in the spin-coated OV-1 layer, possibly because these solvents have high volatility and form bubbles during spin-coating. In contrast, the less volatile nonane provides a smooth and uniform OV-1 film after spin-coating. Subsequently, the OV-1 coated substrate is bonded to the sandblasted substrate with epoxy adhesion.

The components in the chromatography module are mounted on a printed circuit board (PCB), whereas the Knudsen pumps are mounted on a PCB platform that is attached to heat sinks. The gas flow connectors which were co-fabricated are attached with the other fluidic components. Electrical lead transfer between the components and PCBs is provided by commercial pins and headers directly soldered to the components. To prevent on-board electromagnetic crosstalk that can affect the detector readout, CapDet1 is fenced in by an aluminum perimeter that is grounded.

The photograph of the system is shown in Fig. 4.3. The overall footprint of the system, including both modules, is ≈8×10 cm^2.

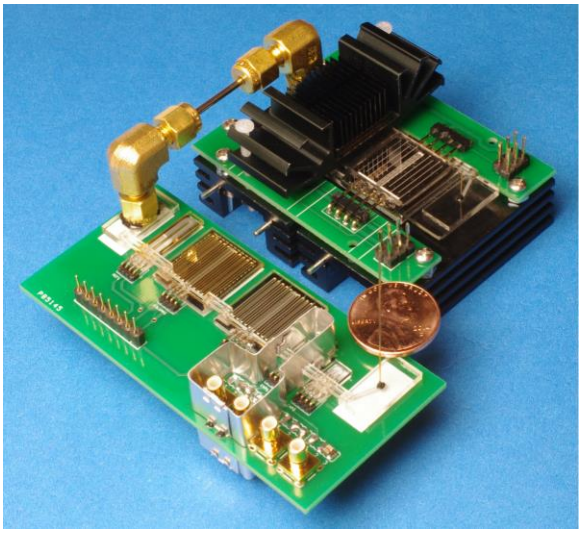

Fig. 4.3: Photographs of the *iGC3.c2* system. One of the Knudsen pump heat sinks is removed to reveal the inner structure.

4.4. Experimental Results

Test vapor preparation. To evaluate its performance, the *iGC3.c2* system was used to sample, separate, and detect mixtures of 19 chemicals. The chemical species were labeled in groups based on their molecular structures or properties. The *a*-group includes 6 non-polar *n*-alkanes in the range of pentane (C_5) to decane (C_{10}); the *b*-group includes 5 non-polar aromatic hydrocarbons: benzene, toluene, *m*-xylene, *o*-xylene, and mesitylene; the *c*-group includes 5 mildly-polar chemicals (aldehyde and halogenated hydrocarbons): hexanal, chlorobenzene, chlorohexane, 4-chlorotoluene, and 1,3-dichlorobenzene; the *d*-group includes 3 other non-polar chemicals (cycloalkane and terpenes): cycloheptane, α-pinene, 3-carene. Most of these chemicals are common indoor air pollutants [Kos95].

To prepare the test vapor, the 19 chemicals in liquid form were first formulated into a mixture. The volume of each chemical was adjusted (based on density and molar mass) such that each non-

polar chemical had equal concentration in the resulting vapor, and each mildly-polar chemical had 1/5 of that concentration. For analyses that were performed on relatively concentrated mixtures (where each non-polar chemical had 0.5-1 ppm), liquid mixtures of 85-170 nL were injected into a 2 L dilution bottle prefilled with room air. For analyses at lower concentrations, the injected liquid volume became difficult to be controlled accurately. Therefore, the liquid mixtures were diluted with pentane before being injected into the 2 L bottle. In each case the mixture injected into the bottle was evaporated to form the test vapor. Table 4.1 summarizes the vapor concentrations that were tested. In this chapter, the units for vapor concentration, *i.e.,* "ppm" and "ppb", are defined as the number of molecules of each chemical divided by the number of molecules of air in the prepared vapor and multiplied by 10^6 and 10^9, respectively.

Experimental control. During vapor sampling, the bottle was connected to the port upstream of the capacitive detectors (Fig. 4.4). The Knudsen pump module provided 0.2 sccm flow for 10-120 min., drawing the vapor through the detectors, the separation columns, and into the preconcentrator. The temperature in the pump was controlled by the on-chip heaters and temperature sensors operated by a customized closed-loop control algorithm in LabVIEW. The pump consumed ≈4 W power during vapor sampling. A commercial flow meter (Model # MW-20SCCM-D, Alicat Scientific, Inc., AZ) was optionally connected downstream of the pump to provide readings of the flow rate. The other end of the flow meter was open to room air. The control of the system did not rely on the flow meter. The chromatography module was maintained at room temperature. After vapor sampling, the Knudsen pump was turned off and allowed to cool down for 15-20 min before initiating analytical separation.

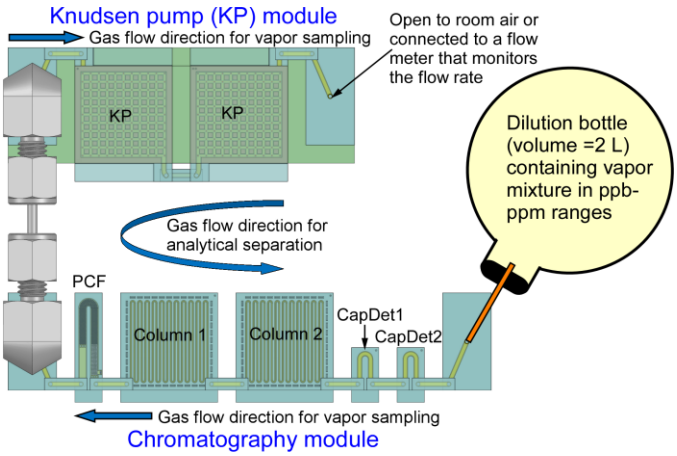

Fig. 4.4: The test setup for the system performing vapor sampling.

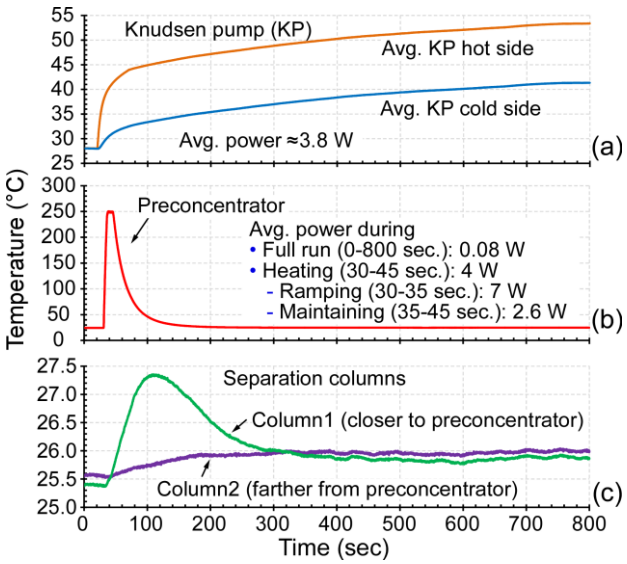

Fig. 4.5: Typical temperature control of the system during analytical separations without active temperature programming of the separation columns. (a) The Knudsen pump using a continuous temperature gradient to provide flow. (b) The preconcentrator using a thermal pulse to perform vapor injection. (c) The separation columns enduring temperature rise only due to thermal crosstalk with the preconcentrator.

During analytical separation, the dilution bottle was removed. The time when the software for control and readout was initiated was defined as time =0. Starting at time ≈20 s, the pump provided a reversed 0.2 sccm flow with ≈4 W power, pushing room air through the chromatography module to serve as the carrier gas. After the flow rate reached appropriate levels, starting at time ≈30 s, the preconcentrator was heated to 250ºC in 5 s, then maintained at 250ºC for 10 s (Fig. 4.5) to

thermally inject the sampled vapors into the closest separation column (Column1). As for the Knudsen pumps, the preconcentrator was heated using the embedded thin-film metal heaters, and its temperature was monitored using embedded thermistors. For most experiments, the columns were not actively heated. Column1 endured a temporary temperature rise of 2 ºC due to crosstalk from the thermal pulse delivered to the preconcentrator, whereas Column2 showed modest (0.5 ºC) temperature rise (Fig. 4.5).

During either sampling or separation, the 0.2 sccm air flow through the system resulted from the overall pressure load of fluidic path presented to the Knudsen pump module (Fig. 4.6). The flow properties of both modules were measured in separate experiments. The flow resistance of the chromatography module was measured by using an external vacuum pump to create an air flow through the module, while the flow rate and pressure difference along the module were measured by a flow meter (MW-20SCCM-D, Alicat Scientific, Inc., AZ) and pressure sensor (MPX5010DP, Freescale Semiconductor Inc., TX), respectively. The flow resistance of the Knudsen pump module was measured in the same manner. The output pressure head and flow rate characteristics of the Knudsen pump module were measured by supplying the pump with 4 W power and varying the flow resistance connected to the pump. The pump provided a maximum flow rate of 0.5 sccm and a blocking pressure of 1 kPa. The intercept of the pump characteristic line and the chromatography module resistance line appeared at 0.2 sccm, as was experimentally confirmed by the flow meter.

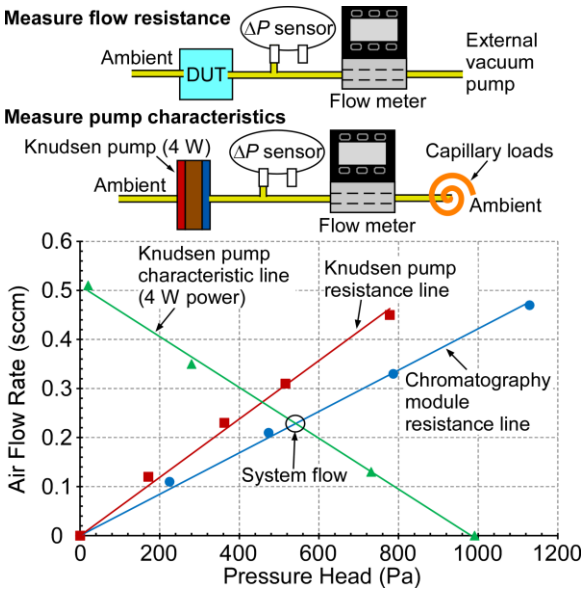

Fig. 4.6: Pump characteristics and flow resistance of the Knudsen pump module and chromatography module.

The two capacitive detectors were simultaneously measured by two commercial capacitive-to-digital converter (CDC) chips (AD7746, Analog Devices, MA). Each CDC provided a square-wave excitation signal to one set of electrodes in the capacitive detector, and measured the voltage from the opposite set of electrodes. Because the excitation signal for one detector could affect the voltage readout from the other detector through electromagnetic coupling, an electromagnetic shield, made of custom-cut aluminum sheets and connected to the CDC ground, were placed on the PCB, as noted in Section 4.3. The CDCs used a detection rate of ≈7 Hz. When the CDC was not connected to any capacitor, its rated and measured value of the root-mean-square (RMS) noise was ≈4 aF. When it was connected to the capacitive detector in the current setup, the measured RMS noise was ≈40 aF. The noise increase could potentially be reduced with improved PCB design.

A number of experiments were performed on test samples, as explained in the remainder of this section. Before each analytical cycle, the preconcentrator was flushed for ≈30 s by providing another thermal pulse as that used for the vapor injection, while the pump provides 0.2 sccm flow.

This prevents contaminant from accumulating in the preconcentrator from run to run, essentially regenerating the system.

Data processing. Typical raw chromatograms obtained from the capacitive detectors showed retention peaks superposed upon drifting baselines (Fig. 4.7), which might be caused by gas flow induced redistribution of chemicals in the system. The baseline drift was digitally compensated by a customized MATLAB program to facilitate user perception of the chromatogram. First, baseline segments were identified in the chromatogram; this was performed manually in the present work, but in principle can be performed automatically by software [Tze15]. Next, a polynomial of degree 10-20 was used to fit the baseline segments. Finally, the raw chromatogram was subtracted by the polynomial, providing the compensated chromatogram (Fig. 4.7).

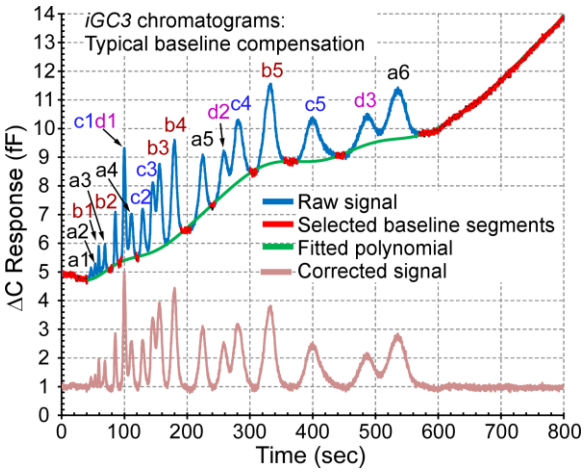

Fig. 4.7: Digital baseline compensation of a typical chromatogram provided by the capacitive detector.

Quantitative analysis. To demonstrate quantitative analysis, the system was used to detect the 19-chemical mixture with various concentrations (Table 4.1). The chromatograms from CapDet1 and CapDet2 are shown in Fig. 4.8 and Fig. 4.9, respectively. A sampling time of 30 min. was sufficient to demonstrate the effective separation and detection of chemicals with concentration range of 0.05-1 ppm for non-polar species and 0.01-0.2 ppm for mildly-polar species (*e.g.*, in Run

1-4, Fig. 4.8a and Fig. 4.9a). For lower concentrations (*i.e.*, 10 ppb for non-polar species and 2 ppb for mildly-polar species), the 30 min. sample did not provide distinguishable peaks (*e.g.*, in Run 5a). However, a sampling time of 2 hours did provide distinguishable peaks (*e.g.*, in Run 5b, Fig. 4.8b and Fig. 4.9b).

Table 4.1: List of chemicals and test conditions

Run ID:			1							2	3	4	5	
			1a	1b	1c	1d	1e	1f	1g				5a	5b
Column temperature during separation			Room temperature					Programmed		Room temperature				
Sampling time (min.)			30	20	15	10	30	30	30	30	30	30	30	120
Relative humidity			10-20%				50%	10-20%						
Chemicals		**Polarity**	**Concentration (ppm)**											
a1	pentane C5	nonpolar	1							0.5	20	10	10	
a2-a6	n-alkanes C6-C9	nonpolar	1							0.5	0.1	0.05	0.01	
b1-b5	benzene, toluene, m-xylene, o-xylene, mesitylene	nonpolar	1							0.5	0.1	0.05	0.01	
c1-c5	hexanal, chlorobenzene, chlorohexane, 4-chlorotoluene, 1,3-dichlorobenzene	mildly polar	0.2							0.1	0.02	0.01	0.002	
d1-d3	cycloheptane, α-pinene, 3-carene	nonpolar	1							0.5	0.1	0.05	0.01	

Low concentration analysis. The results for relatively low concentration analyses (Run 3-4) can be elucidated by applying a progressive moving average method to the chromatograms (Fig. 4.8b and Fig. 4.9b). Moving averages are typically used to process transient data streams: a fixed-length window moves along the stream, and raw data within the window are averaged to generate a new data point. The window length is required to be large enough to minimize the noise in the data, but also small enough to preserve the signal intensity. In the case of GC chromatograms, later retention peaks are typically wider than earlier ones because of the longitudinal diffusion in the separation columns [Bar04]. Therefore, the GC chromatograms are more amenable to be processed by moving average with a varying window length. In Fig. 4.8b and Fig. 4.9b, the window length for the chromatograms was linearly ramped from 5 points (before time ≈30 s) to 101 points (at the end of the chromatograms). This method evidently reduces the noise without significantly distorting the retention peaks.

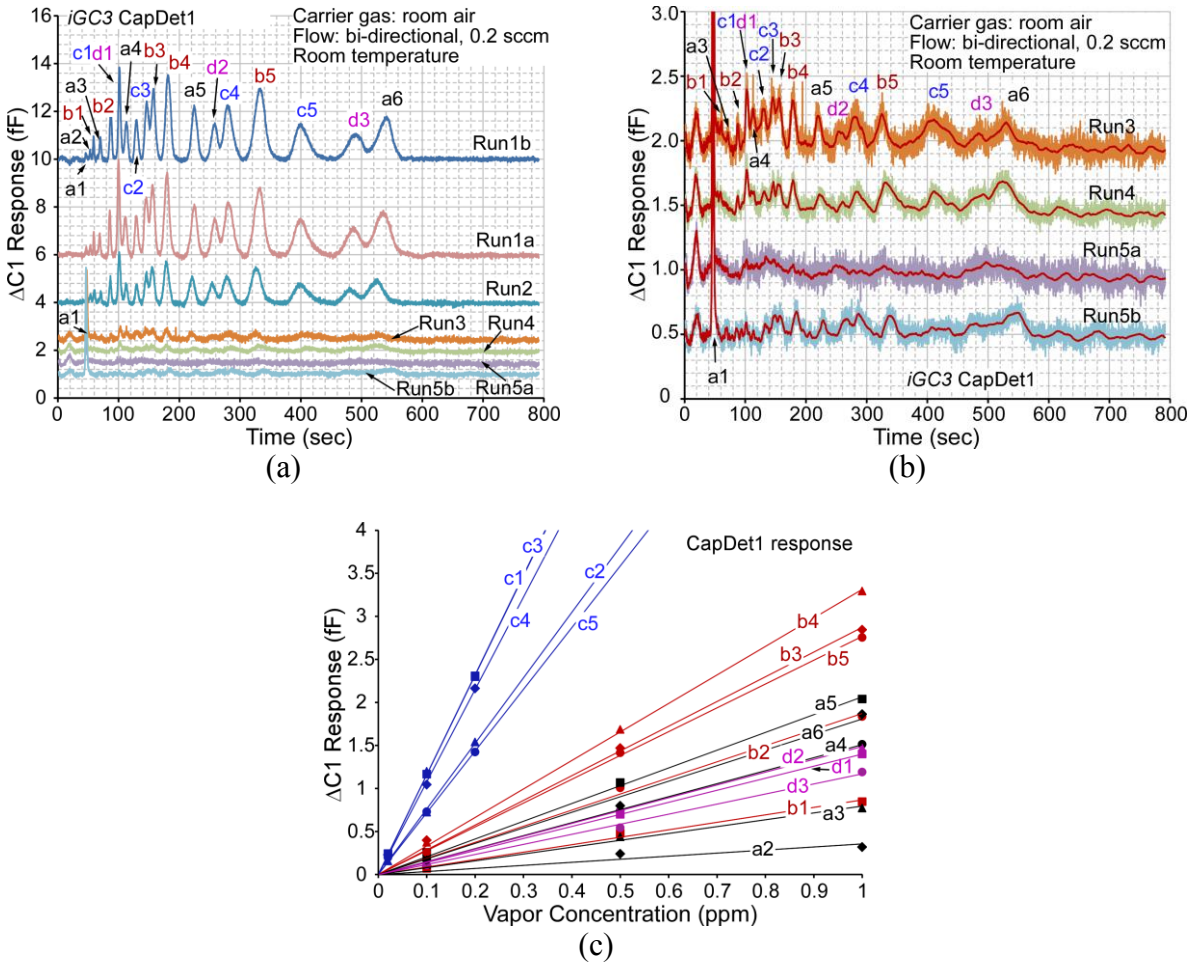

Fig. 4.8: *iGC3.c2* system results for 19 chemical with varying concentrations provided by CapDet1. Separation was performed by room temperature. (a) Original chromatograms. (b) Magnified chromatograms of the low concentration runs. (c) Measured peak heights ($\Delta C1$) showing proportionality to prepared vapor concentrations.

Linearity and sensitivity trends. The peak heights extracted from the chromatograms varied proportionally with the corresponding vapor concentrations being sampled (Fig. 4.8c and Fig. 4.9c). This proportionality is provided by the capacitive detectors. Compared to some other detectors that provide linear response in log or log-log scales [Kul14, Zam09], the directly proportional response of the capacitive detectors significantly reduces the effort of characterization and calibration before the system can be used for quantitative analyses. Further, as indicated by slopes in Fig. 4.8c and Fig. 4.9c, both CapDet1 and CapDet2 showed higher sensitivity to the *c*-

group (mildly-polar) chemicals than to the *a*-, *b*-, and *d*-group (non-polar) chemicals. Compared to CapDet1, which showed positive peaks to all the tested chemicals, the CapDet2 showed positive peaks to the c-group, negative peaks to the a- and d-group, and nearly zero response to the b-group. Additionally, both detector responses showed a certain trend of sensitivity to alkanes: the absolute value of sensitivity increased from pentane (*a1*) to nonane (*a5*), but started to decrease from nonane to decane (*a6*). These observations are discussed in the next section.

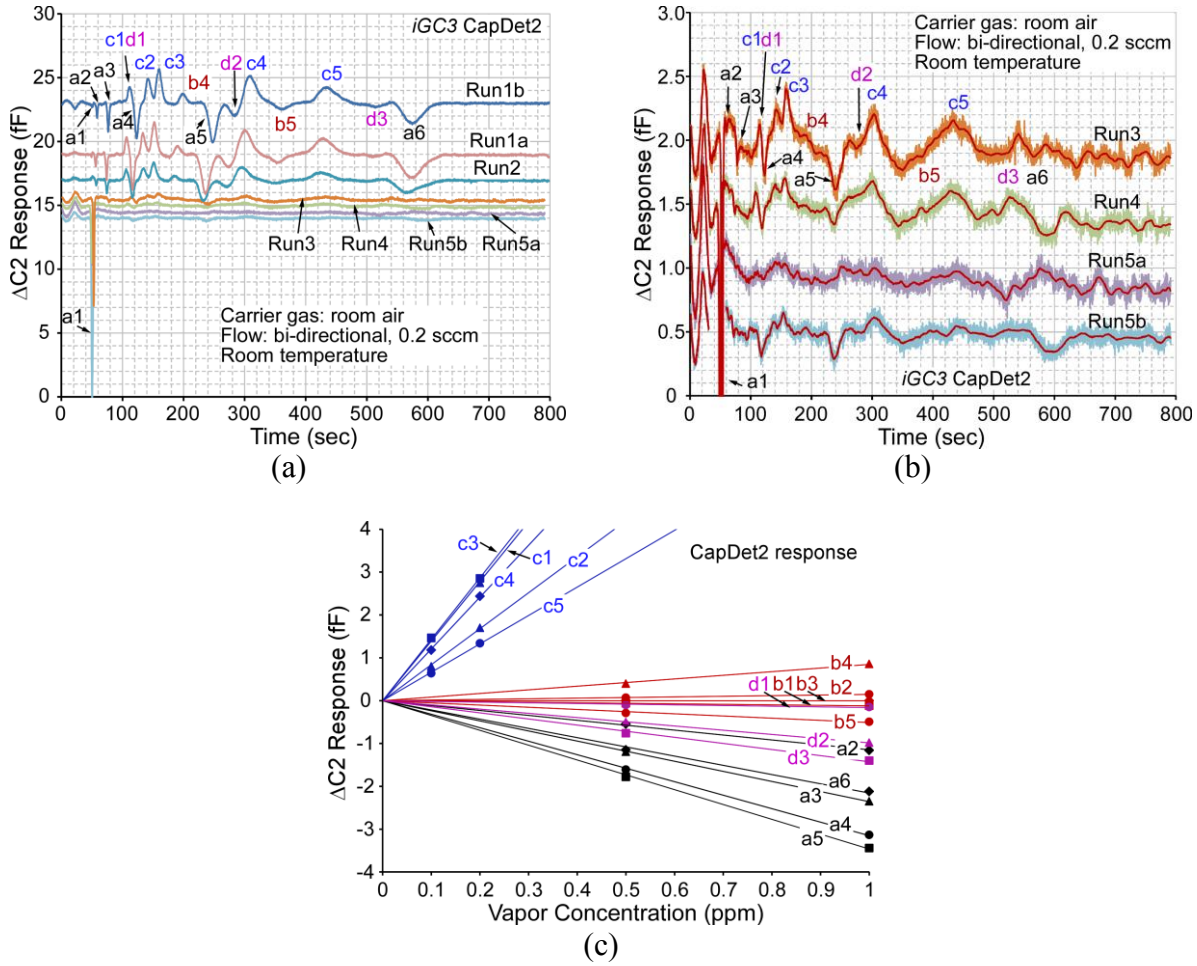

Fig. 4.9: *iGC3.c2* system results for 19 chemical with varying concentrations provided by CapDet2. Separation was performed by room temperature. (a) Original chromatograms. (b) Magnified chromatograms of the low concentration runs. (c) Measured peak heights (Δ*C*2) showing proportionality to prepared vapor concentrations.

Effect of humidity. The relative humidity in the lab where the tests were conducted varied between 10-20%, as measured by a commercial humidity sensor (#42280, Extech Instruments Corporation, NH). To test the system response to moisture, an additional amount of water was injected to the 2 L dilution bottle together with the other 19 chemicals, providing ≈50% relative humidity in the sampled vapor, which is equivalent to a concentration of ≈12,000 ppm. The increased moisture caused baseline variations that were different from those obtained with room humidity. However, after baseline compensation, the system response to the moisturized vapor (Run 1b) was similar to that for the non-moisturized vapor (Run 1a, Fig. 4.8b and Fig. 4.9b).

Resolving coeluting peaks. In some examples of μGC systems, arrays of detectors, each having a unique response pattern to various chemicals, have been used to enhance the discrimination of eluted peaks [Bry14, Kim11, Mls06]. In contrast to the reported chemiresistor arrays [Bry14], which provided only positive peaks to almost all chemicals, capacitive detectors can provide both positive and negative peaks [Igr06, Mor14], thereby providing higher discrimination capabilities for certain chemical species. In this work, particularly, the a- and d-group chemicals can be easily differentiated from the *c*-group chemicals by the use of CapDet1 and CapDet2. Additionally, these two detectors can be used to resolve co-eluting peaks. In this process, the detector response ratio, *i.e.*, $r = \Delta C2/\Delta C1$, was first determined for each chemical (Fig. 4.10a). This can be done by training the system with subsets of the chemicals, which produce no co-eluting peaks. Next, in the two detector responses ($\Delta C1$ and $\Delta C2$) where two peaks (*e.g.*, peak *A* and peak *B*) co-elute, an equation matrix can be listed:

$$\begin{cases} \Delta C1_A + \Delta C1_B = \Delta C1 \\ r_A \cdot \Delta C1_A + r_B \cdot \Delta C1_B = \Delta C2 \end{cases} \tag{4.1}$$

where $\Delta C1_A$ and $\Delta C1_B$ are the two co-eluting peak signals in CapDet1 response, and r_A and r_B are the detector response ratio for peak *A* and peak *B*, respectively. After solving this equation matrix

for every data point in the chromatogram segments containing the two co-eluting peaks, each co-eluting peak can be separately reconstructed. As shown in Fig. 4.10b and c, this method successfully resolves partially co-eluting peaks *c3-b3* and *d2-c4*, as well as fully co-eluting peaks *c1-d1*.

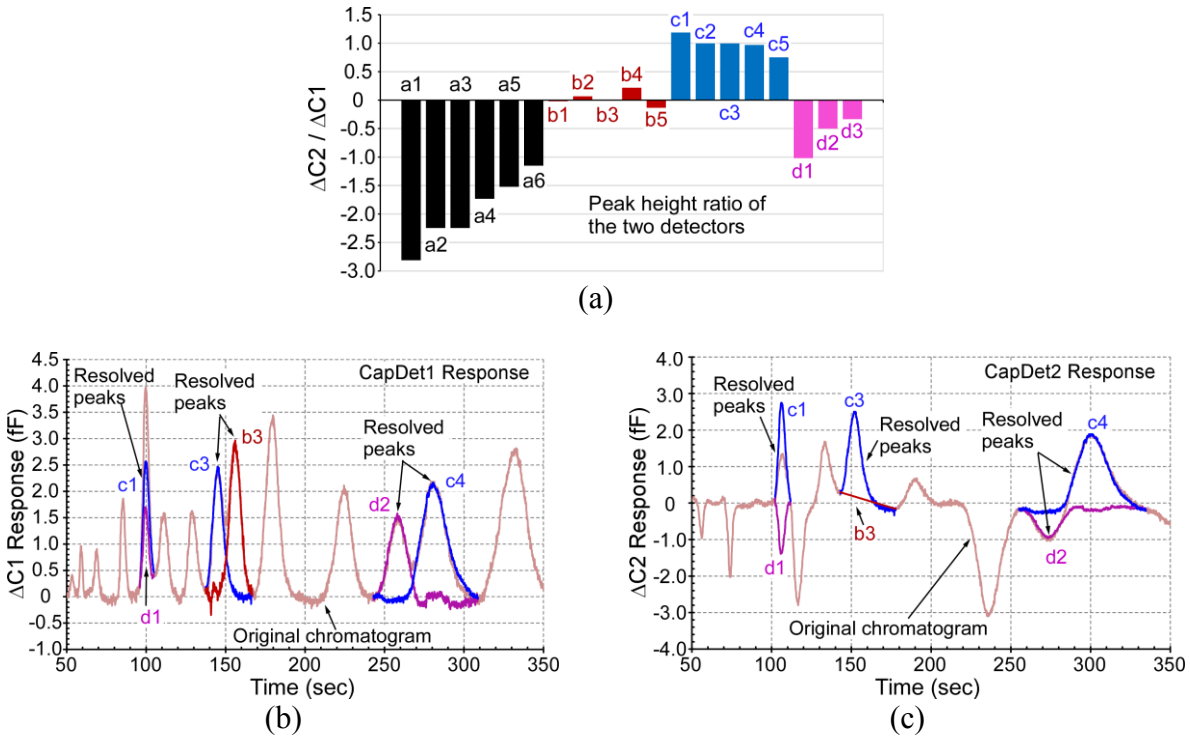

Fig. 4.10: Co-eluting peaks resolved by the two capacitive detector responses. (a) Capacitive detector response ratios ($\Delta C2/\Delta C1$) for various chemicals. (b) Co-eluting peaks resolved in CapDet1 chromatogram. (c) Co-eluting peaks resolved in CapDet2 chromatogram.

Characterization of sampling. In the *iGC3.c2* system, the sampled vapor must pass through the detectors and columns before reaching the preconcentrator. In order to assess the impact of this, the system was used to analyze the same vapor concentration – 1 ppm of non-polar chemicals and 0.2 ppm for mildly-polar chemicals – repeatedly, with different sampling times ranging from 10-30 min. The peak height provided by the detectors varied linearly, but not proportionally, with the sampling time (Fig. 4.11). The intercept of the linear function on the axis of sampling time indicates the threshold time, *i.e.*, the time taken by a vapor species to pass through the detectors

and columns. The threshold time of the vapor was close to its retention time during analytical separation, provided that the sampling and separation used the same magnitude of flow rate.

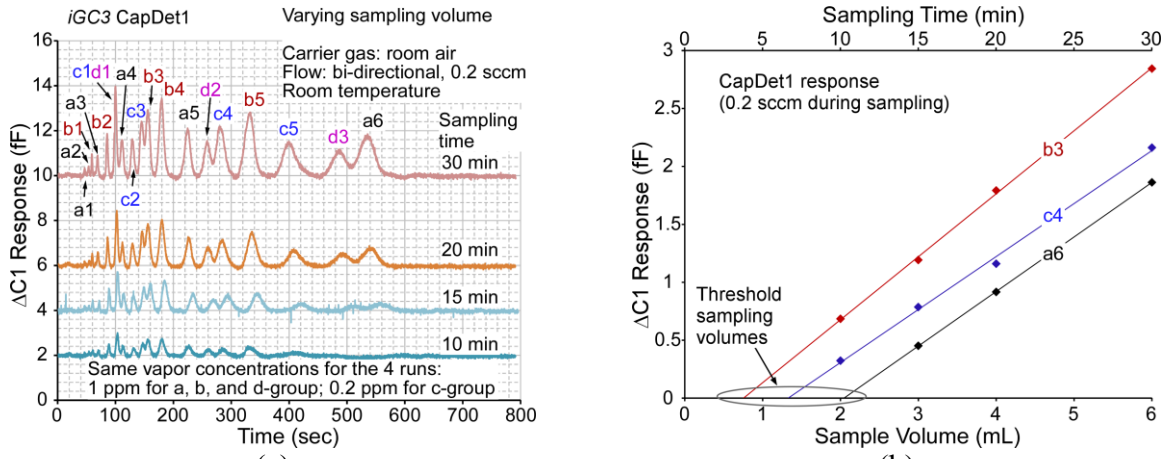

Fig. 4.11: Characterization of the *iGC3.c2* sampling operation. (a) Chromatograms of the same vapor with various sampling volumes. (b) Calculation of the peak heights. The intercepts on the horizontal axis indicate the threshold volumes (*i.e.*, the volumes taken by the vapors to pass through the column during sampling).

Temperature programming. Temperature programming of the separation columns was also demonstrated to accelerate the separation (Fig. 4.12). For microfabricated separation columns, each column chip can often be individually programmed [Kim11]. In Run 1f (Fig. 4.12a), the temperature of Column1, which was upstream of Column2 during separation, was ramped up linearly from room temperature to 40°C from t =100 s to t =200 s and then allowed to cool naturally. Further heating of Column1 was unnecessary, as all the tested chemicals had eluted Column1. The temperature of Column2 was linearly ramped to 52°C during from t =100 s to t =320 s and then allowed to cool naturally. Compared to room temperature separation, this temperature programming run accelerated the separation by ≈50%, and increased the peak heights of certain chemicals by 50-100%. The columns consumed a total average power of 0.5 W for the duration from t =100 s to t =320 s. The power consumption can be slightly reduced by heating only the downstream column. In Run 1f (Fig. 4.12b), the temperature of Column2 was linearly ramped to

50°C during 200-400 s, whereas Column1 was not actively heated. Compared to room temperature separation, this temperature programming run accelerated the separation by ≈30% while the columns consumed only 0.4 W.

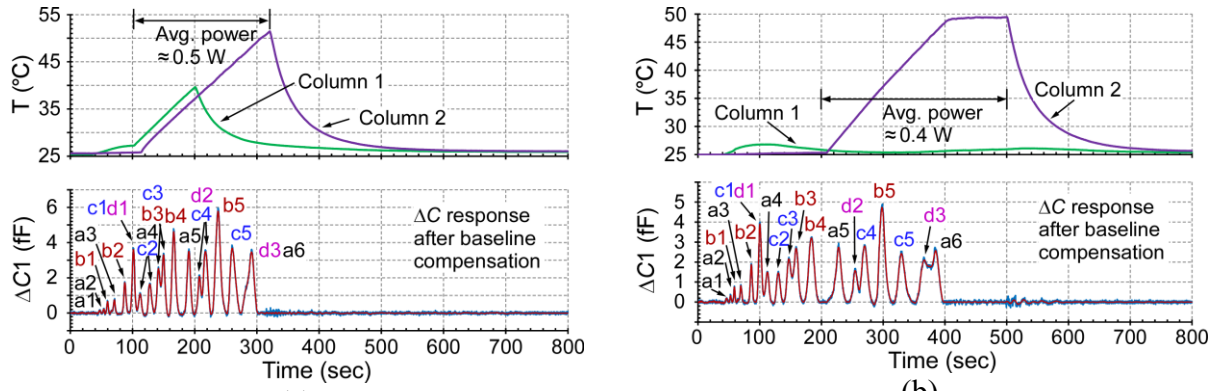

(a) (b)

Fig. 4.12: Accelerated separation provided by temperature programming of the separation columns. (a) Heating both columns for fast separation. (b) Heating only Column 2 to accelerate separation with lower power consumption.

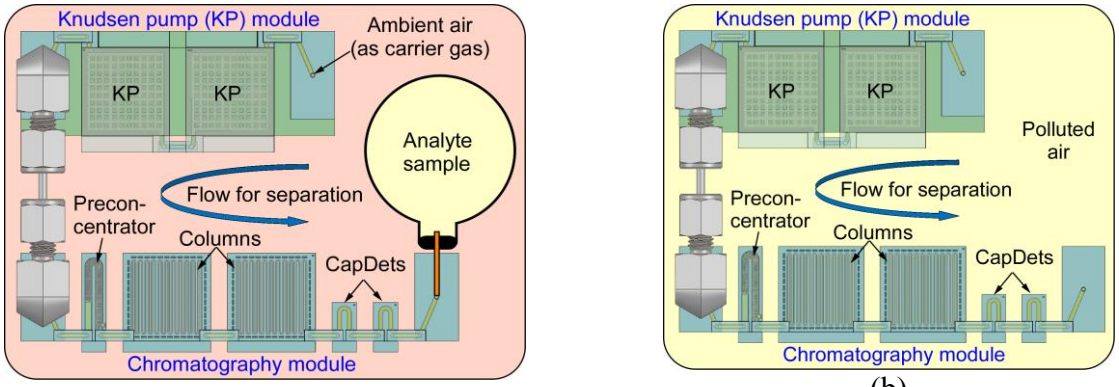

(a) (b)

Fig. 4.13: Two scenarios of the system operation. (a) A conventional scenario where vapor samples are collected and fed to the system; the carrier gas is room air that does not contain the analytes. (b) A different scenario where the system automatically monitors the ambient pollutants; the carrier gas contains the analytes.

The aforementioned experiments used the ambient air as the carrier gas, which was relatively clean and not contaminated by the analyte samples. These results demonstrated the system operation in a conventional test scenario (Fig. 4.13a), where vapor samples are manually collected and fed to the system for analyses. However, if the system is operated in a different scenario where

the ambient pollutants are being monitored automatically, the carrier gas used for analytical separation would be polluted by the same vapor being sampled (Fig. 4.13b).

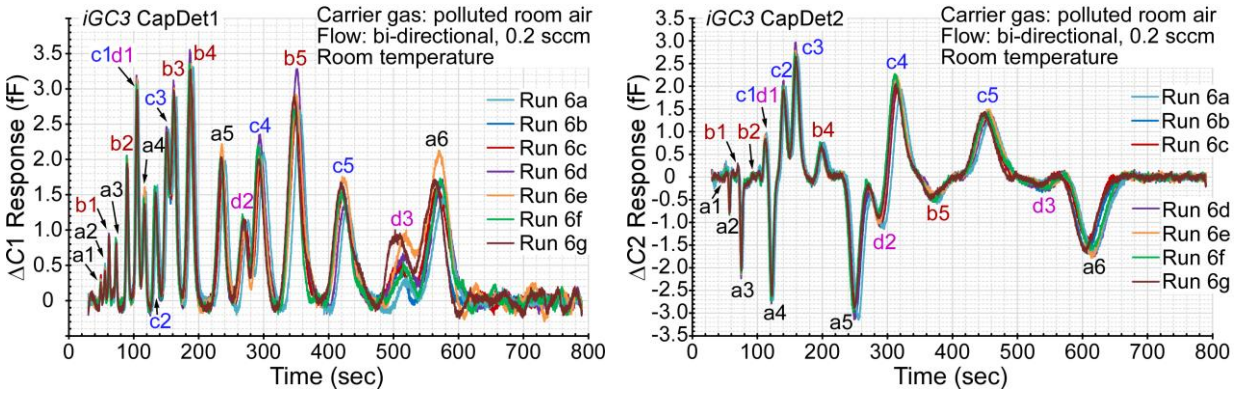

(a) (b)

Fig. 4.14: Chromatograms of repeated runs using both ambient and polluted air as the carrier gas. Run 6a used the (relatively clean) ambient air as the carrier gas. Run 6b-c used polluted air with 10-25% ambient relative humidity as the carrier gas for benchmarking. Run 6d-g used polluted air with 50% relative humidity as carrier gas. (a) CapDet1 response. (b) CapDet2 response.

To mimic this latter scenario, another set of experiments was performed, in which the dilution bottle filled with the tested vapor mixture (Fig. 4.4) was connected upstream of the Knudsen pump during analytical separation to provide the carrier gas. In principle, the preconcentrator, after thermal desorption, traps the VOCs in the carrier gas, preventing the VOCs from entering the separation columns. Therefore, in a single run, the results with the use of polluted air as the carrier gas should be similar to that using ambient air. In consecutive runs, however, the VOCs trapped by the preconcentrator during previous analytical separation could be injected, together with the new sample, into the separation column in the following run, causing hysteresis and overestimation of the VOC concentrations. Therefore, before each vapor sampling cycle, the preconcentrator was flushed by a flow in the direction of sampling for a short duration. In experimental evaluation, the system was tested with consecutive runs. As shown by the experimental results in Fig. 4.14, the chromatograms for the 19 chemicals (1 ppm in *a*-, *b*-, and *d*-group, 0.2 ppm in *c*-group) in the carrier gas (Run 6b-c) overlap with that using the relatively clean ambient air as the carrier gas

(Run 6a). Additionally, these chromatograms also overlap with those for the same 19 chemicals and 50% relative humidity in the carrier gas (Run 6d-g). These results indicate that the system can perform repeatable analyses in a polluted environment.

4.5. Discussion and Conclusion

The results of the two capacitive detectors warrant discussion. As noted previously, the ΔC depends on changes in both thickness and permittivity that are caused by the eluted peaks of the VOCs to the OV-1 polymer film covering the electrodes. The permittivity response can be expressed as the difference in dielectric constants of polymer and chemical, *i.e.*, $\varepsilon_{ch} - \varepsilon_p$, in the affected region of OV-1. If this term is positive, the average dielectric constant of the polymer-chemical matrix is higher than that of the polymer, and the resulting ΔC will also be positive. Conversely, if this term is negative, its contribution to the ΔC will be negative.

In CapDet2, where the polymer thickness of 1.6 μm is greater than the electrode width and gap of 1 μm, polymer swelling does not affect ΔC, as most electric field lines for sensing are distributed only in the lower portion of the polymer. Hence, $\Delta C2$ depends almost entirely on $\varepsilon_{ch} - \varepsilon_p$. The dielectric constant of OV-1 (ε_p), which is constituted of 100% polydimethylsiloxane or PDMS, at room temperature is 2.3-2.8 [Mar99], whereas those of the *a*-, *b*-, *c*-, and *d*-group chemicals (ε_{ch}) are 1.8-2.0, 2.2-2.6, 5-10, and 2.0-2.2, respectively [Woh08]. Note here that the dielectric constants of chemicals under consideration are the values for the liquid phase rather than gas form, because the vapor molecules adsorbed in the polymer are condensed. Therefore, the *c*-group contributes to positive $\Delta C2$, the *b*-group contributes to nearly zero $\Delta C2$, whereas the *a*- and *d*-group contribute to negative $\Delta C2$ (Fig. 4.8).

In CapDet1, the polymer thickness of 0.25 μm is substantially less than the electrode width and gap of 1 μm. Therefore, polymer swelling does affect $\Delta C1$, as the entire polymer thickness is within the distribution of electric field lines for sensing. Polymer swelling always tends to cause positive $\Delta C1$, as an increasing number of electric field lines are enclosed in the polymer. As shown by the results (Fig. 4.9), $\Delta C1$ is positive for all the tested chemicals, even for the c-group chemicals that provide negative $\varepsilon_{ch} - \varepsilon_p$. This can be understood, as the absorption of chemicals is a process of adding dipole moments to the polymer layer. Therefore, regardless of the sign of $\varepsilon_{ch} - \varepsilon_p$, $\Delta C1$ is always positive. Additionally, $\Delta C1$ is strongly dependent upon the value of $\varepsilon_{ch} - \varepsilon_p$. The *c*-group chemicals provide several times higher value of $\varepsilon_{ch} - \varepsilon_p$, and hence several times higher $\Delta C1$, than the non-polar chemical.

The sensitivity of the capacitive detectors also depends on the partition coefficients (K_D) of chemicals between polymer and air. The partition coefficient is defined as the concentration ratio of the chemical distributed in the polymer to that in the air at equilibrium, and is used to describe the extent of vapor adsorption in the polymer. The partition coefficient multiplied by the phase ratio (β), *i.e.*, volume ratio of the air to the polymer in the detector can be used to determine the fraction of chemicals (η) that are adsorbed by the polymer and useful for sensing [Bar04]:

$$\eta = \frac{K_D / \beta}{K_D / \beta + 1} \tag{4.2}$$

On one hand, larger K_D values cause larger η values and hence higher ΔC magnitudes. On the other hand, because the separation columns use the same polymer as the detectors as in *iGC3.c2*, larger K_D values cause longer retention and broader peaks, thereby reducing the ΔC magnitudes. The β for CapDet1 and CapDet2 are 1000 and 160, respectively. The partition coefficients of the *a*-group chemicals between PDMS and air at room temperature [Mar97], as well as the calculated values of η are listed in Table 4.2. From pentane to nonane, the η value substantially increases

(Table 4.2), causing ΔC magnitudes to increase in both detectors (Fig. 4.8 and Fig. 4.9). Compared to nonane, decane has only marginally larger η values but much broader peaks, hence providing slightly smaller ΔC magnitudes in both detectors (Fig. 4.8 and Fig. 4.9). Similar trends are also evident for the *b*-group chemicals in CapDet1 responses (Fig. 4.8). It is worth noting that the partition coefficient describes the chemical distribution only when equilibrium is reached. In the scenario of a μGC detector where continuous flow is present, the actual fractions of chemicals adsorbed by the polymer are possibly smaller than the calculated values in Table 4.2. More detailed understanding of the dynamic distribution of the chemical molecules can be assisted with computational modeling [Mor14].

Table 4.2: Calculation of chemicals partitioned between polymer and air in the detectors

Chemical	Partition coefficient (K_D) [Mar97]	Fraction of chemical in polymer in CapDet1 (η1)	Fraction of chemical in polymer in CapDet2 (η2)
pentane	82	8%	34%
hexane	215	18%	58%
heptane	565	36%	78%
octane	1486	60%	90%
nonane	3908	80%	96%
decane	10280	91%	99%
benzene	296	23%	65%
toluene	815	45%	84%
m-xylene	2190	69%	93%
o-xylene	2710	73%	95%
mesitylene	6150	86%	98%

Further calculations can be performed to elucidate the chemical quantities being analyzed. For example, in Run 5b, the 120 min. sample taken at 0.2 sccm flow rate provided a sampling volume of 24 mL. Hence, the mass of chemicals being sampled and subsequently injected by the preconcentrator was ≈1 ng for the non-polar chemicals and ≈0.2 ng for the mildly-polar chemicals. (The effective mass actually sampled into the preconcentrator was slightly smaller due to the threshold volume as discussed in the following text; nevertheless, this difference was negligible

for the 120 min. sample.) These values represent the lowest mass levels that were experimentally detected by the capacitive detectors.

Additionally, in this effort, considering 4-chlorotoluene as an example, the peak width (measured at half peak height) was 17 s, and hence occupied a volume 0.06 mL in the 0.2 sccm gas flow during separation. Therefore, the maximum concentration of the 4-chlorotoluene peak was ≈0.8 ppm, as 24 mL of the original 2 ppb vapor was now concentrated in the 0.06 mL peak. The K_D of 4-chlorotoluene, as calculated from [Mar97], is ≈5590. This means that only 15% of the 4-chlorotoluene molecules remained in the gas phase as the peak passed through CapDet1. If tested in non-transient steady state with a large head space, this would be comparable to a reading at 120 ppb concentration. This type of correction is necessary when comparing the *iGC3.c2* results to those in which chemical sensors were characterized in steady state.

The capacitive detectors for this effort used OV-1 for the polymer film. Being non-polar, this material is most responsive to non-polar and mildly-polar chemicals. For highly polar chemicals a polar polymer film is recommended. Polar chemicals inherently provide higher $\varepsilon_{ch} - \varepsilon_p$ than the chemicals with lower polarities, and are likely to provide even lower detection limits [Mls06, Pat03].

It is notable that as the detection principle of the interdigitated capacitive detectors can be modeled [Igr06, Mor14], a library of predictable detector responses can be constructed using computational methods. This can reduce the burden of evaluating the technology for a previously untested application.

The peak capacity of the two-column ensemble in the *iGC3.c2* system can be theoretically estimated. The peak capacity is a term describing the maximum number of retention peaks that can be baseline-separated by the column within a given duration. With the assumption that the

theoretical number of plates (N) remains constant for all the VOC species (which is usually valid with <20% variation), the peak capacity (n_{PC}) can be approximated by the following equation [Gru70]:

$$n_{PC} = 1 + \frac{\sqrt{N}}{4} \ln \frac{t_n}{t_0} \tag{4.3}$$

where t_n is the retention time of the n^{th} peak; t_0 is the elution time of an unretained peak, which is equal to the total fluidic volume of the columns divided by the flow rate. The columns used in the *iGC3.c2* system are designed to have similar cross-section and stationary phase thickness as those in the *iGC1* system, and thus similar height equivalent to a theoretical plate (HETP) of ≈2600 plates/m at a flow rate of 0.2 sccm. The two-column ensemble in the *iGC3.c2* system has a total length of 60 cm, therefore a value of N ≈1560 based on Equation (2.5). It also has an estimated cross-sectional area of 5×10^{-4} cm^2 and, leading to a total fluidic volume of 0.03 cm^3. Assuming a flow rate of 0.2 sccm, which is experimentally used, t_0 ≈9 s. Therefore, if t_n is set to be 1 hour, n_{PC} ≈60; if t_n is set to be 10 min., n_{PC} ≈42. In comparison, the experimental results with ≈10 min. long separation intervals (Fig. 4.8 and Fig. 4.9) appeared to provide a peak capacity of ≈20, which was lower than the theoretical estimates. This was likely caused by the discrepancies in the conditions between system-level experiments and the idealized calculation. The calculation is based on the assumption of negligible peak broadening in the vapor injector and detector and of using N_2 as the carrier gas. In the *iGC3.c2* experimental evaluation, the peak injection was provided by the preconcentrator desorption, resulting in the width of a few seconds. The capacitive detectors were based on the chemical diffusion in the polymer layer, contributing to peak broadening. The dead volume in the fluidic connectors and detectors also contributed to peak broadening. Additionally, room air was used as the carrier gas.

In conclusion, the results show the viability of a full μGC system, in which all the components are microfabricated and electronically interfaced. The system has no moving parts, uses room air as carrier gas, and all the fluidic components can be co-fabricated by a common low-cost process. These features can potentially increase the overall applicability of μGC technology. The current manifestation of the system provided a detection limit of 2 ppb for certain chemicals, which is low enough for use in certain applications such as indoor pollutant monitoring. Compared to other reported μGCs that provide comparable performance [Kim11, Zam09], the results in this work are significant because they are provided by a fully microfabricated and integrated system. With further refinement of the electronic hardware and software, it is expected to be suitable for continuous, unmanned monitoring.

In the future, the system platform can be reconfigured for other applications. For example, detectors with different coatings of polymer species can be easily integrated to enhance vapor recognition. More preconcentrators or separation columns can be added to enhance the chromatography. While in the current system a two-stage Knudsen pump is used to demonstrate a scalable architecture, a single-stage Knudsen pump with improved design and implementation is also expected to be capable of driving the system, thereby reducing the system complexity and footprint. Other micro gas pumps can also be integrated in place of the Knudsen pump module.

Chapter 5:

A Monolithic High-Flow Knudsen Pump Using Vertical Al_2O_3 Channels in SOI

This chapter* describes the analysis, design, and microfabrication of a Knudsen pump for high flow generation. The Knudsen pump generates gas streams from the cold end to the hot end using free-molecular flow without moving parts. The designed Knudsen pump has densely arrayed, vertically oriented, 2 μm-wide rectangular channels for providing high flow. The temperature gradient is provided between a thin film metal heater and a gridded Si heat sink in the Knudsen pump structure. The Knudsen pump is fabricated on a single silicon-on-insulator wafer using a four-mask lithographic process. The sidewalls of the rectangular channels are constructed by atomic layer deposition of Al_2O_3 on sacrificial Si channels and subsequent Si etching. The fabricated Knudsen pumps have designed footprints ranging from 0.4-3.2 cm^2. At atmospheric pressure, the fabricated Knudsen pumps provide a maximum measured air flow rate of >200 sccm with response time of <0.5 sec. Experimental results have also shown that these Knudsen pumps are most suitable for pumping at moderate vacuum pressure of ≈200 Torr (27 kPa).

* This chapter describes joint work with Seungdo An.

5.1. Introduction

Gas pumping has been demonstrated by micropumps two decades ago [Ste93]. A majority of gas micropumps are based on the actuation of flexible diaphragms to generate flow [Las04]. Diaphragm actuation mechanisms include electrostatic [Bes13, Bes12, Cab01, Kim10, Kim15], piezoelectric [Ste93, Tan08], and electromagnetic [Son13] methods. Diaphragm actuation is relatively power efficient, but the stress and fatigue in the diaphragm actuation may lead to diaphragm fracture [Yee13] and thus reliability and lifetime issues. In contrast, another type of gas micropump, the Knudsen pump, operates by the phenomenon of thermal transpiration; with no moving parts, long lifetimes have been demonstrated, *e.g.*, ≈11750 hrs of continuous operation [Gup11].

When two chambers are connected by a channel that has a hydraulic diameter that is comparable to or smaller than the mean free path of the gas molecules at the relevant pressure (*i.e.*, $Kn \geqslant 0.1$), the gas flow is in the transition or free molecular regimes. Under these conditions, gas molecules flow from the cold end to the hot end of the narrow channel [Knu50, Rey79].

In order to facilitate thermal transpiration for Knudsen pumps, both microfabricated channels and porous media have been employed. Thermal transpiration channels lithographically microfabricated on silicon substrates were reported in [An14, Gup12, McN05]. These efforts were directed at pumps intended to evacuate blind cavities. The 162-stage Knudsen pump achieved a vacuum pressure of 0.9 Torr (0.12 kPa) at atmospheric ambient pressure, but its flow rate (~10^{-6} sccm) was limited by the resistance of single flow channels connected in a long series [An14]. In contrast, porous media provide numerous nano/micro channels which permit thermal transpiration to occur in parallel, thereby generating high flow. Various porous media, such as silicon aerogel [You03], glass microspheres [You03], naturally occurring zeolite [Gup11], and mixed cellulose

ester (MCE) membranes [Gup11, Pha10], have been used. The MCE-based Knudsen pump generated an air flow rate of ~1 sccm, which was sufficient to demonstrate applications in micro gas chromatography systems for providing gas flow for vapor separation [Liu11, Qin14, Qin14]. Using porous media is a low-cost and facile approach, but the material defects can limit the flow rate. In addition, assembly of porous media into conventionally machined or lithographically fabricated frames can pose challenges to process integration [Gup11, Gup11, Qin14].

This chapter addresses the previously unresolved challenge in lithographic manufacturing of high density thermal transpiration channels for high flow. The channels described in this chapter are vertically oriented through the substrate wafer, permitting dense arrays of parallel channels to achieve high flow rates. In contrast, microfabricated Knudsen pumps that were reported previously [An14, Gup12, McN05] used series connected in-plane channels that allowed very low flow rates (~10^{-6} sccm) even though the compression ratios achieved were very high. Other efforts directed at Knudsen pumps with relatively high flow rates (>0.1 sccm) [Gup11, Gup11, Liu11, Pha10, Qin14, Qin14, You03] utilized porous media. The lithographically microfabricated through-wafer channels described in this chapter have uniform and controllable dimensions, providing design discretion and avoiding non-standard materials.

The design and modeling are described in Section 5.2, the fabrication in Section 5.3, the experimental results in Section 5.4, and discussions and conclusions in Section 5.5.

5.2. Design and Modeling

Description of the Structure

The high-flow Knudsen pump contains three regions (Fig. 5.1): the active pumping area, the thermal isolation zone, and the outer substrate rim. The active pumping area includes arrays of

rectangular, vertical channels (with a =2 μm, b =120 μm, l =20 μm) oriented such that a, b, and l are aligned to x, y, and z directions, respectively. The 2-μm dimension limits the effective hydraulic diameter to approximately this value. It is selected for pumping efficacy in the range of 0.1-1 atmospheric pressure, and for ease of lithographic patterning. The channel sidewalls are made of thin dielectric layers for minimizing the heat conduction through the sidewall and thus the overall power consumption. In the xy-plane above the channel array is another dielectric layer referred to as the "upper dielectric membrane," which has rectangular openings. The upper dielectric membrane provides mechanical support for the dielectric sidewalls from above, whereas the openings serve as the gas outlet windows for the vertical channels. A thin-film metal pattern on top of the upper dielectric membrane serves as the resistive heater. Beneath the channel array is the heat sink with grid-patterned openings. The heat sink dissipates Joule heat laterally to the outer substrate rim, while the grid-patterned openings serve as the gas inlet windows. The outer substrate rim is used for physical handling as well as for attachment to the external setup.

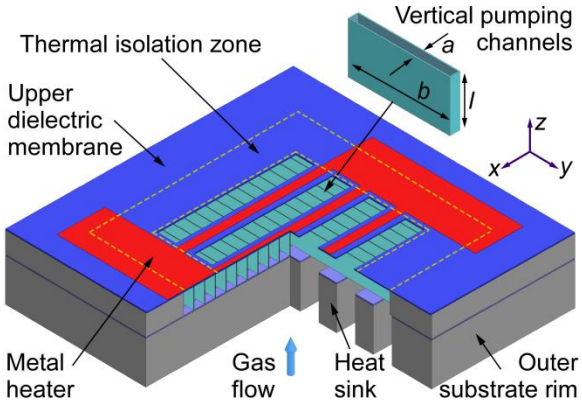

Fig. 5.1: The 3D structural concept of the Knudsen pump.

Between the active pumping area and the outer substrate rim is a region that serves as the thermal isolation zone. This region contains the same vertical channels as the active pumping area, but the channels are capped by the upper dielectric membrane. The region is designed to provide

lateral thermal isolation between the heated active pumping area and the cooler outer substrate rim, thus minimizing the lateral power dissipation which does not contribute to pumping.

In this effort the Knudsen pumps have been fabricated in silicon-on-insulator (SOI) wafers. Thermal transpiration channels traverse a 20-μm thick device layer, which is separated by 0.5 μm thick oxide from a 380-μm handle layer in which heat sinks are formed. The upper dielectric membrane is a stack of two silicon oxide-nitride-oxide (ONO) layers with a total thickness of 3 μm; the resistive heater layer is a Cr/Pt layer (of thickness ≈25/100 nm); the heat sink and the outer substrate rim are formed by bulk silicon. The primary version of Knudsen pumps uses 10-nm thick Al_2O_3 sidewalls for the thermal transpiration channels; this type is labelled "ALD KP". In a more conservative version, the dielectric sidewalls are made of a 100 nm-thick ONO layer; this is named "ONO KP".

In this effort, designs with various pumping areas are studied: the "KP-1.2" has an active pumping area of 1×1.2 mm^2, whereas the "KP-24" has 4×6 mm^2. The "KP-96" is comprised of four KP-24s, providing a total pumping area of 96 mm^2. All the designs have a ≈0.36 mm wide thermal isolation zone surrounding the active pumping area.

Computational Modeling

The Knudsen pump is modeled by a two-step approach: 1) finite element analysis (FEA) of the temperature distribution of the Knudsen pump; and 2) semi-analytical computation of the flow and pressure outputs of the Knudsen pump. Due to the vast span of feature sizes (from 10 nm to 1 cm) in the Knudsen pump, the FEA is divided into two parts: 1(a) lateral temperature distribution over the entire device area (Fig. 5.2(a)); and 1(b) vertical temperature distribution within a single narrow channel (Fig. 5.2(b)), which provides the effective temperature difference that is actually

available for pumping. Only the ALD KP-1.2 is modeled to provide an example illustration of the temperature distribution in the device structure and the resulting performance.

Part 1(a) Because of the symmetrical geometry of the design, only a quarter of the ALD KP-1.2 is modeled. In this simulation, the heat sink, the narrow channels, the upper dielectric membrane, and the heater are modeled as layers of uniform material using equivalent values of thermal conductivities (Table 5.1). For example, the narrow channel region is a composite of air and Al_2O_3 sidewalls, and is modeled as a layer of uniform material with weighted average thermal conductivity of air and Al_2O_3. The thermal conductivity of amorphous thin-film Al_2O_3 has been experimentally determined to be 1.8-3.3 W/mK in a 50-600°C range [Cap13].

Table 5.1: Material properties assumed in the FEA Part 1(a)

Structure	Material composition	Thermal conductivity assumed (W/mK)
Narrow channels	Al_2O_3/air	0.3-0.4, temperature dependent
Heat sink	Si/air	56
Upper ONO membrane	ONO/air	11
Heater	Cr/Pt/air	15

The bottom of the outer substrate rim is assumed to be maintained at 295 K (which is the ambient temperature during experimental testing), whereas the heater layer is supplied with input power densities (*i.e.*, power per unit pumping area) of 0-0.5 W/mm^2. From the temperature distribution (Fig. 5.2a), it is observed that the temperature reaches maximum in the center of the active pumping area, and gradually decreases in the vicinity of the thermal isolation zone. The average temperatures on the top and bottom surfaces of the narrow channels (*i.e.*, T_h and T_c, respectively, which are plotted by the circular-dotted lines in Fig. 5.2c) are used for subsequent calculations. The value of T_h increases from room temperature to 203°C (476 K) as the input power increases to 0.5 W/mm^2, whereas T_c increases only to 31°C (304 K).

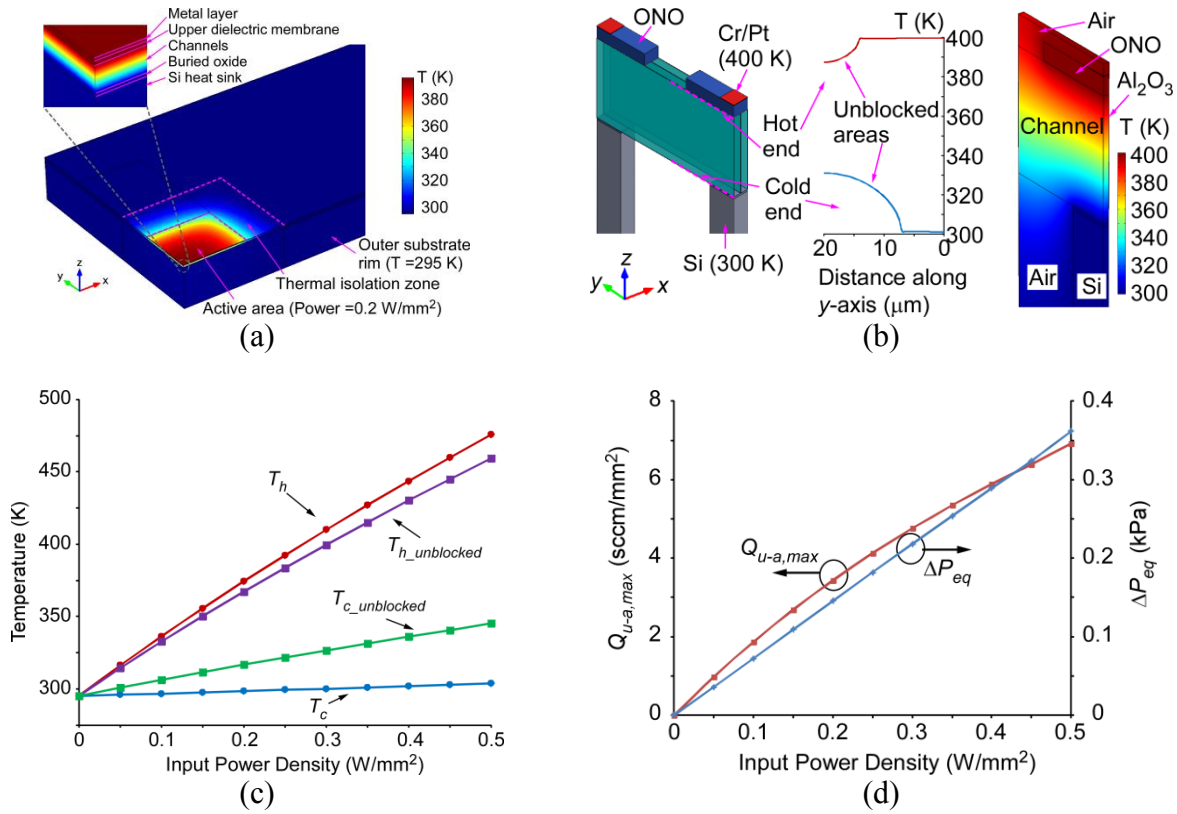

Fig. 5.2: Modeling of the Knudsen pump KP-1.2. (a) FEA on lateral temperature distribution. (b) FEA on temperature of unit-area structure. (c) Resulting temperatures with various input powers. (d) Calculated flow and pressure.

Part 1(b) As illustrated in the unit- channel structure of the Knudsen pump (Fig. 5.2b), the hot and cold ends of the narrow channels are partially blocked by the upper dielectric membrane above and the heat sink underneath. This part explores the temperatures of the unblocked regions – which are effective for pumping – with respect to the temperatures of the heater and the heat sink.

In the unit-area structure, a temperature difference (T_h-T_c) of 100 K is applied between the heater and the heat sink (Fig. 5.2b). From the simulation results, the average temperature of the unblocked area on the hot end of the narrow channels ($T_{h\_unblocked}$) is 9.5 K lower than that of the heater (which is T_h); the average temperature of the unblocked area on the cold end of the narrow channels ($T_{c\_unblocked}$) is 24.2 K higher than that of the heat sink (which is T_c). Consequently, the temperatures effective for pumping with arbitrary T_h and T_c can be calculated by:

$$T_{h\_unblocked} = T_h - 9.5\% \times (T_h - T_c) \tag{5.1}$$

$$T_{c\_unblocked} = T_c - 24.2\% \times (T_h - T_c) \tag{5.2}$$

with the results shown in Fig. 5.2c. The nonlinearity in the curves is caused by the temperature dependence of the thermal conductivities of air and Al_2O_3.

Part 2 In this part, the flow rate generated by the Knudsen pump is calculated using the temperatures $T_{h\_unblocked}$ and $T_{c\_unblocked}$ as derived in Part 1, using the following equation that covers an extended flow regime of $Kn \geq 0.02$ [Sha99]:

$$M_{std} = \left(Q_T \frac{\Delta T_{KP}}{T_{avg}} - Q_P \frac{\Delta P_{KP}}{P_{avg}} \right) \frac{\pi a^2 b P_{avg}}{l} \left(\frac{m}{2 k_B T_{avg}} \right)^{\frac{1}{2}} \tag{5.3}$$

where M_{std} is the standard flow rate through a rectangular channel; ΔT ($=T_{h\_unblocked} - T_{c\_unblocked}$), T_{avg} ($=(T_{h\_unblocked}+T_{c\_unblocked})/2$), ΔP, and P_{avg} are the temperature difference, average temperature, pressure head, and average pressure between the hot end and the cold end of the channel, respectively; a, b, and l are the channel width, depth, and length, respectively ($a \leq b$, Fig. 5.1); m is the mass of the gas molecule; k_B is the Boltzmann constant; and Q_T and Q_P are the thermal creep and viscous flow coefficients, respectively, numerically provided by Sharipov [Sha99], and dependent on the rarefaction parameter δ_{avg}, which is the inverse of Kn.

As the gas flow is partially blocked by the upper dielectric membrane and the heat sink structure, the actual flow is only a fraction of that calculated from Equation (5.3). The value of this fraction can be represented by percentage of pumping area that is unblocked ($f_{unblocked}$). In the particular designs described in this chapter, $f_{unblocked}$=42.4%.

For comparing the performance of Knudsen pumps with various pumping areas, the output flow rate per pumping area ($Q_{u\text{-}a}$) is of interests. The output flow rate per pumping area reaches maximum ($Q_{u\text{-}a,max}$) when the pressure head is zero, *i.e.*, $Q_{u\text{-}a,max} = Q_{u\text{-}a}|_{\Delta P=0}$. It can be calculated

by the product of Equation (5.3) and the number of channels per pumping area, divided by the gas density.

The blocking pressure (ΔP_{eq}), which is the maximum pressure head generated by the Knudsen pump at the zero-flow condition, can also be calculated by solving the following equation [Sha96]:

$$\frac{P_{avg} + \Delta P_{eq}/2}{P_{avg} - \Delta P_{eq}/2} = \left(\frac{T_{h\_unblocked}}{T_{c\_unblocked}} \right)^{Q_T/Q_P} \tag{5.4}$$

The calculated blocking pressure is roughly proportional to the input power density (Fig. 5.2d). The calculated maximum flow rate per pumping area shows a concave function to the input power density (Fig. 5.2d), which mainly results from the increase of average temperature with increasing input power density. The modeled results are compared with the experimental results in Section 5.4.

5.3. Fabrication

The fabrication process uses four masks. The important features include: (1) A SOI device layer mold, formed by channel etching using deep reactive ion etching (DRIE) and conformal refilling using Al_2O_3 sidewall material and a polySi sacrificial layer. (2) A Cr/Pt resistive heater on the upper dielectric membrane. (3) A heat sink formed by DRIE of the SOI handle layer.

The process begins with creating the vertical trenches in the SOI device layer, using DRIE on the front side of the SOI wafer. Each trench has an area of 2 × 118 μm^2 and a separation of 2 μm from adjacent ones (Fig. 5.3a). The SOI buried oxide acts as the etch stop. Next, the vertical trenches are coated by an Al_2O_3 layer (thickness ≈10 nm) using ALD (Fig. 5.3b). The process is followed by refilling the vertical trenches with a polySi layer (thickness ≈1.5 μm), using low-pressure chemical vapor deposition (LPCVD). Then the polySi on the top surface of the SOI

device layer is dry etched until the top surface of the Al_2O_3 layer is fully exposed, using an isotropic RIE recipe with high selectivity of silicon over Al_2O_3 (Fig. 5.3c). Alternatively, this step can potentially be replaced by chemical mechanical polishing (CMP). Next, the upper dielectric membrane is formed by deposition of two stacks of ONO using plasma-enhanced chemical vapor deposition (PECVD). Each ONO stack is composed of one nitride layer (thickness ≈0.7 μm) sandwiched by two oxide layers (thickness ≈0.4 μm); the total two-stack ONO thickness ≈3 μm. The nitride and oxide thicknesses are adjusted to provide a mild tensile stress level of ≈56 MPa (Table 5.2). The thickness of these dielectrics smoothens the topographical variation generated during the previous dry etching step. The ONO stacks are patterned by RIE (Fig. 5.3d). The Cr/Pt resistive heater (thickness ≈25/100 nm) is deposited by evaporation, and patterned by a lift-off process.

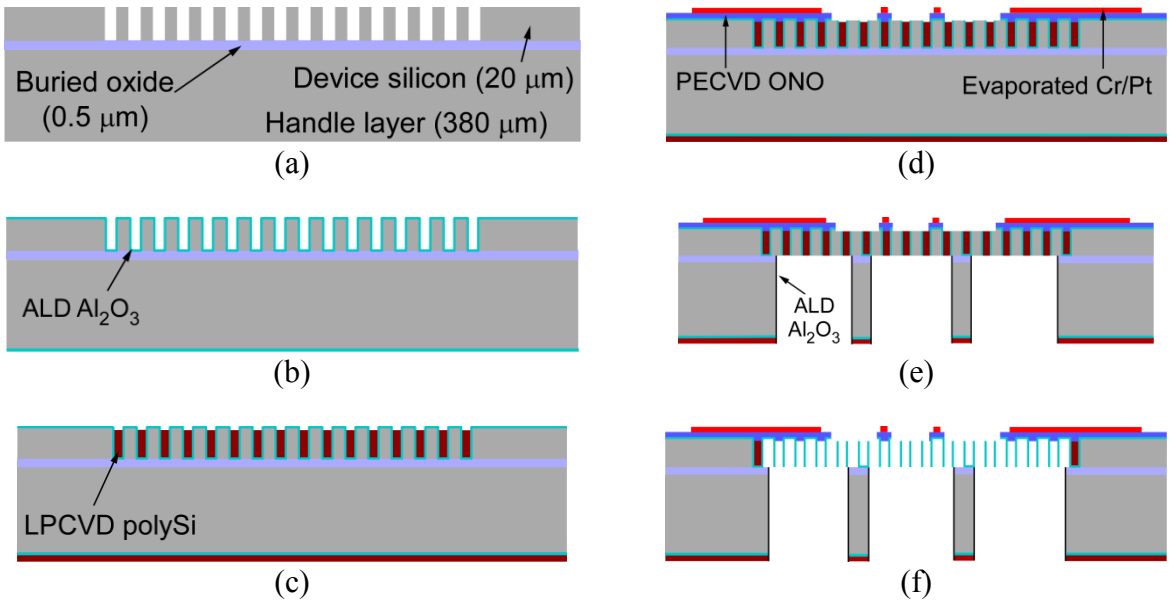

Fig. 5.3 Fabrication process of the ALD KPs. (a) DRIE to create channels. (b) ALD 10 nm-thick Al_2O_3 layer. (c) LPCVD channel refill and plasma etching. (d) Deposition and patterning of the upper ONO layer and the Cr/Pt heater. (e) DRIE to create the heat sink. (f) XeF_2 etching of sacrificial Si.

Table 5.2: Measured thickness and residual stress of each layer

Layer	Thickness (μm)	Residual stress (MPa)
SOI device layer/buried oxide/handle layer	20/0.5/380	NA
polySi	1.5	NA
Upper dielectric membrane (O/N/O-O/N/O)	0.4/0.7/0.4-0.4/0.7/0.4	+56
Al_2O_3	0.0107	+304
Cr/Pt	0.025/0.1	+967

The heat sink is formed by micromachining from the back side of the SOI wafer. In the preceding deposition steps, the SOI handle layer is covered with Al_2O_3 and polySi. With an etching mask of photoresist, the Al_2O_3 and polySi layers are etched using RIE; the SOI handle layer is etched through using DRIE; and the SOI buried oxide layer is etched using RIE. To protect the heat sink from subsequent XeF_2 etching, a dielectric layer inert to XeF_2 is required to coat the sidewalls of the heat sink; however, the dielectric layer must not coat the bottom of the heat sink, otherwise the gas inlet of the Knudsen pump will be blocked. This protection is achieved by depositing an Al_2O_3 layer (thickness ≈10 nm) on the heat sink using ALD, and etching the Al_2O_3 layer using RIE without masking. This step results in Al_2O_3 coating only on the sidewalls of the heat sink, as the anisotropic RIE has a higher etch rate of Al_2O_3 on the bottom of the heat sink than on the sidewall (Fig. 5.3e). This process is similar to the SCREAM process [Zha93]. Finally, the sacrificial silicon and polySi in the SOI device layer are etched using XeF_2 dry gas, thereby providing the thermal transpiration channels (Fig. 5.3f).

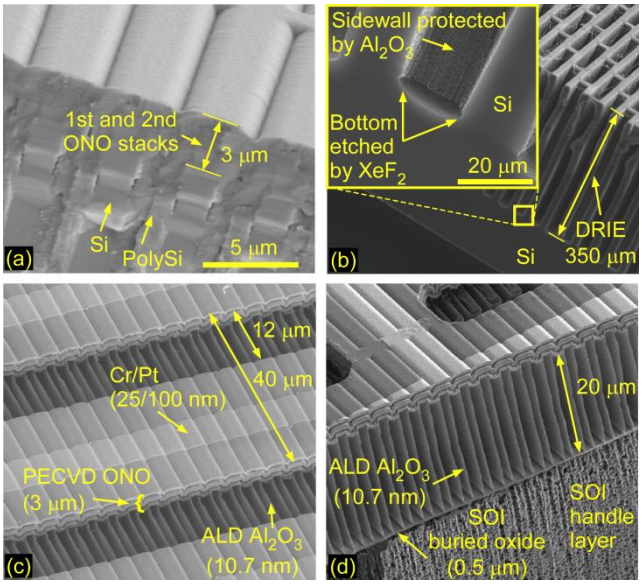

Fig. 5.4: SEM images of the Knudsen pump during and after fabrication. (a) Top surface with ONO coating. (b) Gridded Si heat sink sidewall protected by Al_2O_3. (c) Top view of final structure. (d) Side view of final structure.

The intermediate and final fabrication results are illustrated by scanning electron microscope (SEM) images in Fig. 5.4. The image in Fig. 5.4a shows a cross-section of the wafers after deposition of 3 μm PECVD ONO. The image in Fig. 5.4b shows the sidewall protection of the heat sink provided in the XeF_2 step by the Al_2O_3 layer. The bottom of the DRIE trench shows clear undercut profiles, which verifies that the bottom (unprotected by Al_2O_3) is etched by XeF_2 whereas the sidewall (protected by Al_2O_3) is intact. From the SEM images of the final Knudsen pump structure (Fig. 5.4c and d), it is evident that the Al_2O_3, silicon oxide, and Cr/Pt structures remain intact during XeF_2 etching; the silicon nitride is partially etched by XeF_2 but the overall structure is not damaged or buckled. Vertical channel sidewalls that are made of 10 nm-thick Al_2O_3 show no noticeable defects. The photographs of the fabricated ALD KPs are shown in Fig. 5.5. The KP-1.2 has a total footprint of 4×10 mm^2, the KP-24 8×10 mm^2, and the KP-96 16×20 mm^2.

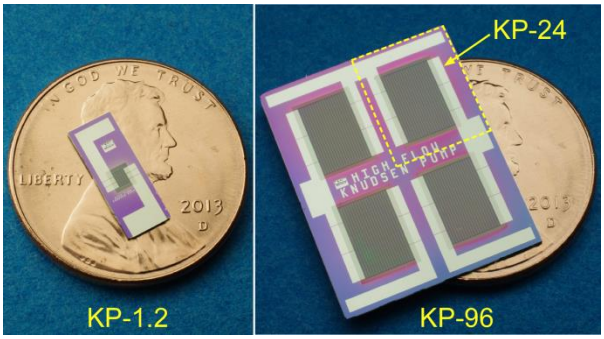

Fig. 5.5: Photographs of the fabricated high flow Knudsen pumps. (The KP-24 is a quarter of the KP-96 as shown by the outlines.)

The more conservative version of Knudsen pumps, *i.e.*, the ONO KPs, is microfabricated using a similar process [An14]. The main difference in the fabrication of the ONO KPs is that the channel sidewalls are formed by LPCVD of a 100 nm-thick ONO layer.

5.4. Experimental Results

The performance of the Knudsen pumps operated both at atmospheric pressure and in vacuum was evaluated, using two different test setups. The evaluation involved both the steady state and transient performance at various power levels. In addition, a lifetime test was also performed. In this effort, the pumping medium was room air.

Test setup

The test setup for evaluating the Knudsen pump performance at atmospheric pressure is shown in Fig. 5.6a. The device under test (DUT) was mounted on an Al plate, which served as a thermal ground, with perforations for providing fluidic connection to the gas inlet of the KP. It was ensured that the outer rim of the DUT was in good thermal contact with the Al block; epoxy was applied around the perimeter to prevent leakage. A computer-controlled switch was used to control the power supplied to the DUT. A commercial pressure sensor – Model # MPX5010DP, Freescale Semiconductor, Inc., AZ – and flow meters – Model # MW-20SCCM-D for measuring the KP-

1.2, and model # MW-1SLPM-D for measuring the KP-24 and KP-96, Alicat Scientific, Inc., AZ – were connected to inlet of the DUT. Tubes with various internal diameters were used to alter flow resistance, and consequently, the load, presented to the DUT.

Knudsen pumps are often operated in tandem with roughing pumps. For example, a roughing pump can be used to drop the pressure of a cavity from atmospheric pressure down to ~100 Torr (13 kPa), with further evacuation to be provided by one or a series of Knudsen pumps. Certain applications like gas chromatography also require continuous flow at modest pressure. Therefore, measuring the Knudsen pump operation in vacuum provides insights into the prospect of such applications.

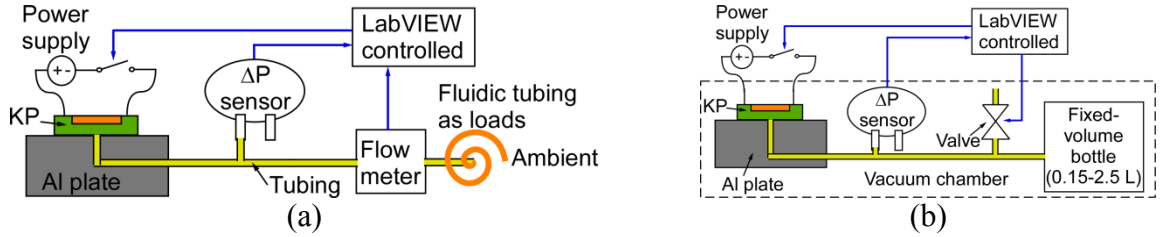

Fig. 5.6: (a) Test setup for measuring the Knudsen pump operation at atmospheric pressure. (b) Test setup for measuring the Knudsen pump operation in vacuum.

For evaluating the DUT operation at low pressure, the entire test setup was placed in a vacuum chamber equipped with electrical feedthroughs for electronic control and readout (Fig. 5.6b). The DUT was used to evacuate the air in a glass bottle with fixed and known volume. Glass bottles with different volumes were selected in the range of 0.15-2.5 L, depending on the pumping capacity of the DUT. A commercial differential pressure sensor (Model # MPX5010DP, Freescale Semiconductor, Inc., AZ) continuously monitored the time-dependent pressure head generated by the Knudsen pumps. The flow rate was calculated from the measured time-dependent pressure variation, similar to the method reported in [Roj13]. A commercial solenoid valve (Model # U8256B045V, ASCO Valve, Inc., NJ) was used both to reset the pressure head and to bypass the

flow before the pressure level in the vacuum chamber stabilized, thereby preventing flow surging through the Knudsen pumps.

Experimental results

The steady state performance of the ALD KPs operated at atmospheric pressure is shown in Fig. 5.7a. In Fig. 5.7a, each data point indicates the flow rate (Q) and pressure head (ΔP) generated by the ALD KP-1.2 with a specific input power. The data exhibits a linear compromise between the flow rate and pressure head (Fig. 5.7a). Similar plots were also obtained from the ALD KP-24 (Fig. 5.7b) and ALD KP-96 (Fig. 5.7c). The highest flow rate measured in this effort reached ≈211 sccm. This was obtained from the ALD KP-96 with an input power of 37 W and a pressure head of 0.09 kPa. Projecting along the Q-ΔP line, the KP-96 was expected to produce a flow rate of ≈290 sccm at zero pressure head, an idealized condition. The maximum blocking pressures created by the ALD KPs were in the rage of 0.35-0.4 kPa. Although increasing the input power is expected to increase the output flow and pressure further, these tests were not attempted in order to prevent damage from overheating. In an ongoing lifetime test, the ALD KP-24 devices have operated continuously for over 13,000 hours (1 year, 6 months), during which the flow rate gradually reduced by ≈30% from the initial value (Fig. 5.7d). Most of the loss in flow occurred after the first year of continuous operation. The decrease in the flow rate was likely caused by dust accumulation at the pump inlet, where no filter was used.

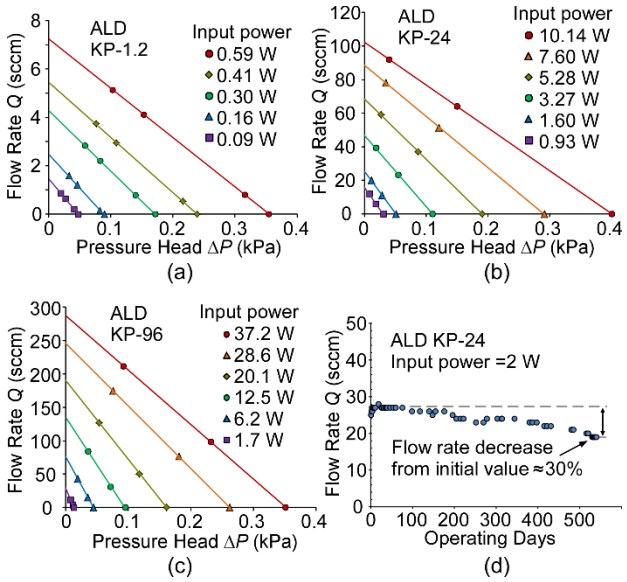

Fig. 5.7: Experimental results on the air flow rate and pressure head created by the Knudsen pumps – (a) ALD KP-1.2, (b) ALD KP-24, and (c) ALD KP-96 – at atmospheric pressure with various input powers. (d) Lifetime test on the ALD KP-24.

As evident from Fig. 5.8a, at a given areal power density, the ALD KP-1.2 provided higher maximum flow rate per pumping area and lower blocking pressure than the ALD KP-24 and ALD KP-96. This was likely caused by the variations in the temperature distribution between the three designs. Possible variations in the loading presented in the test setup may have also played a role. The modeling results of the ALD KP-1.2 (in Section 5.2) are plotted in Fig. 5.8a and Fig. 5.8b. These results match the experimental results with <15% discrepancy. The normalized performance of the ONO KPs is plotted in Fig. 5.8c and Fig. 5.8d. The same overall trend is evident: at a given power density, the ONO KP-1.2 provided higher maximum flow rate per pumping area and lower blocking pressure than the ONO KP-24 and ONO KP-96. However, the performance of the ONO KPs was lower than that of the ALD KPs. With the same power density, the ALD KPs produced 5x in the maximum flow rate per pumping area and 2x in the blocking pressure compared to the ONO KPs. The lower performance of the ONO KPs was likely caused

by the higher heat conduction through the 100 nm-thick ONO sidewalls, as well as the nonidealities in the fabricated structures [An14].

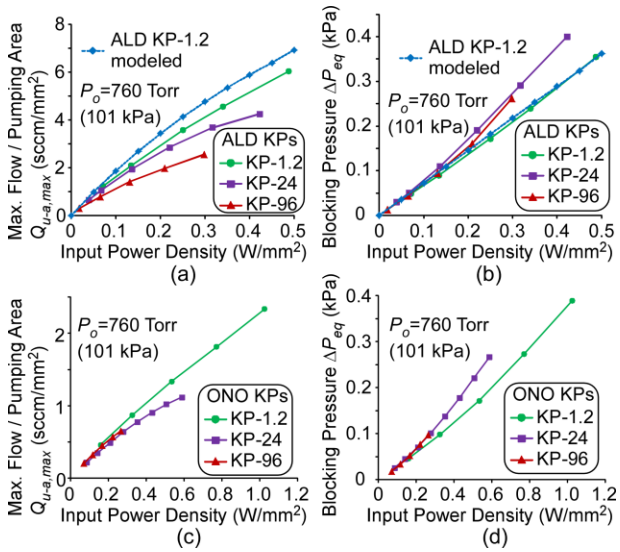

Fig. 5.8: Experimental performance of the Knudsen pumps operated at atmospheric pressure. (a) The maximum flow rates per unit pumping area of the ALD KPs. (b) The blocking pressures of the ALD KPs. (c) The maximum flow rates per unit pumping area of the ONO KPs. (d) The blocking pressures of the ONO KPs. The Knudsen pump output flow rate (Q) and input power are normalized to the pumping area ($A_{pumping}$). Mathematically, $\Delta P_{eq} = \Delta P|_{Q=0}$, and $Q_{u\text{-}a,max} = (Q/A_{pumping})|_{\Delta P=0}$.

The transient flow and pressure head responses of the ALD KPs were also measured by switching the input power. The transient flow responses were obtained under the condition of maximum measurable flow, *i.e.,* no extra tubular loading. The transient ΔP responses were obtained under the maximum-ΔP condition, *i.e.*, gas flow being fully blocked. After the input power was turned on or off, the ALD KPs showed <0.5 sec. response time for reaching 90% of the steady state values (Fig. 5.9). This response rate is ~20x faster than previously reported Knudsen pumps [Gup11, Pha10]. Since the measured response time was the aggregate of both the thermal response time of the Knudsen pump itself and the fluidic response time of the test setup, faster response can be expected with reduced dead volume in the test setup.

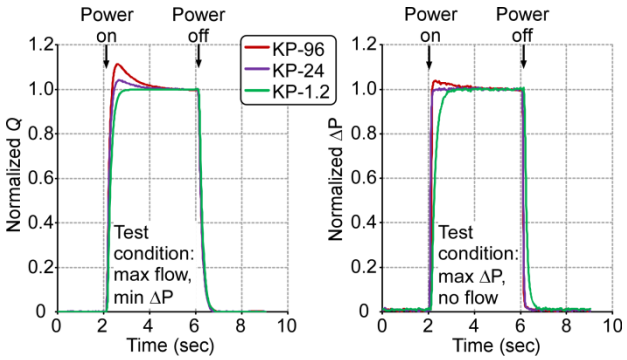

Fig. 5.9: Transient responses of flow and pressure head generated by various ALD KPs. The transient flow and pressure head are normalized to the steady state magnitudes.

Knudsen pump operation in vacuum

The performance of the Knudsen pumps operated in vacuum was evaluated by the measured time-dependent pressure head response. The volume flow rate response can be calculated from the mass transfer rate of air molecules being withdrawn from the bottle, which in turn can be calculated from the measured transient pressure head response, using the following equations:

$$Q = \frac{1}{\rho_{std}} \cdot \frac{dm_{air}}{dt} = \frac{M_{air}}{\rho_{std}} \cdot \frac{dn}{dt} \tag{5.5}$$

where m_{air} and n are the mass and number of moles of air molecules withdrawn in time period t, respectively; ρ_{std} is the air density at standard conditions; and M_{air} is the molar mass of air. With the application of the ideal gas law, the volume air flow rate can be further derived as:

$$Q = \frac{M_{air}}{\rho_{std}} \cdot \frac{V}{R \cdot T} \cdot \frac{dP}{dt} \tag{5.6}$$

where V is the total volume of air being evacuated (which is mainly contributed by the fixed-volume bottle), R is the universal gas constant, T is the ambient temperature, and P is the pressure of air being evacuated. Numerically $\frac{dP}{dt}$ is equal to $\frac{d\Delta P}{dt}$.

As the Knudsen pumps had demonstrated rapid (<0.5 sec.) response, which was much shorter than the duration of the time-dependent experiment (typically ≈50 sec.), the Knudsen pumps were

assumed to reach quasi-steady-state operation during the experiment (*i.e.*, the Knudsen pumps reached steady state within each observation interval). Therefore, the measured pressure head and calculated flow rate at each time interval could be used directly to indicate the performance of the Knudsen pumps operated in vacuum. As shown in Fig. 5.10, the measured pressure head response and the corresponding flow response present a linear relationship. To verify this method, the responses of the Knudsen pumps operated at atmospheric pressure were also evaluated by time-dependent measurements (*e.g.*, the red line in Fig. 5.10a for ALD KP-1.2). This response matched that obtained using a flow meter directly (*i.e.*, the green line in Fig. 5.7a). The measured flow *vs*. pressure responses of the ALD KP-1.2 at various ambient pressures (20, 70, 200, and 760 Torr) are shown in Fig. 5.10a. It is evident from Fig. 5.10b that the ALD KP-1.2 provided increasing output flow rate with increasing ambient pressure, but the blocking pressure was highest at an ambient pressure of ≈200 Torr (27 kPa). A similar trend can also be observed from the response of the ONO KP-1.2 (Fig. 5.10c and d). Considering both the output flow rate and blocking pressure, the Knudsen pumps described in this work were most amenable for operation at 200 Torr (*i.e.*, P_o =200 Torr).

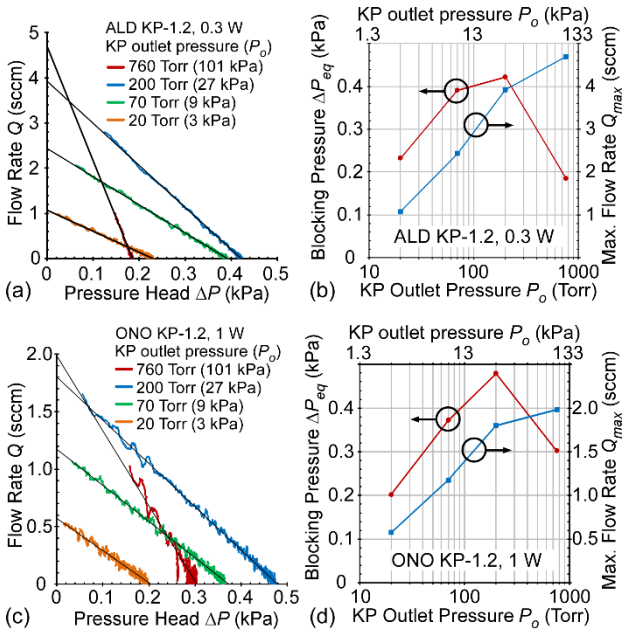

Fig. 5.10: Measured performance of the Knudsen pumps operated in vacuum. (a) ALD KP-1.2 with 0.3 W input power. (b) ONO KP-1.2 with 1 W input power.

5.5. Discussion and Conclusion

Benchmarking

Fig. 5.11 compares various gas micropump technologies in terms of the maximum flow rate per pumping area measured at atmospheric pressure. The Knudsen pumps in this effort demonstrate a measured maximum flow rate per pumping area among the highest of micropumps, and ~200x higher than previously reported Knudsen pumps. Additionally, the Knudsen pumps reported in this effort are ~20x faster than prior Knudsen pumps because of the low thermal mass in the heating zone, which is constituted by the Cr/Pt heater and the upper dielectric membrane.

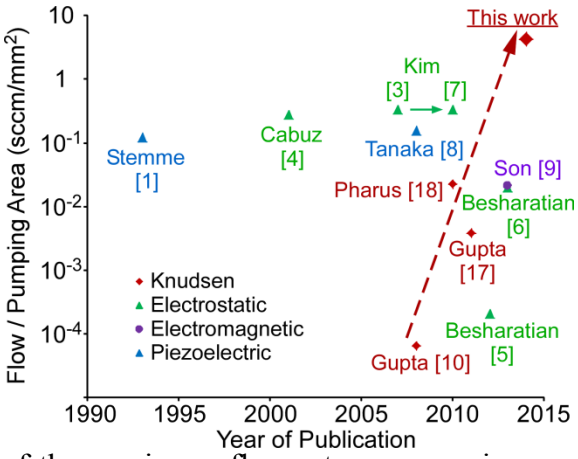

Fig. 5.11: Benchmarking of the maximum flow rate per pumping area provided by various gas micropump technologies.

It is worthwhile to assess the gas flow pumping efficiency, *i.e.*, the ratio of output flow rate to input power. Compared to electrostatic-actuated micropumps [Cab01, Kim10, Kim15], Knudsen pumps, being thermally actuated, are more than an order of magnitude lower in efficiency; however, the advantages of the Knudsen pumps lie in the ultra-high reliability and long lifetime. Compared to the MCE-based Knudsen pumps (which provided the highest efficiency among prior Knudsen pumps) [Gup11, Qin14], the Knudsen pumps described in this effort provide ≈25x higher efficiency.

Experimentally measured maximum flow rate per pumping area and blocking pressure of the ALD KP-1.2 are <15% different from the modeling results. Such a discrepancy is likely due to the inaccuracies of material parameters used in the FEA model (such as the thermal conductivities of thin-film Al_2O_3 and ONO), as well as the approximations represented by the mathematical model for rectangular channels [Sha99].

With the same input power density, the KP-24 has a higher average temperature than the KP-1.2. This is because the heat generated in the active pumping area dissipates laterally to the outer substrate rim. Such heat dissipation in the KP-24 is less efficient, as the KP-24 has a larger active

pumping area. The higher average temperature, when applied with the mathematical model [Sha99], yields higher blocking pressure and lower maximum flow rate per pumping area for the KP-24. This was validated by the experimental results presented in Fig. 5.8.

The KP-96, which is the composite of four KP-24s, is expected to have the same blocking pressure and maximum flow rate per pumping area as the KP-24. This was validated by the results presented in Fig. 5.8b. However, Fig. 5.8a indicates that the ALD KP-96 yields a smaller maximum flow rate per unit pumping area than the ALD KP-24. This is likely due to the limitation in the test setup (Fig. 5.6a), in which the fluidic connections present more significant flow loading when the flow rate increases.

Discussion on Ideal Structures

It is instructive to consider the fundamental performance constraints that might be imposed by an ideal Knudsen pump structure that includes only the vertical thermal transpiration channels ($a/b/l$ =2/120/20 μm). It is assumed that a temperature gradient can be applied along the channels without any lateral power dissipation. It is also assumed that none of the channels are blocked by a membrane as in practice. If the channels have infinitesimal sidewall thickness (*i.e.*, 100% of power dissipates through air), a power density of 0.2 W/mm^2 can generate a maximum flow rate per pumping area of 21 sccm/mm^2. If the channels have 10 nm-thick Al_2O_3 sidewalls, the same power density can generate a maximum flow rate per pumping area of 16 sccm/mm^2 because of a lower temperature gradient (Table 5.3). This means that the 10 nm-thick Al_2O_3 sidewalls reduce the performance of the ideal structure with zero sidewall thickness by 24%. The actual designed structure further reduces the performance, resulting in a maximum flow rate per unit pumping area that is only 14-16% of that provided by the ideal structure with infinitesimal sidewalls thickness and no blocked channels (Table 5.3).

Table 5.3: Comparison between ideal and actual structures.

Assuming input power =0.2 W/mm^2	Ideal structure with 0 nm sidewall	Ideal structure with 10 nm sidewall	ALD KP-1.2 modeled results	ALD KP-1.2 test results
ΔT (K)	133	100	50	NA
ΔP_{eq} (kPa)	0.396	0.290	0.146	0.137
$Q_{u\text{-}a}$ (sccm/mm^2)	21	16	3.4	2.9

Discussion on Channel Width for Thermal Transpiration

The thermal transpiration channels have a width of 2 μm, resulting in a Knudsen number *Kn* of ≈0.04 at atmospheric pressure. Such a *Kn* value, as calculated using the mathematical model [Sha99], favors a high flow rate but yields a low blocking pressure. Nevertheless, such a dimension is more amenable to the pumping operation at a vacuum pressure where the mean free path of air molecules is more close to the channel width. In addition, gas in vacuum pressures has lower thermal conductivity, thus reducing the power consumption of the Knudsen pump. For example, as demonstrated in Fig. 5.10a, the ALD KP-1.2 operated at an ambient pressure of ≈200 Torr provided twice blocking pressure with only 15% less in the maximum flow rate per pumping area as compared to that operated at atmospheric pressure. Therefore, the Knudsen pump technology in this effort can be a good candidate for use in tandem with a roughing pump (*e.g.* a diaphragm actuation-based micropump) to generate both vacuum and high flow rate simultaneously; in such configuration, the latter generates pressure drops in the low-vacuum or near-atmospheric range whereas the former generates pressure drops in higher-vacuum range.

The 2 μm channel width is selected in this effort mainly because the lithography and DRIE processes place constraints on further downscaling in the channel width. If desirable, redesign is possible to increase the blocking pressure even for operation at atmospheric pressure. In a simple calculation, if the Knudsen pump were fabricated with 1 μm-wide channels with 5 nm-thick Al_2O_3

sidewalls, the blocking pressure would be tripled while the flow rate would only be reduced by 10% with the same input power at atmospheric pressure.

Conclusion

In summary, this effort explores a monolithic, fully lithographic microfabrication approach for making a Knudsen pump for high-gas-flow generation. Vertical channels are constructed in dense arrays for parallel pumping, and channel sidewalls can be made of Al_2O_3 layers as thin as 10 nm to minimize power consumption. For characterizing the Knudsen pump microfabricated by such techniques, this chapter emphasizes on the evaluation of single-stage Knudsen pumps with various pumping areas operated at various ambient pressures. The experimentally measured Knudsen pump output air flow rate at atmospheric ambient pressure has reach over 200 sccm, with maximum measured flow per unit-area of ≈4.3 sccm/mm^2. Detailed modeling is conducted to study the temperature distribution, and flow and pressure generation of the fabricated Knudsen pump, which shows <15% discrepancy from test results. Experimental results indicate that the Knudsen pumps as described in this chapter are most suitable for pumping at ≈200 Torr absolute pressure.

Based on the Knudsen pump technology described in this chapter, potential applications can be envisioned. For example, a multi-stage Knudsen pump can be configured, which provides smaller flow rate and higher pressure head for micro gas chromatographs and mass spectrometers. Additionally, the fast response provides promise in applications that requires rapid flow switching. Future work includes tailoring the fabrication process for achieving both high flow and high pressure head simultaneously.

Chapter 6:

Arrayed Architectures for Multi-stage Si-Micromachined High-Flow Knudsen Pumps

This paper reports an evaluation and a comparison of two architectures for implementing Si-micromachined high-flow Knudsen pumps. Knudsen pumps, which operates on the principle of thermal transpiration, have been shown to have great promise for micro-scale gas phase fluidic systems such as micro gas chromatographs. Simultaneously achieving both high flow rate and adequate blocking pressure has been a persistent challenge, which is addressed in this work by combining multiple pumps in series and addressing the resulting challenges in thermal management. The basic building block is a Si-micromachined pump with ≈100,000 parallel channels in a 4x6 mm^2 footprint. In the primary approach, multiple pump stages are stacked vertically with interleaved Si-micromachined spacers. A stacked 4-stage Knudsen pump has a form factor of 10x8x6 mm^3. In an alternate approach, multiple stages are arranged in a planar array. The experimental results demonstrate multiplication of output pressure head with the number of stages, while the flow rate is maintained. For example, a stacked 4-stage Knudsen pump with 8 W power operated at atmospheric pressure provided a blocking pressure 0.255 kPa, which was 3.6x of that provided by a single-stage pump with 2 W power; while both provided ≈30 sccm maximum flow rate. The performance can be customized for practical applications such as micro gas chromatography.

6.1. Introduction

The Knudsen pump is a motionless gas based on the phenomenon of thermal transpiration. Thermal transpiration typically occurs in narrow channels where the gas molecules are constrained in free molecular or transition regimes, *i.e.*, the hydraulic diameter of the channel is smaller than or comparable to the mean free path of the gas molecules. When a temperature gradient is applied along such narrow channels, the gas molecules tend to move from the cold end to the hot end of the channels [Knu50, Rey79]. As the mean free path of air molecules at atmospheric pressure is ≈70 nm, the thermal transpiration effect favors miniaturization of the flow channels, which can be provided by microfabrication. Compared to motion-based microfabricated gas pumps, which typically use membrane actuation to compress and transport gas [Cab01, Kim15, Son13, Ste93], the Knudsen pump provides high reliability and long lifetime [Gup11].

Two important performance metrics for micro gas pumps are flow rate and pressure head, *i.e.*, pressure difference generated between the outlet and inlet of the pump. The target pressure can vary widely, depending on the application. For example, many vibratory microgyroscopes require a vacuum environment, typically of 10^{-7}-10^{-2} kPa (10^{-6}-10^{-1} Torr) absolute pressure, to reduce viscous damping [Liu09]. While such vacuum levels are initially provided by hermetic packaging apparatus, the vacuum can or modulated by integrated micropumps [An14, Gre13]. Another example is that of micro gas chromatographs (μGC), which require a flow rate of 0.2-1 sccm and pressure head of 1-10 kPa [Kim11, Qin14, Qin14]. These requirements can be met by some certain Knudsen pumps [Gup11] and electrostatic peristaltic pumps [Kim15], and have been experimentally demonstrated in certain μGC configurations [Kim07, Liu11, Qin14, Qin14].

The performance of micro gas pumps can be improved by arranging multiple pumps into an array. In general, when the pumps are connected in parallel, the total output flow rate is increased.

For Knudsen pumps, connecting multiple pumps in parallel is in principle equivalent to using a larger pumping area for a single pump [An15]; connecting pumps in series to form multi-stage pumps, the total output pressure head is increased. By arranging the pumps with both serial and parallel connections, the flow-pressure head characteristics can be tuned in a flexible manner. Unlike the parallel arrangement where all the pump units share a common fluidic inlet and outlet, the fluidic connections in multi-stage pumps can pose challenges to microfabrication and performance.

For Knudsen pumps, the mass flow rate through a rectangular narrow channel provided by thermal transpiration can be estimated by the following equation [Sha99]:

$$M_{avg} = \left[Q_T \frac{\Delta T}{T_{avg}} - Q_P \frac{\Delta P}{P_{avg}} \right] \frac{\pi a^2 b P_{avg}}{l} \left[\frac{m}{2 k_B T_{avg}} \right]^{\frac{1}{2}} \tag{7.1}$$

where ΔT, T_{avg}, ΔP, and P_{avg} are the temperature difference, average temperature, pressure head, and average pressure between the hot end and the cold end of the channel, respectively; a, b, and l are the channel width, depth, and length, respectively (if $a<<b$, the hydraulic diameter $\approx a$); m is the mass of the gas molecule; k_B is the Boltzmann constant; and Q_T and Q_P are the thermal creep and viscous flow coefficients, respectively, numerically provided by Sharipov [Sha99]. The pressure head ΔP reaches its maximum value, *i.e.*, blocking pressure (ΔP_{eq}), when the flow rate is reduced to zero. Therefore, it can be derived from eqn (7.1) that

$$\Delta P_{eq} = \frac{Q_T}{Q_P} \frac{P_{avg}}{T_{avg}} \Delta T \tag{7.2}$$

As shown by eqn (7.1) and eqn (7.2), the performance of Knudsen pumps is determined by ΔT, which is limited by the tolerable stress of the pump structure. The upper limit of temperature is also constrained by the materials used, such as the polymer membrane that is used in some Knudsen pumps [Gup11]. If the thermal conductance of the narrow channels in the membrane is

not sufficiently small, the input power to the hot end can also heat the cold end, and consequently the entire structure. Therefore, heat sinks are typically needed at the cold end of the narrow channels.

Our group has reported two versions of Si-microfabricated high-flow Knudsen pumps recently [An14, An15]. These are single stage pumps that can provide a maximum flow rate of ≈90 sccm at atmospheric pressure. An array of these pumps connected in parallel can provide >200 sccm flow rate. However, the maximum pressure head, *i.e.,* blocking pressure as measured when flow rate is reduced to zero, is <0.4 kPa [An15]. The small pressure head limits the applications of these pumps, as a moderate flow resistance in the flow system can severely load the pump and reduce the flow rate.

To address the challenge of inadequate pressure head, two methods are investigated in this chapter to configure these pumps into multi-stage pumps. Several multi-stage micropump architectures have been reported in the past. In monolithic architectures, multiple stages are integrated side-by-side with fluidic connections on the same chip [Kim15, Son13]. In stacked architectures, multiple chips are arranged vertically, with through-chip fluidic connections that are aligned during assembly [San15]. In planar arrayed architectures, multiple chips are arranged side-by-side on a motherboard; fluidic connections are typically provided by external tubes [Liu11]. Whereas the monolithic architectures provide the greatest compactness, the parasitic flow resistance of the on-chip fluidic connections can be prohibitively large. This becomes a significant concern when each pump stage provides a high flow but only a moderate pressure head. Additionally, heat dissipation can be a challenge. In contrast, stacked architectures, which are inherently three-dimensional arrangement, require smaller footprints than the monolithic architectures. The parasitic flow resistance is also lower, as the fluidic connections are provided

by channels with larger diameters. However, the heat dissipation is exacerbated to some extent. The planar arrayed architectures require larger footprints and volumes than the other two architectures. However, the heat dissipation challenge is significantly mitigated. The parasitic flow resistance can also be reduced if the fluidic connections are provided by external tubes of sufficient diameter. However, these tubes can contribute to extra dead volume, which can delay the pump responses.

This paper describes a quantitative assessment and comparison of the stacked and planar arrayed architectures for series-connected arrays of fully microfabricated Knudsen pumps with the highest flow rates that have been reported to date. As noted previously, the goal is to determine the highest blocking pressures that can be achieved, for applications to complex microanalytical systems such as gas chromatographs. For Knudsen pumps, the stacked architecture has not been demonstrated before. As Knudsen pumps are thermally actuated, thermal management in the stacked architecture is critical. The temperature distribution in the stacked architecture is modeled computationally. The performance of the stacked pumps are experimentally evaluated. The planar arrayed architecture is evaluated, to provide reference points. The design and modeling results are described in Section 6.2, fabrication and assembly in Section 6.3, the experimental results in Section 6.4, and discussions and conclusions in Section 6.5.

6.2. Device Structure and Modeling Results

The single-stage Si-microfabricated high-flow Knudsen pumps are built monolithically on silicon-on-insulator (SOI) wafer (Fig. 6.1). Dense arrays of rectangular narrow channels, each having a 2 μm hydraulic diameter and 20 μm length, are created through the SOI device layer. These narrow channels provide thermal transpiration flow through the wafer. The narrow channel

sidewalls are made of a 10 nm-thick Al_2O_3 layer. Thin dielectric sidewalls are intended to reduce heat conduction along the channels. The temperature gradient for thermal transpiration is provided by integrated heaters and heat sinks. The heaters are formed by a patterned Cr/Pt layer (25/100 nm), which is supported by a stack of two Si oxide-nitride-oxide (ONO) membranes (of total thickness ≈3 μm) on the upper surface of the wafer above the narrow channel arrays. The openings in the ONO layer permit the gas flow to exit the narrow channels. The heat sinks, created in the 380 μm-thick SOI handle layer, are patterned into Si grids that provide wide flow paths. These wide channels maintain incoming gas flow in the viscous regime until it is drawn into the narrow thermal transpiration channels. In this work, each single-stage pump has a pumping area of 4x6 mm^2. The pumping area is laterally surrounded by a 0.36 mm-wide thermal isolation zone, which is comprised of the narrow channels arrays covered by the ONO layer that blocks the flow. The thermal isolation zone is surrounded by the outer substrate rim, which can be attached to a thermal ground. In this chapter, the outlet stage of the multi-stage Knudsen pumps is defined as Stage 1.

To configure a stacked pump, these single-stage pumps cannot be directly aligned and stacked one on top of another. If directly stacked, the heater of the lower stage would be in contact with the heat sink of the upper stage. Hence, the power supplied to the heater of the lower stage would directly heat the heat sink of the upper stage, and consequently the entire stacked structure because of the high thermal conductance of the Si heat sink. Therefore, spacers are required between the stages. In this work, the spacers are micromachined Si frames form-fitted to the single-stage pumps. The high thermal conductance of the Si spacers thermally connects the outer substrate rims of all the upper stages to that of the lowest stage, which is attached to a thermal ground at room temperature. The opening in the center of the spacer is marginally larger than the thermal isolation zone, providing a minimally resistive gas flow path between the stacked stages.

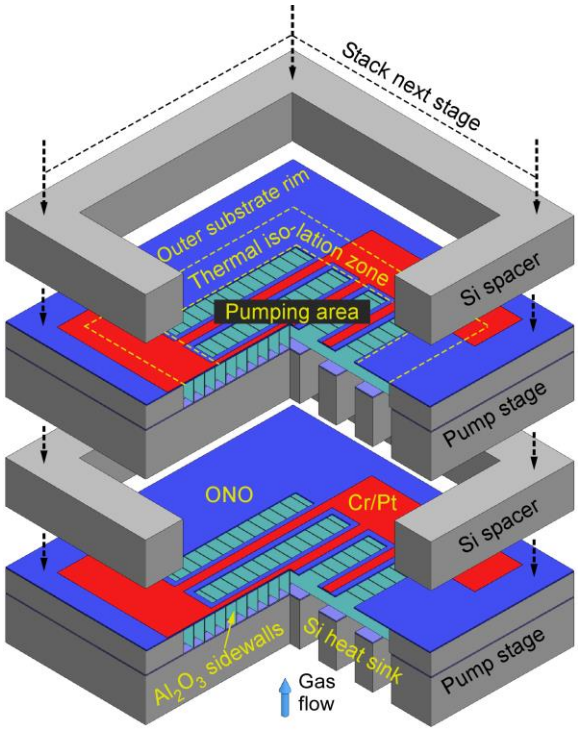

Fig. 6.1: The 3D structural concept of the stacking of Knudsen pumps with spacers.

The thermal response of the single-stage and stacked 4-stage Knudsen pumps was modeled using finite element analysis (FEA). The temperature distribution in the single-stage pump is shown in Fig. 6.2a. It was assumed that 4.8 W power was applied to the pumping area (*i.e.*, 0.2 W/mm^2). The bottom of the outer substrate rim was assumed to be at 295 K. The upper surface of the pumping area was assumed to have natural convection. The heat transfer within the structure was assumed to be dominated by conduction. Under these conditions, the temperature in the center of the pumping area is highest, and decreases near the thermal isolation zone closer to the perimeter (Fig. 6.2a) The temperatures along the hot side and cold side of the narrow channel arrays are plotted in Fig. 6.2b. The ΔT reaches 90 K in the center of the pumping area, and rapidly drops to almost zero in the thermal isolation zone. Without the thermal isolation zone, the ΔT drops to zero at the edge of the pumping area, which would significantly compromises the performance.

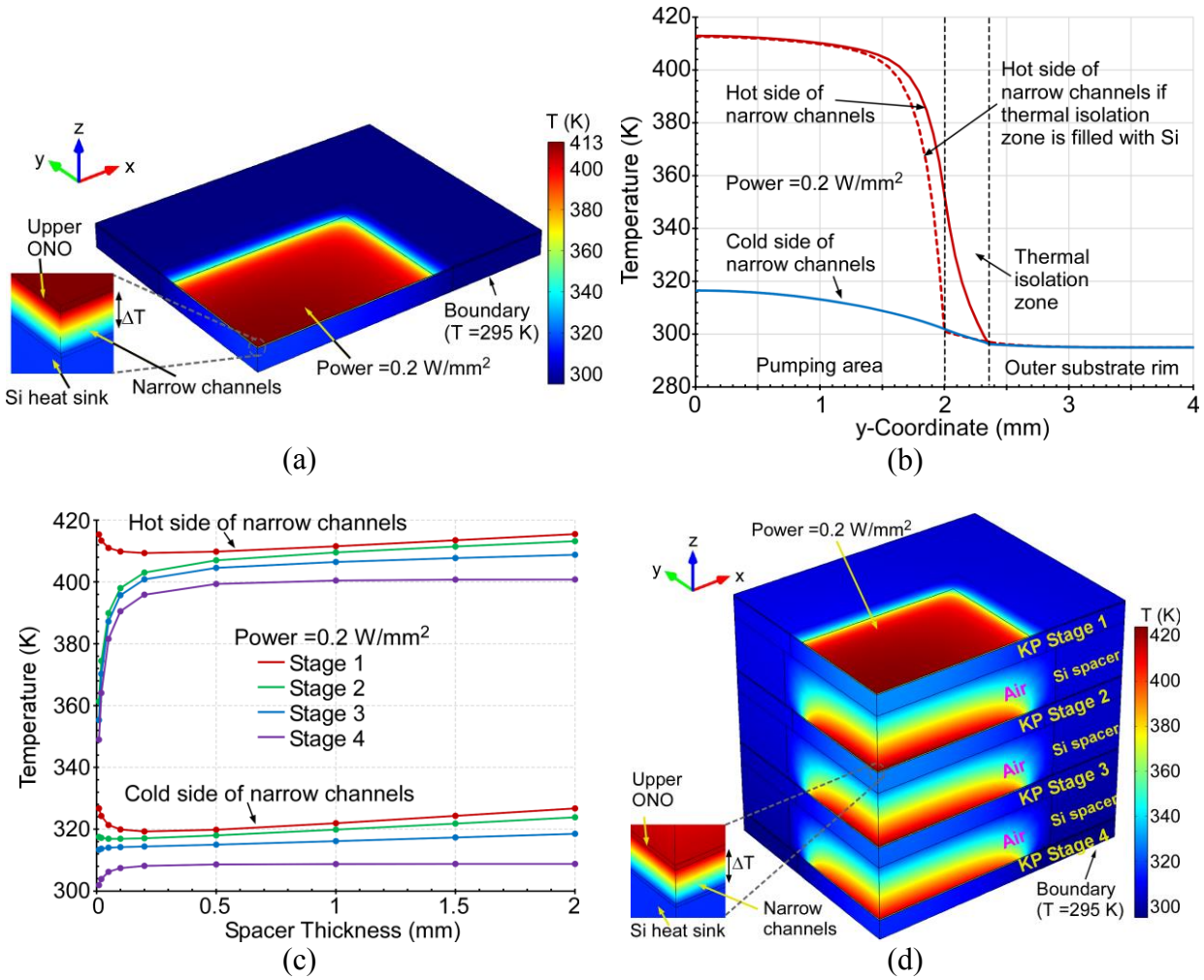

Fig. 6.2: Modeling of the Knudsen pump using FEA. (a) Temperature distribution in a single-sage pump. (b) Temperatures on the hot side and cold side of narrow channels. (c) Average temperatures on the hot and cold sides of the narrow channels in a stacked 4-stage pump with varying spacer thickness. (d) Temperature distribution in the stack with spacer thickness of 1 mm.

For the stacked architecture, the effect of the spacer thickness on the temperature distribution was also studied. The results of an analysis of a 4-stage stack are shown in Fig. 6.2c and d. It was assumed that the power applied to each stage was 4.8 W, *i.e.*, 0.2 W/mm^2 of pumping area. The outer substrate rim of the lowest stage (Stage 4) in the stack was assumed to be at 295 K. The upper surface of the pumping area of the highest stage (Stage 1) was assumed to have natural convection. It was assumed that heat transfer within the stack is dominated by conduction at these small scales. The average temperature on the hot side and cold side of each stage of narrow

channels is plotted in Fig. 6.2c, as a function of spacer thickness. It is evident from this plot that when the spacer thickness exceeds 0.2 mm, the temperature on the hot side of the narrow channels in each stage is ≈90°C higher than that on the cold side. However, when the spacer thickness drops below 0.2 mm, the temperatures on the hot sides of the narrow channels decrease with spacer thickness in all stages except the highest one. This is because the heat conduction through the air gap between the heater of the lower stage and the Si heat sink of the upper stage becomes significant. Therefore, a minimum spacer thickness of 0.2 mm is preferred. However, considering the ease of fabrication and assembly, which are discussed in the following paragraphs, a spacer thickness of 1 mm is selected. The temperature distribution in the stack for this value is shown in Fig. 6.2d. The temperature in the center of the pumping area is highest, reduces near the thermal isolation zone. Vertically, the highest stage has ≈10 K higher temperature than the lowest stage. This value can be reduced if necessary by reducing the pumping area or increasing the width of the outer rim.

6.3. Fabrication and Assembly

The single-stage pumps were microfabricated using a 4-mask process in a single SOI wafer. The narrow channel arrays were created by deep reactive ion etching (DRIE) through the SOI device layer (Fig. 6.3a). The sidewalls of these narrow channels were formed by atomic layer deposition (ALD) of 10 nm-thick Al_2O_3 (Fig. 6.3b). Then the narrow channels were filled with sacrificial polySi using low-pressure chemical vapor deposition (LPCVD) (Fig. 6.3c). The ONO membrane and the Cr/Pt heaters were deposited by plasma-enhanced chemical vapor deposition (PECVD) and e-beam evaporation, respectively (Fig. 6.3d). The Si heat sinks were created by

DRIE through the SOI handle layer (Fig. 6.3e). Finally, after wafer dicing, the sacrificial polySi and remaining Si in the narrow channels were etched by XeF_2 dry gas.

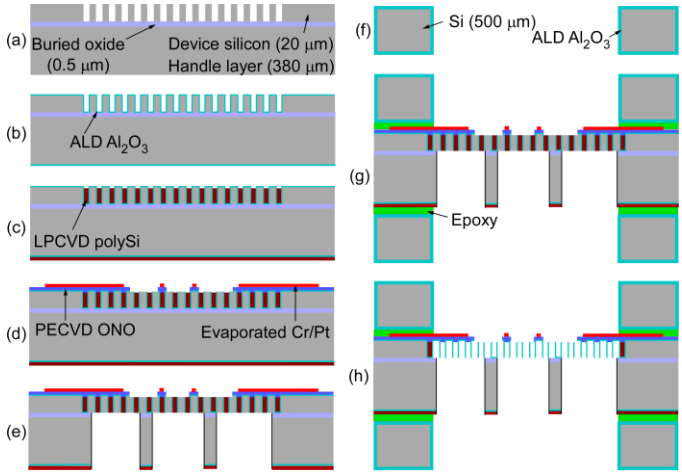

Fig. 6.3: Illustration of the fabrication process for the Knudsen pump stages. (a) DRIE through SOI device Si layer. (b) ALD Al_2O_3. (c) Narrow channel refilled by sacrificial poly-Si. (d) Deposit and pattern upper ONO membrane and Cr/Pt heater. (e) DRIE through SOI handle layer. (f) Spacer fabrication: DRIE through Si and ALD Al_2O_3. (g) Attach spacers to pump stages with epoxy. (h) XeF_2 etch of Si and polySi in narrow channels.

The Si spacers for the stacked pumps were microfabricated using a 1-mask process, in which the 500 μm-thick Si wafers are etched through by DRIE (Fig. 6.3f). The layout for this step was designed such that all the Si spacers are singulated from the wafer after DRIE without requiring additional dicing. Subsequently, the spacers were coated with a 20 nm-thick Al_2O_3 layer on all surfaces. This layer was optional and precautionary, serving two purposes. First, it allowed the spacers to be attached to the pump stages before the final XeF_2 etch of the Si and polySi in the narrow channels; the Al_2O_3 layer protected the spacers from the XeF_2 gas. Second, the Al_2O_3 layer electrically isolated the spacers, blocking stray current that might heat the spacers.

The multiple stages of the stacked pumps were attached to each other by adhesion layers. First, two spacers were bonded to a pump stage, one on each side (Fig. 6.3g), using permanent epoxy (Epotek-377, Epoxy Technology Inc., MA). After XeF_2 etch of the sacrificial Si and polySi (Fig. 6.3h), the pump stages were stacked and bonded to each other using a removable wax layer

(QuickStick™ 135, Electron Microscopy Science, PA). This permitted replacement or reconfiguration of the pump stages. After stacking, the distance between two pump stages was 1 mm, created by two 500 µm-thick spacers.

For testing, wires were attached to the lead pads of the Cr/Pt heaters using a conductive epoxy. The stacked pumps were mounted on a perforated Al plate that served as an external heat sink; the perforations permitted gas flow into the pumps. For the planar arrayed pump architecture, a tube fitting was attached to the outlet on top of each stage to permit a tube connection to the next stage. The photograph of a 4-stage stacked architecture, which has a form factor of 10x8x6 mm^3, is shown in Fig. 6.4a. The photograph of a 4-stage planar arrayed pump is shown in Fig. 6.4b.

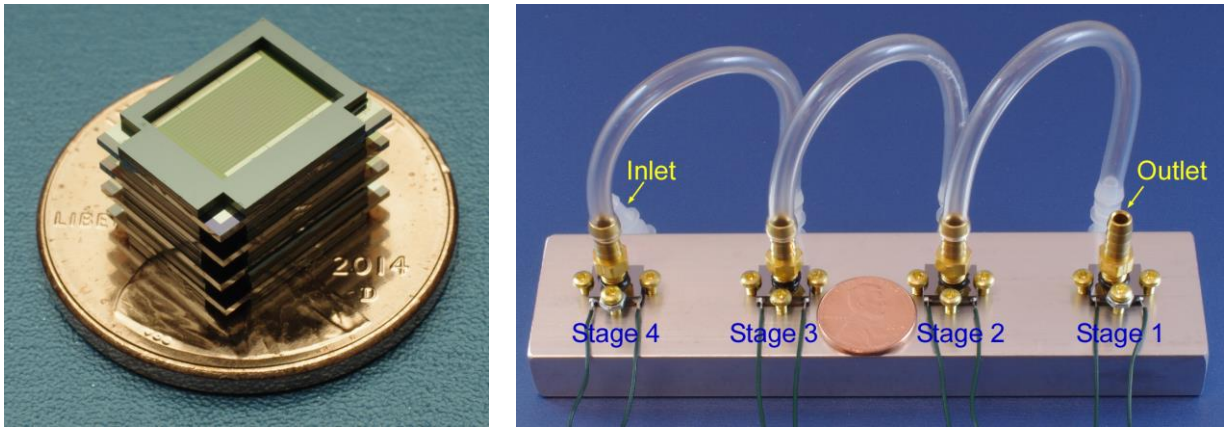

(a) (b)

Fig. 6.4: Photographs of the fabricated multi-stage Knudsen pumps. (a) A 4-stage stacked Knudsen pump. (b) A 4-stage Knudsen pump connected by Tygon tubes.

6.4. Experimental Results

To experimentally evaluate the multi-stage Knudsen pumps, the device under test (DUT) was used to evacuate room air from a glass bottle of 2.5 L fixed volume (Fig. 6.5). A commercial differential pressure sensor (MPX5010DP, Freescale Semiconductor Inc, TX) continuously measured the pressure difference (ΔP) between the inlet of the DUT and the outlet, which was open to the ambient pressure (P_o). A solenoid valve was connected to the DUT inlet to reset the

pressure. These components were placed in a vacuum chamber that was used to control the ambient pressure for the DUT. Electrical feedthroughs in the vacuum chamber wall allowed electronic control and readout through a data acquisition board (NI USB-6259, National Instruments, TX) and a LabVIEW™ program.

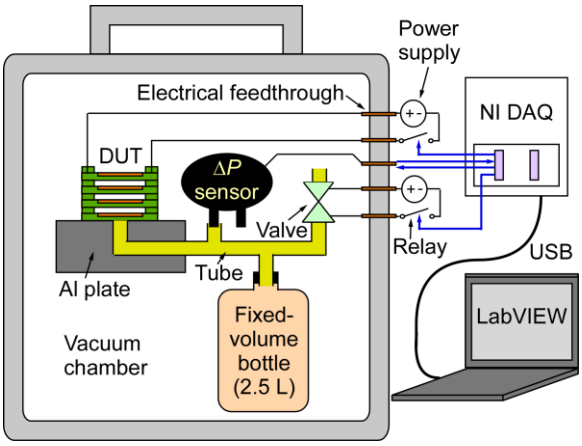

Fig. 6.5: Test setup for evaluating the performance of the Knudsen pumps.

Even under the ideal condition, an *n*-stage Knudsen pump cannot provide more than *n*-fold increase in blocking pressure compared to a single-stage Knudsen pump. Further, this will require an *n*-fold increase in power (keeping the same power density for each stage), and the maximum possible flow rate (Q_{max}) will be the same as that for a single-stage pump. Mathematically, $\Delta P_{eq} = \Delta P|_{Q=0}$, and $Q_{max} = Q|_{\Delta P=0}$. This trend was evident in the experimental results of the stacked and planar array.

For the stacked architecture, while operating in an air ambient at atmospheric pressure (Fig. 6.6a) of 100 kPa (760 Torr) with an average power of 2 W per stage, the stacked 1-stage, 2-stage, and 4-stage pumps provided blocking pressures of 0.070 kPa, 0.135 kPa, and 0.255 kPa. The flow rates (Q) were calculated from the ΔP using the following equation derived from the ideal gas law:

$$Q = \frac{M_{air}}{\rho_{std}} \frac{V}{R \cdot T_{amb}} \frac{\mathrm{d}\Delta P}{\mathrm{d}t} \tag{7.3}$$

where M_{air} is the molar mass of air; ρ_{std} is the air density at standard conditions; V is the volume being evacuated; R is the universal gas constant, T_{amb} is the ambient temperature, $\frac{\mathrm{d}\Delta P}{\mathrm{d}t}$ is the changing rate of ΔP.

The maximum flow rates for the stacked 1-stage, 2-stage, and 4-stage pumps were 30 sccm, 33.5 sccm, and 27 sccm, respectively, at 2 W per stage. Hence, the ratio of the blocking pressures was 1:1.9:3.6, whereas the ratio of the maximum flow rates was 1:1.1:0.9. A similar trend was evident when the pumps were operated at an ambient pressure of 27 kPa (200 Torr) (Fig. 6.6b), which is of interest for certain applications such as gas chromatographs. The stacked 1-stage, 2-stage, and 4-stage pumps provided blocking pressures of 0.15 kPa, 0.30 kPa, and 0.55 kPa, and maximum flow rates of 17.5 sccm, 21 sccm, and 15 sccm, respectively, at 2 W per stage. The ratio of the blocking pressures was 1:2:3.7, whereas the ratio of the maximum flow rates was 1:1.2:0.9. The deviation of these ratios from the hypothetical ideal ratios, *i.e.*, 1:2:4 for blocking pressure and 1:1:1 for maximum flow rate, was relatively modest. Possible contributing factors are discussed in the next section.

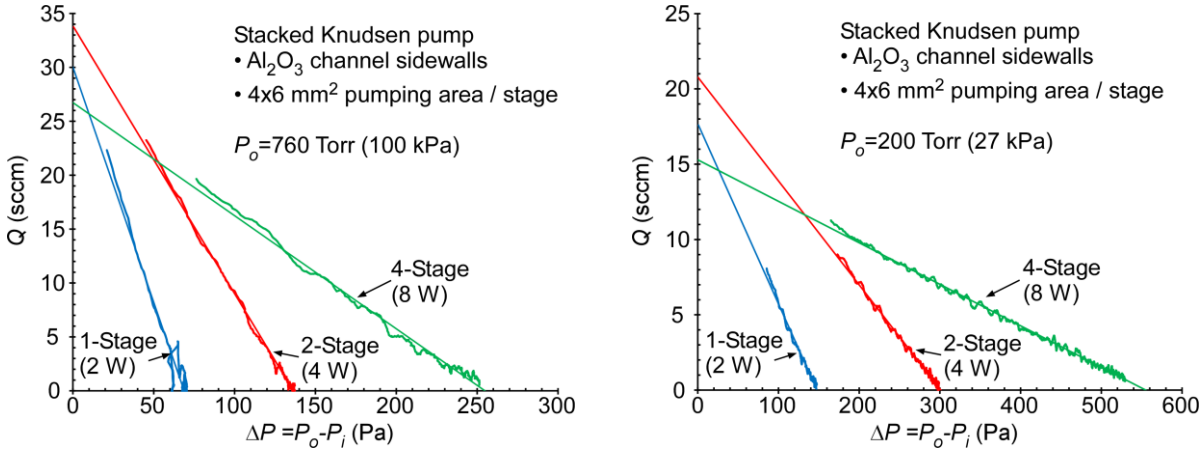

Fig. 6.6: Performance of the stacked Knudsen pumps at (a) atmospheric pressure and (b) 200 Torr ambient pressure.

The planar arrayed pumps were also evaluated in air at atmospheric pressure 100 kPa (760 Torr) with an average power of 2 W per stage (Fig. 6.7a). The planar arrayed 1-stage, 2-stage, and 4-stage pumps provided blocking pressures of 0.065 kPa, 0.120 kPa, and 0.250 kPa, and maximum flow rates of 31 sccm, 31 sccm, and 33 sccm, respectively. The ratio of the blocking pressures was 1:1.8:3.8, whereas the ratio of the maximum flow rates was 1:1:1.1.

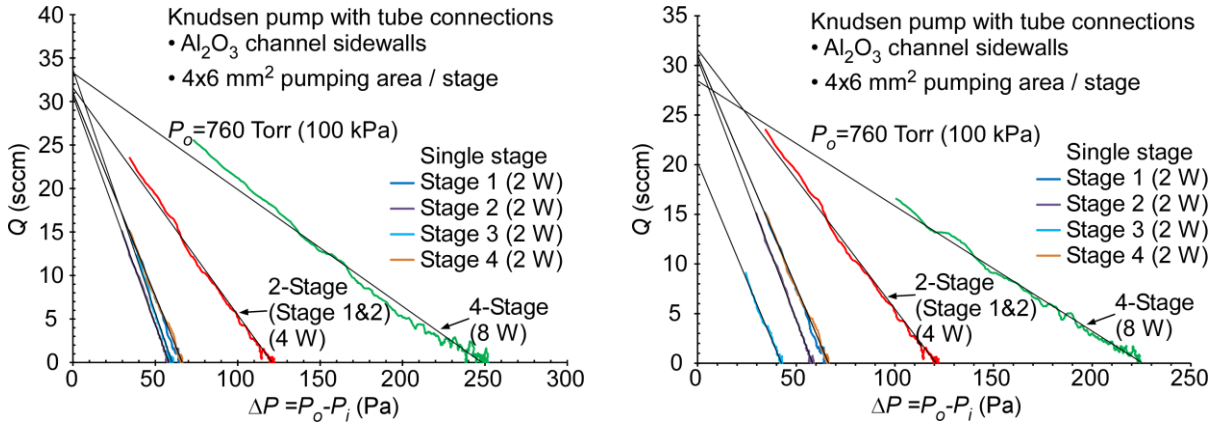

Fig. 6.7: Performance of the multi-stage Knudsen pumps with tube connections at atmospheric pressure. (a) A 4-stage pump in which all the stages performed similarly. (b) A 4-stage pump in which one stage provided lower performance than the other three stages.

To study the effect of the stage-to-stage variation upon the overall performance of the multi-stage Knudsen pump, a trial 4-stage planar arrayed pump was configured, in which one of the stages (Stage 3) was replaced with a trial stage that provided lower performance than the other stages (Fig. 6.7b). When operated in air at atmospheric pressure with an average power of 2 W per stage, the blocking pressure of the trial pump was smaller than that of the normal pump by ≈0.025 kPa, which was approximately equal to the blocking pressure difference between the trial stage and the normal stages. The maximum flow rate of the trial pump was smaller than that of the normal pump by ≈5 sccm, which was less than the maximum flow rate difference between the trial stage and the normal stages.

The performance of both types of arrays increased with power (Fig. 6.8). For the stacked 4-stage pumps at atmospheric pressure, when the total power increased from 1 W to 8 W, the blocking pressure increased from 0.03 kPa to 0.255 kPa, whereas the maximum flow rate increased from 4 sccm to 27 sccm (Fig. 6.8a). For the planar arrayed 4-stage pumps at 27 kPa (200 Torr) ambient pressure, when the total power increased from 8 W to 12 W, the blocking pressure increased from 0.595 kPa to 0.88 kPa, whereas the maximum flow rate was increased from 20.5 sccm to 27.5 sccm (Fig. 6.8b).

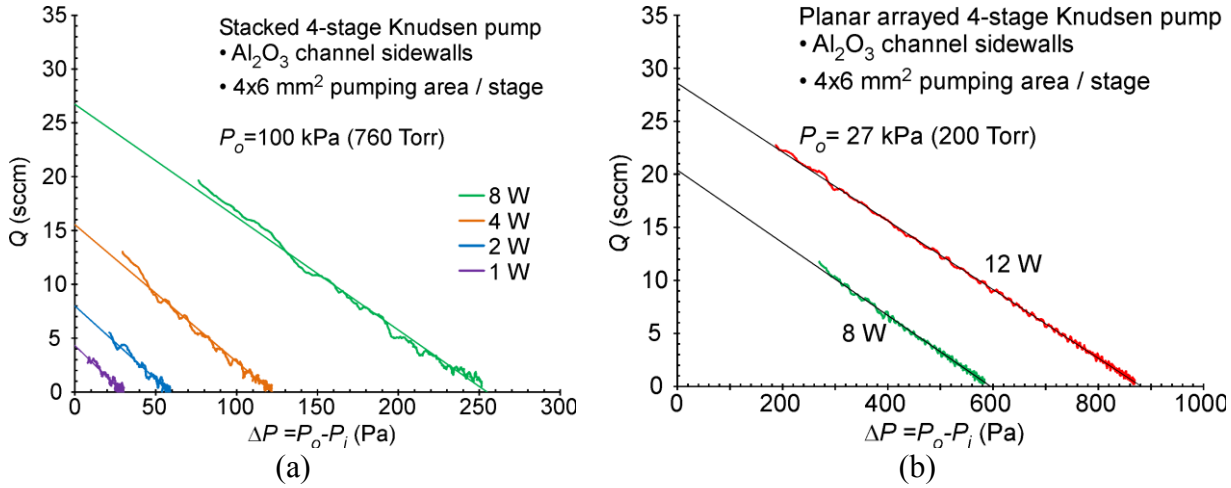

Fig. 6.8: Performance of the 4-stage Knudsen pumps with varying powers. (a) Stacked pump at atmospheric pressure. (b) Planar arrayed pump at 27 kP (200 Torr) ambient pressure.

6.5. Discussion and Conclusion

The experimental results have validated the benefits of series-connected high-flow Knudsen pumps, *i.e.*, a higher pressure head. Compared to a single-stage pump, the 4-stage pumps in both the stacked and planar arrayed architectures have shown nearly 4x blocking pressure while maintaining similar flow rates. The blocking pressure provided by the 4-stage pumps reaches ≈0.9 kPa (Fig. 6.8), which is twice as high as the previously reported data for this type of Knudsen pump [An15]. This blocking pressure is achieved by distributing 12 W into 4 stages, providing a ΔT of ≈56 K in each stage as calculated from the modeling results (Fig. 6.2). If this blocking

pressure is attempted by a single-stage pump, the entire 12 W would need to be applied to a single stage to provide a ΔT of ≈225 K, which could be excessively high and cause damage to the pump structure due to the thermal stress.

Although both the stacked and planar arrayed architectures described in this paper have shown desired performance, different application scenarios are envisioned. The stacked architecture is appropriate for a compact assembly of a small quantity of stages that operate at a relatively low power. From the modeling results (Fig. 6.2), it is evident that the upper stages have higher temperatures than the lower stages. With a stack of a few stages providing >10 sccm flow and sub-kP pressure, such pumps can potentially be used for rapid vapor sampling for various analytical instruments. The planar arrayed architecture is amenable for integrating more stages operating at higher power, if the form factor is not a concern. With a higher pressure head of >1 kPa, the pumps can potentially be used to drive vapor separation in gas chromatographs. As these Knudsen pumps have shown higher performance at a pressure level of ≈27 kPa (200 Torr) than at atmospheric pressure, they can be used in tandem with a roughing pump to enhance the performance.

While the major benefit of Knudsen pump lies in its reliability or lifetime as compared to the membrane-actuation-based micropumps, another level of this benefit is also notable. In a multi-stage Knudsen pump, where no active valve is used, the failure of one stage can degrade the overall performance but the pump can still be functional. Specifically, the overall blocking pressure becomes the aggregate of the remaining stages, whereas the overall flow rate is slightly reduced as the failed stage becomes a flow resistance for the remaining stages. This effect has been observed in the experiments. Nevertheless, the pumps remain functional, because the fluidic

connections in multi-stage Knudsen pumps are directly provided by channels without active valve, which can completely block the gas flow path upon failure.

In conclusion, this chapter reports a stacked architecture and a planar arrayed architecture for configuring multi-stage high-flow Knudsen pumps. Both architectures have shown experimental results that are improved compared to a single-stage pump. The pressure head and flow can be scaled by the number of stages and the pumping area, respectively. With proper scaling, these performance metrics can reach the values appropriate for practical microsystems such as micro gas chromatographs. Future challenges include proper scaling of the performance for specific applications, and packaging of the pumps with improved thermal management.

Chapter 7:

Conclusions and Future Work

7.1. Conclusions

This PhD thesis describes research directed at the integration of fully microfabricated gas chromatography systems. The integrated μGC systems, each contributing to certain aspects that are essential to the ultimate goal of a low-cost, fully microfabricated system. In addition, the pathway to achieving very high performance micropumps was identified; micropumps are key components of μGC systems.

The *iGC1* system shows the feasibility of using a standardized fabrication approach to manufacture a fluidic microsystem for gas chromatography, including a pump, a preconcentrator, a separation column and a detector. The three-mask fabrication process is low cost and standardized, showing promise of wider adoption of μGC technology. The *iGC1* system architecture also demonstrates that a Knudsen pump using nanoporous media assembled with microfabricated dice can be form-fitted with the other μGC components. All the components can be arranged in the form of a 4-cm^3 stack, achieving a compact integration. The experimental results demonstrate basic operation of the system.

The *iGC2* system shows the functionality of a valveless μGC architecture that utilizes a bi-directional micropump with a two-stage preconcentrator. This architecture provides bi-directional gas flow through the system, which is critical for the (multi-stage) preconcentrator. This architecture provides an approach to avoid using valves, which are difficult and costly to

microfabricate, and instead creates bi-directional flow using a bi-directional Knudsen pump. The experimental results demonstrate possibilities to perform quantitative analysis.

The *iGC3* system replaces the microdischarge-based detectors in the previous two systems with capacitive detectors. This approach achieves a system in which all the components can be microfabricated by the same three-mask process and interfaced purely by electronic circuitry. Additionally, the system can use room air as the carrier gas, without relying upon external carrier gas supplies. The system demonstrates analysis of 19 chemicals, most of which are common indoor VOCs, with ppm-ppb concentrations. The experimental results show promises of the system performing automated continuous monitoring of indoor air pollutants.

As the high-flow micro gas pump is an important μGC component, this PhD thesis also contributes to the advancement of a type of motionless gas pump, *i.e.*, the Knudsen pump. In the *iGC* systems described, the Knudsen pumps all use nanoporous MCE membranes with integrated microfabricated glass dice. For this pump, however, lithographic Si-micromachining is used to create through-wafer narrow channel arrays to provide thermal transpiration. This approach monolithically integrates heaters, heat sinks, and narrow channel arrays, which minimize the defect-induced leakage compared to using the MCE membranes. The Si-micromachined Knudsen pumps demonstrate over 200 sccm flow rate and three orders of magnitude higher flow rate per unit pumping area than the MCE-based Knudsen pumps.

Finally, architectures for configuring multi-stage Si-micromachined high-flow Knudsen pumps are studied. In the primary architecture, the single-stage Si-micromachined high-flow Knudsen pumps are stacked with Si-micromachined spacers to form multi-stage pumps. Another architecture that arranges the single-stage pumps in a planar array. Both architectures experimentally demonstrate that the pressure head of the single-stage pumps can be multiplied by

the number of stages, while the flow rate can be maintained by the multi-stage pumps. The results show promises of tailoring the Si-micromachined high-flow Knudsen pumps for various practical applications including μGCs.

7.2. Future Work

The ultimate goal of the *iGC* systems is to realize wide deployment in various end-user applications. Several device improvements need to be accomplished. First, the entire *iGC3* system can be further miniaturized. For example, the current two-stage bi-directional Knudsen pump can be reduced to a single-stage pump, which is properly designed and configured to provide comparable performance. Second, thermoelectric coolers can be integrated with various components, to tailor the *iGC3* system for certain applications where light chemicals are of interest. Additionally, electronic circuitry and packaging for the system merit further investigation. Comprehensive evaluation of the systems with varying environmental parameters (such as ambient pressure, temperature, humidity, and dustiness) is also required.

For the Si-micromachined high flow Knudsen pumps, another approach for multi-stage integration can be explored. In this potential approach, the multi-stage pump is redesigned to integrate both the narrow channel arrays and the wide channels in the same plane (Fig. 7.1b). Fluidic connection of the stages is provided by on-chip channels that are formed by bonding micromachined wafers. This approach provides a highly compact integration, which permits more stages than the current chip-stacking approach, and hence is expected to provide higher performance.

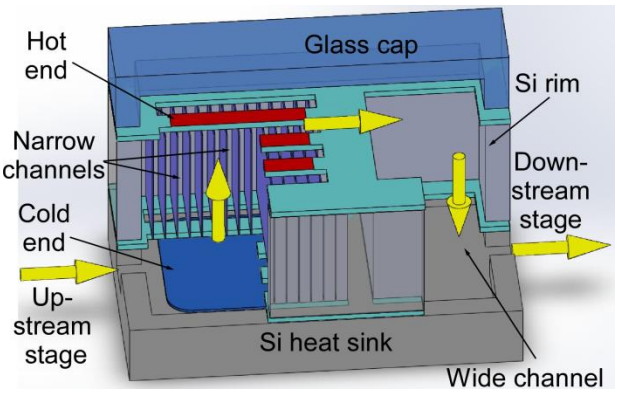

Fig. 7.1: Integration of multi-stage Si-micromachined high-flow Knudsen pumps with on-chip gas flow connection channels.

Appendices

Appendix A:

Additional Results on Si-Micromachined High-Flow Knudsen Pumps

This appendix provides additional results of the single-stage Si-micromachined high-flow Knudsen pumps described in Chapter 5 (Pages 92-115). The contents in this appendix are described in the context of Chapter 5, and are directed at the experimental evaluation of performance in vacuum ambients for both the ALD KPs (which use the 10 nm-thick Al_2O_3 as the narrow channel sidewalls) and the ONO KPs (which use the 100 nm-thick ONO as the narrow channel sidewalls).

Chapter 5 describes the test setup of the Knudsen pump operation in a vacuum ambient (Fig. 5.6b). A typical measurement cycle of the Knudsen pump operation in vacuum is shown in Fig. A.1. In this measurement, the vacuum chamber provided 200 Torr ambient pressure for the Knudsen pump KP-1.2, which was used to evacuated a bottle with 150 mL fixed volume. During Period (1), the Knudsen pump was supplied with 0.3 W constant power starting at $t \approx 5$ sec. With the valve (Fig. 5.6b) closed, the Knudsen pump generated a ΔP response, which approached ΔP_{eq} and stabilized in ≈40 sec (Fig. A.1). During Period (2), the valve was opened at $t \approx 50$ sec. for ≈1 sec., during which the ΔP generated during Period (1) was reset to zero. After the valve was closed, the ΔP was built up again. Period (3) was a repetition of Period (2), providing verification of the result. During Period (4), the Knudsen pump power supply was turn off, therefore the ΔP gradually dropped to zero.

The transient flow response can be calculated from the Δ*P* response in either Period (2) or Period (3). As the Knudsen pump has fast response – with <0.5 sec response time as shown in Fig. 5.9 – the Δ*P* response during Period (1) can also be used for this purpose after the Knudsen pump has thermally stabilized. In a typical flow response, the KP-1.2 output air flow rate gradually decreased from 3 sccm to zero, as Δ*P* gradually stabilized (Fig. A.1).

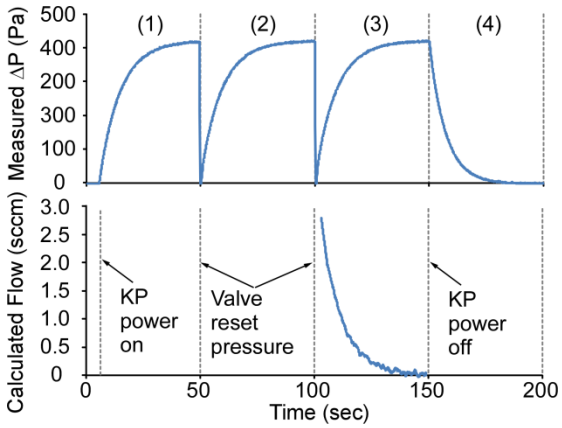

Fig. A.1: An example transient pressure and flow response obtained from the Knudsen pump operation in vacuum. The experiment is divided into four periods – Period (1)-(4).

The resulting *Q*-Δ*P* relationships for the ALD KP-1.2 and ALD KP-24 at 200 Torr (27 kPa) and 70 Torr (9 kPa) ambient pressure with various input power levels are shown in Fig. A.2. For example, the ALD KP-24 operated at 200 Torr ambient pressure with 3 W power provided a maximum flow rate of 25 sccm and a blocking pressure of 0.22 kPa (Fig. A.2c). At an ambient of 70 Torr, the maximum flow rate was 17 sccm and blocking pressure was 0.21 kPa (Fig. A.2d). The performance normalized to the pumping area is shown in Fig. A.3. It is evident that both the flow rate and blocking pressure can be increased by higher power levels. With a given power density, the ALD KP-1.2 provided higher maximum flow rate per unit pumping area and similar blocking pressure as compared to the ALD KP-24. These trends are similar to those shown in Fig. 5.7 and Fig. 5.8.

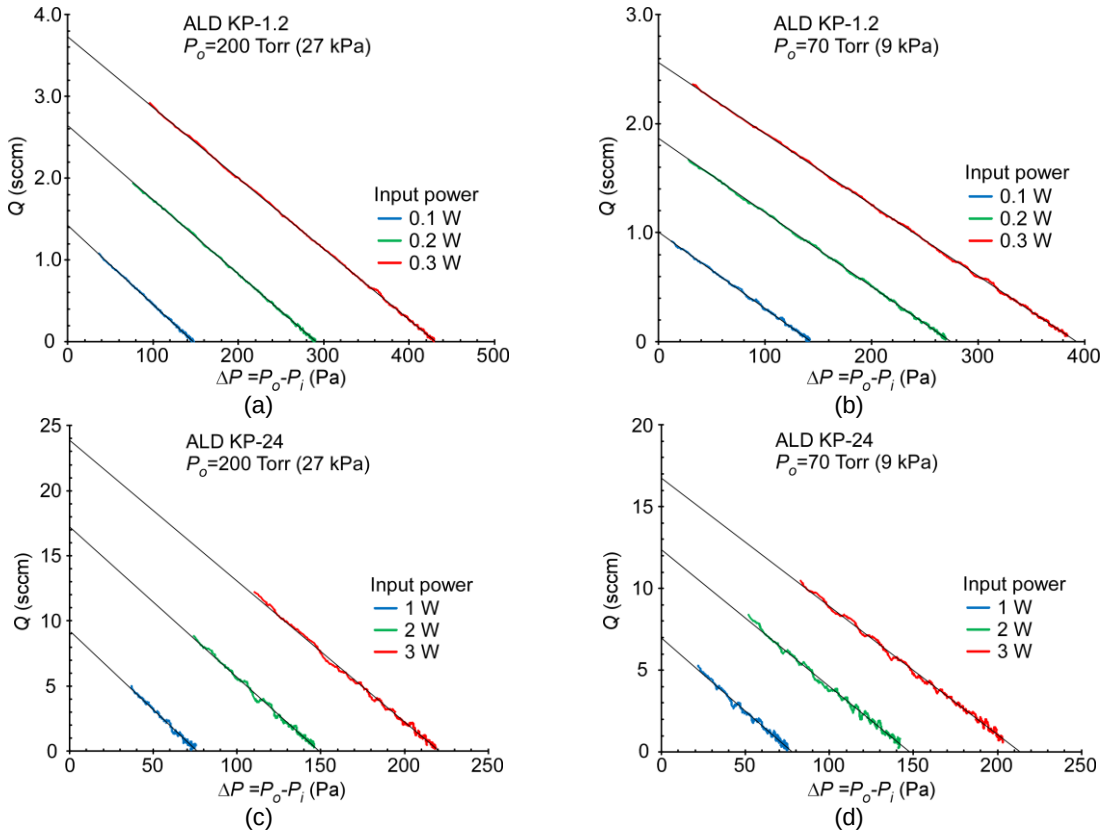

Fig. A.2: Measured Q-ΔP relationships of ALD KPs operated in vacuum with varying input power levels. (a) KP-1.2 at 200 Torr. (b) KP-1.2 at 70 Torr. (c) KP-24 at 200 Torr. (b) KP-24 at 200 Torr.

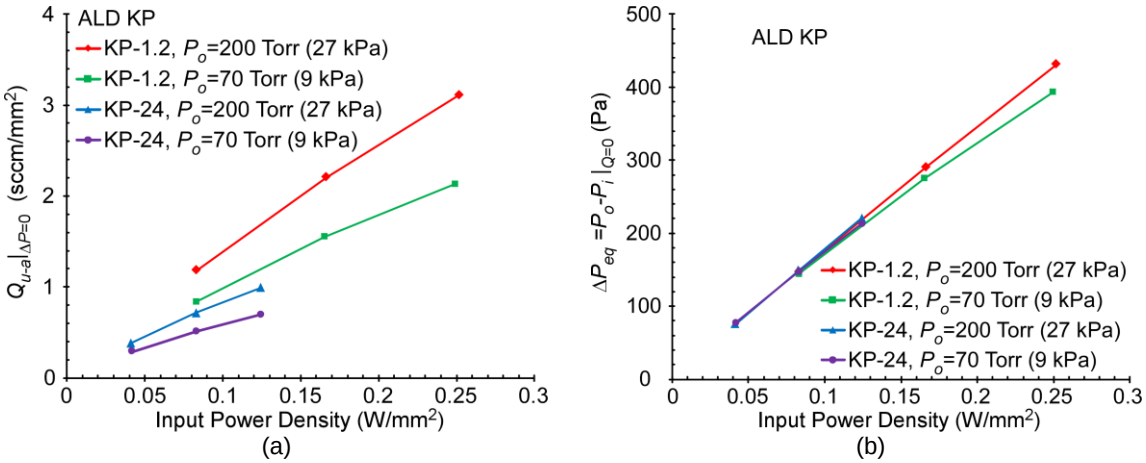

Fig. A.3: Unit-area performance of ALD KPs operated in vacuum. (a) Maximum flow rate per unit pumping area and (b) blocking pressure at different input power densities.

The performance of ONO KPs (*i.e.*, Knudsen pumps with 100 nm-thick ONO sidewalls) is shown in Fig. A.4-Fig. A.5. For example, the ONO KP-96 provided a maximum flow rate of 60

sccm and a blocking pressure of 0.1 kPa, when operated at atmospheric pressure with 25 W power (Fig. A.4c). When operated in vacuum ambient, the ONO KPs show trends that are similar to the ALD KPs, *i.e.*, the maximum flow rate provided by the Knudsen pumps increases with increasing ambient pressure, whereas the blocking pressure reaches maximum at 200 Torr ambient pressure (Fig. A.5). The lower performance of the ONO KPs (Fig. 5.8), as compared to that of the ALD KPs, is likely caused by the non-ideal fabricated structures (*i.e.*, overhanging beams, Fig. A.6) and the 100 nm-thick ONO layer, which allows higher thermal conductance along the walls of the narrow channels between the hot side and the cold side than the 10 nm-thick Al_2O_3 layer.

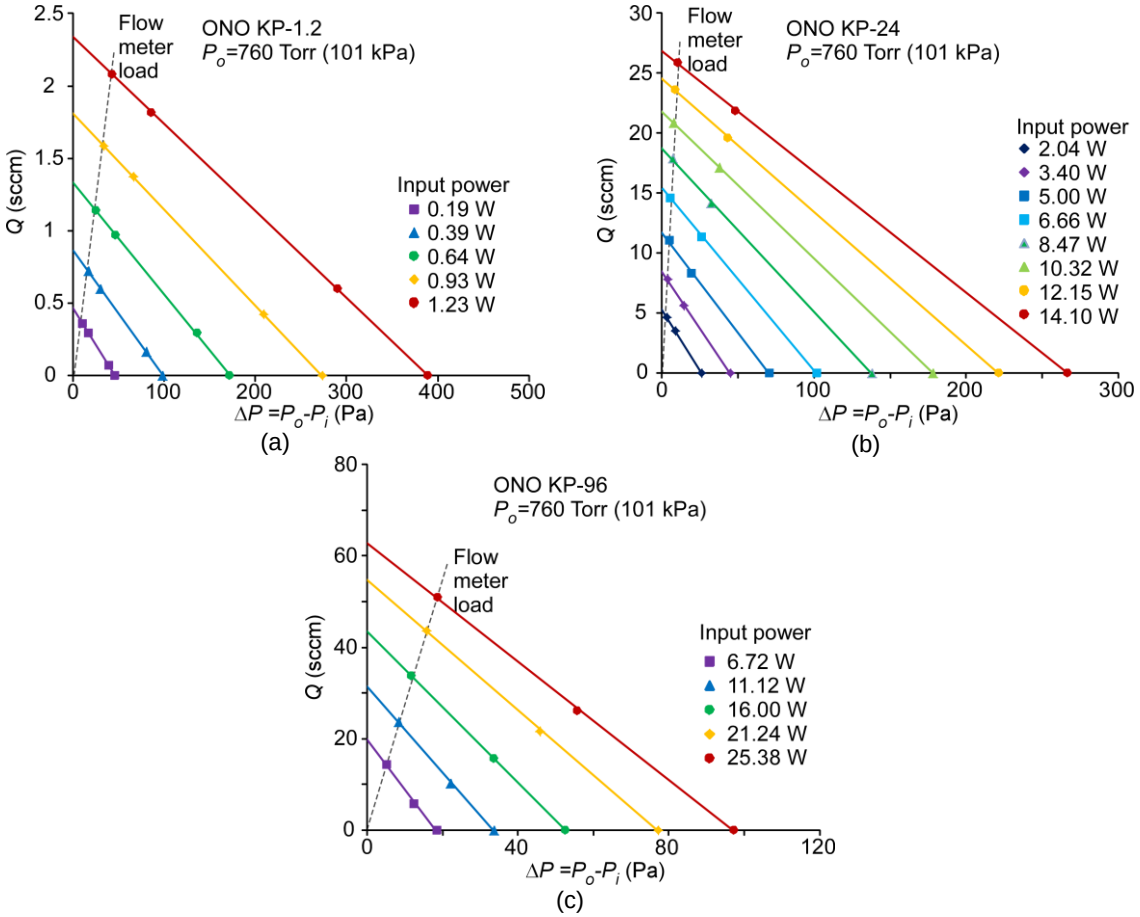

Fig. A.4: Measured Q-ΔP characteristic lines of the ONO KPs at atmospheric pressure with different input power levels: (a) KP-1.2, (b) KP-24, and (c) KP-96.

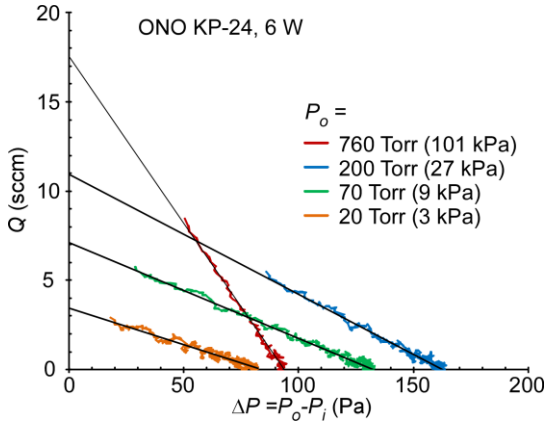

Fig. A.5: Measured Q-ΔP characteristic lines of the ONO KP-24 operated with 6 W power at different ambient pressure levels.

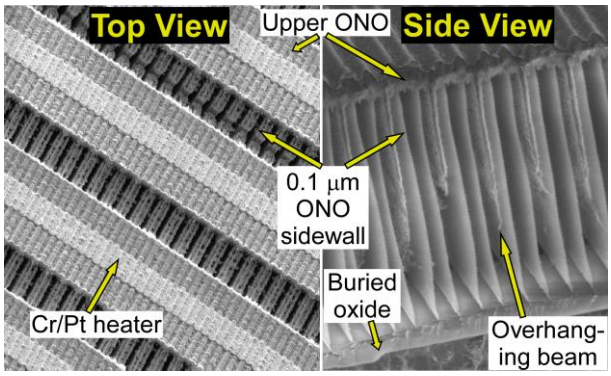

Fig. A.6: SEM image of the ONO KP.

Appendix B:

Supplementary Material of *iGC*

Among the four *iGC* components, *i.e.*, Knudsen pump, preconcentrator, separation column, and detector, only the separation column requires a smooth inner surface, which needs to be coated with the stationary phase. The root-mean-square line roughness of the sandblasted channel is measured to be ≈0.866 μm (Fig. B.1a). This value is larger than the thickness of the stationary phase, which targets an average value of ≈0.2 μm. Therefore, the stationary phase, if directly coated onto the sandblasted surface, could have non-uniform thickness. After spin-coating SU-8 on the sandblasted substrate, the channel is fully covered by SU-8, resulting in a root-mean-square line roughness of 0.013 μm (Fig. B.1b). Therefore, the SU-8 layer not only provides adhesion between the metallized substrate and the sandblasted substrate, but also provides a smooth inner surface of the column facilitating the stationary phase coating.

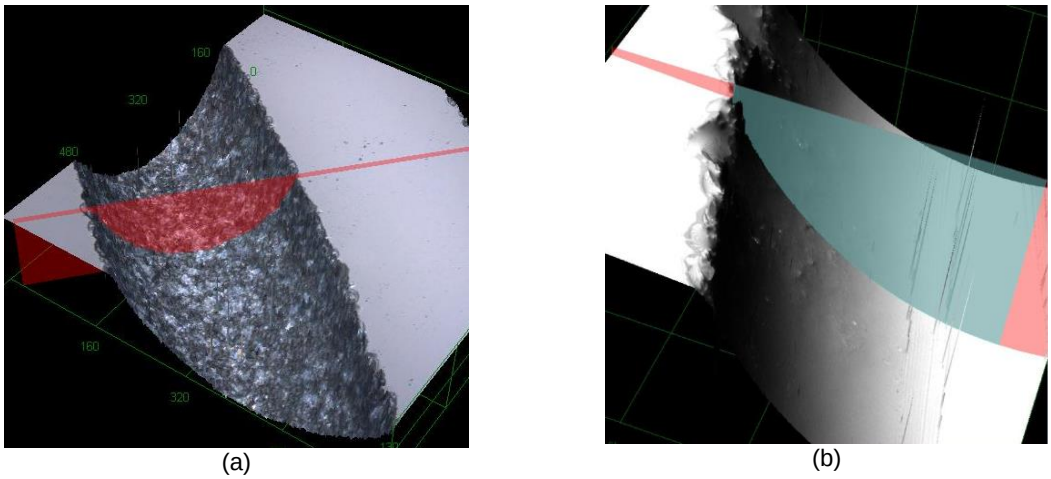

(a) (b)

Fig. B.1: Surface profiles measured by the Olympus LEXT OLS4100 laser scanning digital microscope. (a) A sandblasted channel. (b) A sandblasted channel spin-coated by SU-8.

References

[Ada06] M. Adahchour, J. Beens, R. J. J. Vreuls, and U. A. T. Brinkman, "Recent developments in comprehensive two-dimensional gas chromatography (GC×GC). II. Modulation and detection," *TrAC - Trends in Analytical Chemistry,* vol. 25, no. 6, pp. 540-553, 2006.

[Adk10] D. R. Adkins, "Modular manifold for integrated fluidics and electronics," US Patent 7685864 B1, 2010.

[Adk09] D. R. Adkins and P. R. Lewis, "Compact low-power gas detector for chemical alarms," *SPIE Defense and Security Sensing Conference Proceedings*, Orlando, FL, 2009, p. 73040S (10 pp.).

[Aga05] M. Agah, J. A. Potkay, G. Lambertus, R. Sacks, and K. D. Wise, "High-performance temperature-programmed microfabricated gas chromatography columns," *Journal of Microelectromechanical Systems,* vol. 14, no. 5, pp. 1039-50, 2005.

[Akb15] M. Akbar, H. Shakeel, and M. Agah, "GC-on-chip: integrated column and photoionization detector," *Lab on a Chip,* vol. 15, no. 7, pp. 1748-1758, 2015.

[An14] S. An, N. K. Gupta, and Y. B. Gianchandani, "A Si-Micromachined 162-Stage Two-Part Knudsen Pump for On-Chip Vacuum," *Journal of Microelectromechanical Systems,* vol. 23, no. 2, pp. 406-416, 2014.

[An14] S. An, Y. Qin, and Y. B. Gianchandani, "A monolithic Knudsen pump with 20 sccm flow rate using through-wafer ONO channels," *IEEE International Conference on Micro Electro Mechanical Systems (MEMS)*, San Francisco, 2014, pp. 112-115.

[An15] S. An, Y. Qin, and Y. B. Gianchandani, "A monolithic high-flow Knudsen pump using vertical Al_2O_3 channels in SOI," *Journal of Microelectromechanical Systems,* In press, 2015.

[Bar04] E. F. Barry, "Columns: Packed and Capillary; Column Selection in Gas Chromatography," in *Modern Practice of Gas Chromatography*, eds. R. L. Grob and E. F. Barry, John Wiley & Sons, Inc., 2004, pp. 65-191.

[Bes12] A. Besharatian, K. Kumar, R. L. Peterson, L. P. Bernal, and K. Najafi, "A scalable, modular, multi-stage, peristaltic, electrostatic gas micro-pump," *IEEE International Conference on Micro Electro Mechanical Systems (MEMS)*, Paris, France, 2012, pp. 1001-1004.

[Bes13] A. Besharatian, K. Kumar, R. L. Peterson, L. P. Bernal, and K. Najafi, "Valve-Only Pumping in Mechanical Gas Micropumps," *IEEE International Conference on Solid-State Sensors, Actuators and Microsystems (Transducers)*, Barcelona, Spain, 2013.

[Bhu07] A. Bhushan, D. Yemane, E. B. Overton, J. Goettert, and M. C. Murphy, "Fabrication and preliminary results for LiGA fabricated nickel micro gas chromatograph columns," *Journal of Microelectromechanical Systems,* vol. 16, no. 2, pp. 383-93, 2007.

[Blu12] L. M. Blumberg, "Chapter 2 - Theory of Gas Chromatography," in *Gas Chromatography*, eds. C. F. Poole, Elsevier, 2012, pp. 19-78.

[Bon08] U. Bonne, "Gas Sensors," in *Comprehensive Microsystems*, eds. Y. B. Gianchandani, O. Tabata, and H. Zappe, Elsevier, 2008, pp. 375-432.

[Bro94] S. K. Brown, M. R. Sim, M. J. Abramson, and C. N. Gray, "Concentrations of Volatile Organic Compounds in Indoor Air – A Review," *Indoor Air,* vol. 4, no. 2, pp. 123-134, 1994.

[Bry14] J. Bryant-Genevier, K. Scholten, S. K. Kim, and E. T. Zellers, "Multivariate curve resolution of co-eluting vapors from a gas chromatograph with microsensor array detector," *Sensors and Actuators B: Chemical,* vol. 202, pp. 167-176, 2014.

[Cab01] C. Cabuz, W. R. Herb, E. I. Cabuz, and S. T. Lu, "The dual diaphragm pump," *IEEE International Conference on Micro Electro Mechanical Systems (MEMS)*, Interlaken, Switzerland, 2001, pp. 519-522.

[Cap13] A. Cappella, J.-L. Battaglia, V. Schick, A. Kusiak, A. Lamperti, C. Wiemer, and B. Hay, "High Temperature Thermal Conductivity of Amorphous Al_2O_3 Thin Films Grown by Low Temperature ALD," *Advanced Engineering Materials,* vol. 15, no. 11, pp. 1046-1050, 2013.

[Col13] W. Collin, G. Serrano, L. K. Wright, H. Chang, N. Nunovero, and E. T. Zellers, "Fieldable MEMS gas chromatograph for rapid determinations of explosive marker compounds in complex mixtures," *IEEE International Conference on Solid-State Sensors, Actuators and Microsystems (Transducers)*, Barcelona, Spain, 2013, pp. 2763-2766.

[Col04] L. A. Colón and L. J. Baird, "Detectors in Modern Gas Chromatography," in *Modern Practice of Gas Chromatography*, eds., John Wiley & Sons, Inc., 2004, pp. 275-337.

[Eun12] C. K. Eun and Y. B. Gianchandani, "Microdischarge-Based Sensors and Actuators for Portable Microsystems: Selected Examples," *IEEE Journal of Quantum Electronics,* vol. 48, no. 6, pp. 814-26, 2012.

[Gar15] A. Garg, M. Akbar, E. Vejerano, S. Narayanan, L. Nazhandali, L. C. Marr, and M. Agah, "Zebra GC: A mini gas chromatography system for trace-level determination of hazardous air pollutants," *Sensors and Actuators B: Chemical,* vol. 212, pp. 145-154, 2015.

[Gor12] R. J. M. Gordenker and K. D. Wise, "A programmable palm-size gas analyzer for use in micro autonomous systems," *Proceedings of SPIE 8373, Micro- and Nanotechnology Sensors, Systems, and Applications IV*, Baltimore, 2012, p. 83731O (6 pp.).

[Gos08] S. Gosav, R. Dinica, and M. Praisler, "Choosing between GC-FTIR and GC-MS spectra for an efficient intelligent identification of illicit amphetamines," *Journal of Molecular Structure,* vol. 887, no. 1-3, pp. 269-278, 2008.

[Gre13] S. R. Green, R. Malhotra, and Y. B. Gianchandani, "Sub-Torr Chip-Scale Sputter-Ion Pump Based on a Penning Cell Array Architecture," *Journal of Microelectromechanical Systems,* vol. 22, no. 2, pp. 309-317, 2013.

[Gru70] E. Grushka, "Chromatographic peak capacity and the factors influencing it," *Analytical Chemistry*, vol 42, no 11, pp. 1142-1147, 1970

[Gup12] N. K. Gupta, S. An, and Y. B. Gianchandani, "A Si-micromachined 48-stage Knudsen pump for on-chip vacuum," *Journal of Micromechanics and Microengineering,* vol. 22, paper 105026, no. 10, pp. 1-8, 2012.

[Gup11] N. K. Gupta and Y. B. Gianchandani, "Porous Ceramics for Multistage Knudsen Micropumps-modeling Approach and Experimental Evaluation," *Journal of Micromechanics and Microengineering,* vol. 21, paper 095029, no. 9, pp. 1-14, 2011.

[Gup11] N. K. Gupta and Y. B. Gianchandani, "Thermal transpiration in mixed cellulose ester membranes: Enabling miniature, motionless gas pumps," *Microporous and Mesoporous Materials,* vol. 142, no. 2-3, pp. 535-541, 2011.

[Hag01] C. Hagleitner, A. Hierlemann, D. Lange, A. Kummer, N. Kerness, O. Brand, and H. Baltes, "Smart single-chip gas sensor microsystem," *Nature,* vol. 414, no. 6861, pp. 293-6, 2001.

[Hau07] J. P. Hauschild, E. Wapelhorst, and J. Müller, "Mass spectra measured by a fully integrated MEMS mass spectrometer," *International Journal of Mass Spectrometry,* vol. 264, no. 1, pp. 53-60, 2007.

[Hen98] A. K. Henning, J. S. Fitch, J. M. Harris, E. B. Dehan, B. A. Cozad, L. Christel, Y. Fathi, D. A. Hopkins Jr, L. I. Lilly, W. McCulley, W. A. Weber, and M. Zdeblick, "Microfluidic MEMS for semiconductor processing," *IEEE transactions on components, packaging, and manufacturing technology. Part B,* vol. 21, no. 4, pp. 329-337, 1998.

[Hos11] A. R. Hoskinson, J. Hopwood, N. W. Bostrom, J. A. Crank, and C. Harrison, "Low-power microwave-generated helium microplasma for molecular and atomic spectrometry," *Journal of Analytical Atomic Spectrometry,* vol. 26, pp. 1258-1264, 2011.

[Huf07] J. Huff, "Benzene-induced Cancers: Abridged History and Occupational Health Impact," *International Journal of Occupational and Environmental Health,* vol. 13, no. 2, pp. 213-221, 2007.

[Igr06] R. Igreja and C. J. Dias, "Dielectric response of interdigital chemocapacitors: The role of the sensitive layer thickness," *Sensors and Actuators B (Chemical),* vol. 115, no. 1, pp. 69-78, 2006.

[Jon73] L. A. Jonas and J. A. Rehrmann, "Predictive equations in gas adsorption kinetics," *Carbon,* vol. 11, no. 1, pp. 59-64, 1973.

[Kaa10] B. C. Kaanta, H. Chen, and X. Zhang, "A monolithically fabricated gas chromatography separation column with an integrated high sensitivity thermal conductivity detector," *Journal of Micromechanics and Microengineering,* vol. 20, no. 5, p. 055016 (6 pp.), 2010.

[Kam98] K. P. Kamper, J. Dopper, W. Ehrfeld, and S. Oberbeck, "A self-filling low-cost membrane micropump," *The Eleventh Annual International Workshop on Micro Electro Mechanical Systems (MEMS)*, 1998, pp. 432-437.

[Kim07] H. Kim, A. A. Astle, K. Najafi, L. P. Bernal, and P. D. Washabaugh, "A fully integrated high-efficiency peristaltic 18-stage gas micropump with active microvalves," *IEEE International Conference on Micro Electro Mechanical Systems (MEMS)*, Kobe, Japan, 2007, pp. 131-134.

[Kim10] H. Kim, K. Najafi, and L.P. Bernal, "Helmholtz Resonance Based Micro Electrostatic Actuators for Compressible Gas Control: a Microjet Generator and a Gas Micro Pump," *Journal of Microelectronics and Electronic Packaging,* vol. 7, no. 1, pp. 1-9, 2010.

[Kim15] H. Kim, A. A. Astle, K. Najafi, L. P. Bernal, and P. D. Washabaugh, "An Integrated Electrostatic Peristaltic 18-Stage Gas Micropump With Active Microvalves," *Journal of Microelectromechanical Systems,* vol. 24, no. 1, pp. 192-206, 2015.

[Kim07] H. Kim, W. H. Steinecker, S. Reidy, G. R. Lambertus, A. A. Astle, K. Najafi, E. T. Zellers, L. P. Bernal, P. D. Washabaugh, and K. D. Wise, "A Micropump-Driven High-Speed MEMS Gas Chromatography System," *IEEE International Conference on Solid-State Sensors, Actuators and Microsystems Conference (Transducers)*, Lyon, France, 2007, pp. 1505-1508.

[Kim11] S. K. Kim, H. Chang, and E. T. Zellers, "Microfabricated gas chromatograph for the selective determination of trichloroethylene vapor at sub-parts-per-billion concentrations in complex mixtures," *Analytical Chemistry,* vol. 83, no. 18, pp. 7198-7206, 2011.

[Knu09] M. Knudsen, "Eine Revision der Gleichgewichtsbedingung der Gase. Thermische Molekularstromung," *Annalen der Physik, Leipzig,* vol. 336, no. 1, pp. 205-229, 1909.

[Knu50] M. Knudsen and J. R. Partington, *The Kinetic Theory of Gases. Some Modern Aspects* vol. 39. American Chemical Society, 1950.

[Kos95] R. Kostiainen, "Volatile organic compounds in the indoor air of normal and sick houses," *Atmospheric Environment,* vol. 29, no. 6, pp. 693-702, 1995.

[Kul14] G. S. Kulkarni, K. Reddy, Z. Zhong, and X. Fan, "Graphene nanoelectronic heterodyne sensor for rapid and sensitive vapour detection," *Nature Communications,* vol. 5, 2014.

[Lam05] G. Lambertus and R. Sacks, "Stop-flow programmable selectivity with a dual-column ensemble of microfabricated etched silicon columns and air as carrier gas," *Analytical Chemistry,* vol. 77, no. 7, pp. 2078-2084, 2005.

[Las04] D. J. Laser and J. G. Santiago, "A review of micropumps," *Journal of Micromechanics and Microengineering,* vol. 14, no. 6, pp. 35-64, 2004.

[Lew06] P. R. Lewis, R. P. Manginell, D. R. Adkins, R. J. Kottenstette, D. R. Wheeler, S. S. Sokolowski, D. E. Trudell, J. E. Byrnes, M. Okandan, J. M. Bauer, R. G. Manley, and G. C. Frye-Mason, "Recent advancements in the gas-phase MicroChemLab," *IEEE Sensors Journal,* vol. 6, no. 3, pp. 784-795, 2006.

[Lew07] P. R. Lewis and D. R. Wheeler, "Non-planar microfabricated gas chromatography column," US Patent 7273517 B1, 2007.

[Liu11] J. Liu, N. K. Gupta, K. D. Wise, Y. B. Gianchandani, and X. Fan, "Demonstration of motionless Knudsen pump based micro-gas chromatography featuring micro-fabricated columns and on-column detectors," *Lab on a Chip,* vol. 11, no. 20, pp. 3487-3492, 2011.

[Liu10] J. Liu, Y. Sun, D. J. Howard, G. Frye-Mason, A. K. Thompson, S.-j. Ja, S.-K. Wang, M. Bai, H. Taub, M. Almasri, and X. Fan, "Fabry−Pérot Cavity Sensors for Multipoint On-Column Micro Gas Chromatography Detection," *Analytical Chemistry,* vol. 82, no. 11, pp. 4370-4375, 2010.

[Liu09] K. Liu, W. Zhang, W. Chen, K. Li, F. Dai, F. Cui, X. Wu, G. Ma, and Q. Xiao, "The development of micro-gyroscope technology," *Journal of Micromechanics and Microengineering,* vol. 19, no. 11, p. 113001, 2009.

[Lod03] P. Lodewyckx, G. O. Wood, and S. K. Ryu, "The Wheeler-Jonas equation: A versatile tool for the prediction of carbon bed breakthrough times," *Carbon 2003 Conference*, Oviedo, Spain, 2003, pp. 1345-1349.

[Lu05] C.-J. Lu, W. H. Steinecker, W.-C. Tian, M. C. Oborny, J. M. Nichols, M. Agah, J. A. Potkay, H. K. L. Chan, J. Driscoll, R. D. Sacks, K. D. Wise, S. W. Pang, and E. T. Zellers, "First-generation hybrid MEMS gas chromatograph," *Lab on a Chip,* vol. 5, no. 10, pp. 1123-31, 2005.

[Luo11] X. Luo, W. Zhu, B. Mitra, J. Liu, T. Liu, X. Fan, Y. Gianchandani, “A Chemical Detector for Gas Chromatography Using Pulsed Discharge Emission Spectroscopy on a Microchip,” *American Geophysical Union, Fall Meeting*, San Francisco, CA, Dec. 2011

[Man08] R. P. Manginell, D. R. Adkins, M. W. Moorman, R. Hadizadeh, D. Copic, D. A. Porter, J. M. Anderson, V. M. Hietala, J. R. Bryan, D. R. Wheeler, K. B. Pfeifer, and A. Rumpf, "Mass-sensitive microfabricated chemical preconcentrator," *Journal of Microelectromechanical Systems,* vol. 17, no. 6, pp. 1396-1407, 2008.

[Man11] R. P. Manginell, J. M. Bauer, M. W. Moorman, L. J. Sanchez, J. M. Anderson, J. J. Whiting, D. A. Porter, D. Copic, and K. E. Achyuthan, "A monolithically-integrated μGC chemical sensor system," *Sensors,* vol. 11, no. 7, pp. 6517-6532, 2011.

[Mar99] J. E. Mark, *Polymer Data Handbook*. Oxford University Press, 1999.

[Mar97] P. A. Martos, A. Saraullo, and J. Pawliszyn, "Estimation of Air/Coating Distribution Coefficients for Solid Phase Microextraction Using Retention Indexes from Linear Temperature-Programmed Capillary Gas Chromatography. Application to the Sampling and Analysis of Total Petroleum Hydrocarbons in Air," *Analytical Chemistry,* vol. 69, no. 3, pp. 402-408, 1997.

[McN05] S. McNamara and Y. B. Gianchandani, "On-Chip Vacuum Generated by a Micromachined Knudsen Pump," *Journal of Microelectromechanical Systems,* vol. 14, no. 4, pp. 741-746, 2005.

[Mit08] B. Mitra and Y. B. Gianchandani, "The Detection of Chemical Vapors in Air Using Optical Emission Spectroscopy of Pulsed Microdischarges From Two- and Three- Electrode Microstructures," *IEEE Sensors Journal,* vol. 8, no. 8, pp. 1445-1454, 2008.

[Mit08] B. Mitra, B. Levey, and Y. B. Gianchandani, "Hybrid arc/glow microdischarges at atmospheric pressure and their use in portable systems for liquid and gas sensing," *IEEE Transactions on Plasma Science,* vol. 36, no. 4, Part 5, pp. 1913-1924, 2008.

[Mls06] T. E. Mlsna, S. Cemalovic, M. Warburton, S. T. Hobson, D. A. Mlsna, and S. V. Patel, "Chemicapacitive microsensors for chemical warfare agent and toxic industrial chemical detection," *Sensors and Actuators B (Chemical),* vol. 116, no. 1-2, pp. 192-201, 2006.

[Mor14] K. Morimoto, Y. Qin, and Y. B. Gianchandani, "Modeling and characterization of the transient performance of a gas detector based on fringe-field capacitance," *IEEE SENSORS*, Valencia, Spain, 2014, pp. 1843-1846.

[Nac12] K. Nachef, F. Marty, E. Donzier, B. Bourlon, K. Danaie, and T. Bourouina, "Micro gas chromatography sample injector for the analysis of natural gas," *Journal of Microelectromechanical Systems,* vol. 21, no. 3, pp. 730-8, 2012.

[Nam88] J. Namieśnik, "Preconcentration of gaseous organic pollutants in the atmosphere," *Talanta,* vol. 35, no. 7, pp. 567-587, 1988.

[Nar12] S. Narayanan, B. Alfeeli, and M. Agah, "Two-port static coated micro gas chromatography column with an embedded thermal conductivity detector," *IEEE Sensors Journal,* vol. 12, no. 6, pp. 1893-1900, 2012.

[Noh02] H. Noh, P. J. Hesketh, and G. C. Frye-Mason, "Parylene gas chromatographic column for rapid thermal cycling," *Journal of Microelectromechanical Systems,* vol. 11, no. 6, pp. 718-25, 2002.

[O'Ne68] R. R. O'Neil and G. Davidson, "The fluorescence of air and nitrogen excited by energetic electrons [Final Report, 12 Mar. 1964-11 Feb. 1967]," American Science and Engineering Inc., Cambridge, MA, ASE-1602, Jan. 1968.

[Occ15] Occ, "Toxic and Hazardous Substances," Occupational Safety and Health Standards, 1910.1000, Available at https://www.osha.gov, Access date 4/29/2015

[Oh06] K. W. Oh and C. H. Ahn, "A review of microvalves," *Journal of Micromechanics and Microengineering,* vol. 16, no. 5, pp. 13-39, 2006.

[Par09] J. M. Park, A. T. Evans, K. Rasmussen, T. R. Brosten, G. F. Nellis, S. A. Klein, and Y. B. Gianchandani, "A microvalve with integrated sensors and customizable normal state for low-temperature operation," *Journal of Microelectromechanical Systems,* vol. 18, no. 4, pp. 868-877, 2009.

[Pat03] S. V. Patel, T. E. Mlsna, B. Fruhberger, E. Klaassen, S. Cemalovic, and D. R. Baselt, "Chemicapacitive microsensors for volatile organic compound detection," *Sensors and Actuators B: Chemical,* vol. 96, no. 3, pp. 541-553, 2003.

[Pea50] R. W. Pearse and A. G. Gaydon, *The identification of molecular spectra*. Chapman and Hall, 1950.

[Pha10] K. Pharas and S. McNamara, "Knudsen pump driven by a thermoelectric material," *Journal of Micromechanics and Microengineering,* vol. 20, paper 125032, no. 12, pp. 1-7, 2010.

[Pot07] J. A. Potkay, G. R. Lambertus, R. D. Sacks, and K. D. Wise, "A low-power pressure- and temperature-programmable micro gas chromatography column," *Journal of Microelectromechanical Systems,* vol. 16, no. 5, pp. 1071-9, 2007.

[Pot12] J. A. Potkay and K. D. Wise, "A Hybrid Thermopneumatic and Electrostatic Microvalve with Integrated Position Sensing," *Micromachines,* vol. 3, no. 2, pp. 379-395, 2012.

[Qin13] Y. Qin and Y. B. Gianchandani, "A facile, standardized fabrication approach and scalable architecture for a micro gas chromatography system with integrated pump," *IEEE International Conference on Solid-State Sensors, Actuators and Microsystems (Transducers)*, Barcelona, Spain, 2013, pp. 2755-2758.

[Qin14] Y. Qin and Y. B. Gianchandani, "*iGC1*: An Integrated Fluidic System for Gas Chromatography Including Knudsen Pump, Preconcentrator, Column, and Detector Microfabricated by a Three-Mask Process," *Journal of Microelectromechanical Systems,* vol. 23, no. 4, pp. 980-990, 2014.

[Qin14] Y. Qin and Y. B. Gianchandani, "*iGC2*: an architecture for micro gas chromatographs utilizing integrated bi-directional pumps and multi-stage preconcentrators," *Journal of Micromechanics and Microengineering,* vol. 24, no. 6, p. 065011 (10 pp.), 2014.

[Que05] L. Que, C. G. Wilson, and Y. B. Gianchandani, "Microfluidic electrodischarge devices with integrated dispersion optics for spectral analysis of water impurities," *Journal of Microelectromechanical Systems,* vol. 14, no. 2, pp. 185-191, 2005.

[Rad10] A. D. Radadia, A. Salehi-Khojin, R. I. Masel, and M. A. Shannon, "The effect of microcolumn geometry on the performance of micro-gas chromatography columns for chip scale gas analyzers," *Sensors and Actuators, B: Chemical,* vol. 150, no. 1, pp. 456-464, 2010.

[Red11] K. Reddy, Y. Guo, J. Liu, W. Lee, M.K.K Oo, X. Fan, "On-chip Fabry-Perot interferometric sensors for micro-gas chromatography detection," *Sensors and Actuators: B Chemical,* vol. 159, no. 1, pp. 60-5, 2011.

[Rei06] S. Reidy, G. Lambertus, J. Reece, and R. Sacks, "High-performance, static-coated silicon microfabricated columns for gas chromatography," *Analytical Chemistry,* vol. 78, no. 8, pp. 2623-2630, 2006.

[Rey79] O. Reynolds, "On Certain Dimensional Properties of Matter in the Gaseous State," *Philosophical Transactions of the Royal Society of London,* vol. 170, pp. 727-845, 1879.

[RGB15] RGB Lasersysteme GmbH, 2015, "Qstick - The World's first USB stick Spectrometer", Available at http://www.rgb-laser.com/content_products/product_qstick.html, Access date 4/29/2015

[Rob98] J. K. Robertson and K. D. Wise, "A low pressure micromachined flow modulator," *Sensors and Actuators A (Physical),* vol. A71, no. 1-2, pp. 98-106, 1998.

[Roj13] M. Rojas-Cárdenas, I. Graur, P. Perrier, and J. G. Méolans, "Time-dependent experimental analysis of a thermal transpiration rarefied gas flow," *Physics of Fluids,* vol. 25, no. 7, p. 072001 (24 pp.), 2013.

[San15] A. Sandoughsaz, A. Besharatian, L. P. Bernal, and K. Najafi, "Modular Stacked Variable-Compression Ratio Multi-Stage Gas Micropump," *IEEE International Conference on Solid-State Sensors, Actuators and Microsystems (Transducers)*, Anchorage, Alaska, 2015.

[Sci15] Scientific Equipment Source, 2015, "Agilent 6890 Gas Chromatograph", Available at http://www.se-source.com/agilent6890.htm, Access date 4/29/2015

[Seo12] J. H. Seo, S. K. Kim, E. T. Zellers, and K. Kurabayashi, "Microfabricated passive vapor preconcentrator/injector designed for microscale gas chromatography," *Lab on a Chip,* vol. 12, no. 4, pp. 717-724, 2012.

[Ser12] G. Serrano, D. Paul, S.-J. Kim, K. Kurabayashi, and E. T. Zellers, "Comprehensive two-dimensional gas chromatographic separations with a microfabricated thermal modulator," *Analytical Chemistry,* vol. 84, no. 16, pp. 6973-6980, 2012.

[Ser13] G. Serrano, T. Sukaew, and E. T. Zellers, "Hybrid preconcentrator/focuser module for determinations of explosive marker compounds with a micro-scale gas chromatograph," *Journal of Chromatography A,* vol. 1279, pp. 76-85, 2013.

[Sha96] F. Sharipov, "Rarefied gas flow through a long tube at any temperature ratio," *Journal of Vacuum Science & Technology A (Vacuum, Surfaces, and Films),* vol. 14, no. 4, pp. 2627-2635, 1996.

[Sha99] F. Sharipov, "Non-isothermal gas flow through rectangular microchannels," *Journal of Micromechanics and Microengineering,* vol. 9, no. 4, pp. 394-401, 1999.

[Sno04] N. H. Snow, "Inlet Systems for Gas Chromatography," in *Modern Practice of Gas Chromatography*, eds. R. L. Grob and E. F. Barry, John Wiley & Sons, Inc., 2004, pp. 461-489.

[Son13] J. Son, H. Kim, and H. Kim, "Pneumatic-less high-speed vacuum meso-pump driven by programmable hydraulics," *IEEE International Conference on Micro Electro Mechanical Systems (MEMS)*, Taipei, Taiwan, 2013, pp. 584-587.

[Ste11] W. H. Steinecker, S. K. Kim, F. I. Bohrer, L. Farina, C. Kurdak, and E. T. Zellers, "Electron-Beam Patterned Monolayer-Protected Gold Nanoparticle Interface Layers on a Chemiresistor Vapor Sensor Array," *IEEE Sensors Journal,* vol. 11, no. 2, pp. 469-80, 2011.

[Ste93] E. Stemme and G. Stemme, "A valveless diffuser/nozzle-based fluid pump," *Sensors and Actuators A (Physical),* vol. A39, no. 2, pp. 159-67, 1993.

[Stu00] B. Stuart, "Infrared Spectroscopy," in *Kirk-Othmer Encyclopedia of Chemical Technology*, eds. A. Seidel and M. Bickford, John Wiley & Sons, Inc., 2000.

[Stu04] B. Stuart, *Infrared Spectroscopy : Fundamentals and Applications*. Wiley, 2004.

[Tan08] K. Tanaka, T. Van Dau, R. Sakamoto, T. X. Dinh, D. V. Dao, and S. Sugiyama, "Fabrication and basic characterization of a piezoelectric valveless micro jet pump," *Japanese Journal of Applied Physics,* vol. 47, no. 11, pp. 8615-8618, 2008.

[Ter79] S. C. Terry, J. H. Jerman, and J. B. Angell, "A gas chromatographic air analyzer fabricated on a silicon wafer," *IEEE Transactions on Electron Devices,* vol. 26, no. 12, pp. 1880-1886, 1979.

[Tia05] W.-C. Tian, H. K. L. Chan, C.-J. Lu, S. W. Pang, and E. T. Zellers, "Multiple-stage microfabricated preconcentrator-focuser for micro gas chromatography system," *Journal of Microelectromechanical Systems,* vol. 14, no. 3, pp. 498-507, 2005.

[Tia03] W.-C. Tian, S. W. Pang, C.-J. Lu, and E. T. Zellers, "Microfabricated preconcentrator-focuser for a microscale gas chromatograph," *Journal of Microelectromechanical Systems,* vol. 12, no. 3, pp. 264-272, 2003.

[Tze15] T.-H. Tzeng, C.-Y. Kuo, S.-Y. Wang, P.-K. Huang, P.-H. Kuo, Y.-M. Huang, W.-C. Hsieh, S.-A. Yu, Y. J. Tseng, W.-C. Tian, S.-C. Lee, and S.-S. Lu, "A portable micro gas chromatography system for volatile compounds detection with 15 ppb of sensitivity," *IEEE International Solid-State Circuits Conference (ISSCC)*, 2015, pp. 1-3.

[van08] H. van Weerden, G.-J. Burger, and J. Elders, "Fast micro-GC capabilities based on a microintegration technology platform," *American Laboratory,* vol. 40, no. 16, pp. 14-15, 2008.

[Voi08] I. Voiculescu, M. Zaghloul, and N. Narasimhan, "Microfabricated chemical preconcentrators for gas-phase microanalytical detection systems," *Trends in Analytical Chemistry,* vol. 27, no. 4, pp. 327-343, 2008.

[Wes08] A. Westman-Brinkmalm and G. Brinkmalm, "A Mass Spectrometer's Building Blocks," in *Mass Spectrometry: Instrumentation, Interpretation, and Applications*, eds. R. Ekman, J. Silberring, and A. M. Westman-Brinkmalm, John Wiley & Sons, Inc., 2008, pp. 15-87.

[Wil03] C. G. Wilson, Y. B. Gianchandani, R. R. Arslanbekov, V. Kolobov, and A. E. Wendt, "Profiling and modeling of dc nitrogen microplasmas," *Journal of Applied Physics,* vol. 94, no. 5, pp. 2845-2851, 2003.

[Woh08] C. Wohlfarth, *Static Dielectric Constants of Pure Liquids and Binary Liquid Mixtures: Supplement to IV/6*. Springer, 2008.

[Yee13] S. Y. Yee, R. L. Peterson, L. P. Bernal, and K. Najafi, "Highly-reliable electrostatic actuator using filleted electrode made with photoresist solvent reflow," *International Conference on Solid-State Sensors, Actuators and Microsystems (Transducers)*, Barcelona, Spain, 2013, pp. 1617-1620.

[You03] M. Young, Y. L. Han, E. P. Muntz, G. Shiflett, A. Ketsdever, and A. Green, "Thermal transpiration in microsphere membranes," *Rarefield Gas Dynamics: 23rd International Symposium*, Whistler, British Columia (Canada), 2003, pp. 743-51.

[Zam09] S. Zampolli, I. Elmi, F. Mancarella, P. Betti, E. Dalcanale, G. C. Cardinali, and M. Severi, "Real-time monitoring of sub-ppb concentrations of aromatic volatiles with a MEMS-enabled miniaturized gas-chromatograph," *Sensors and Actuators: B Chemical,* vol. 141, no. 1, pp. 322-8, 2009.

[Zar10] M. A. Zareian-Jahromi and M. Agah, "Microfabricated gas chromatography columns with monolayer-protected gold stationary phases," *Journal of Microelectromechanical Systems,* vol. 19, no. 2, pp. 294-304, 2010.

[Zar89] M. C. Zaretsky, J. R. Melcher, and C. M. Cooke, "Moisture sensing in transformer oil using thin-film microdielectrometry," *IEEE Transactions on Electrical Insulation,* vol. 24, no. 6, pp. 1167-76, 1989.

[Zel11] E. T. Zellers, G. Serrano, H. Chang, and L. K. Amos, "A micro gas chromatograph for high-speed determinations of explosive markers," *IEEE International Conference on Solid-State Sensors, Actuators and Microsystems (Transducers)*, Beijing, China, 2011, pp. 2082-2085.

[Zha93] Z. L. Zhang and N. C. MacDonald, "Fabrication of submicron high-aspect-ratio GaAs actuators," *Journal of Microelectromechanical Systems,* vol. 2, no. 2, pp. 66-73, 1993.